Purdue University
Purdue e-Pubs

Department of Electrical and Computer Engineering Technical Reports

Department of Electrical and Computer Engineering

1-1-1988

Design and Fabrication of a Self-Calibrating Germanium Photodiode for Radiometric Applications

Daniel Li-Chung Huang
Purdue University

Richard J. Schwartz
Purdue University

Follow this and additional works at: https://docs.lib.purdue.edu/ecetr

Huang, Daniel Li-Chung and Schwartz, Richard J., "Design and Fabrication of a Self-Calibrating Germanium Photodiode for Radiometric Applications" (1988). *Department of Electrical and Computer Engineering Technical Reports.* Paper 590.
https://docs.lib.purdue.edu/ecetr/590

This document has been made available through Purdue e-Pubs, a service of the Purdue University Libraries. Please contact epubs@purdue.edu for additional information.

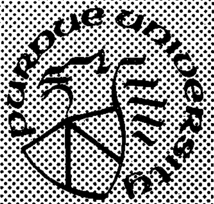

Design and Fabrication of a Self-Calibrating Germanium Photodiode for Radiometric Applications

Daniel Li-Chung Huang
Richard J. Schwartz

TR-EE 88-4
January 1988

School of Electrical Engineering
Purdue University
West Lafayette, Indiana 47907

DESIGN AND FABRICATION OF A SELF-CALIBRATING GERMANIUM PHOTODIODE FOR RADIOMETRIC APPLICATION

Final Report for National Bureau of Standards
Grant NB 82 NAHA 3032

submitted
by

Daniel Li-Chung Huang
Richard J. Schwartz

School of Electrical Engineering
Purdue University
West Lafayette, IN 47907

TR-EE 88-4

January 1988

TABLE OF CONTENTS

Page

LIST OF TABLES vi

LIST OF FIGURES vii

ABSTRACT xiii

CHAPTER I - INTRODUCTION 1

1.1 Radiometry 1
1.2 Self-calibrating Absolute Radiometer 2
1.3 Long-wavelength Optical Communications 4
1.4 Overview 6

CHAPTER II - REVIEW 8

2.1 Introduction 8
2.2 Materials 9
2.3 Photoconductors 9
2.3.1 Extrinsic Photoconductors 9
2.3.2 Intrinsic Photoconductors 11
2.4 p-i-n Photodiodes 12
2.5 Avalanche Photodiodes (APD) 13
2.5.1 Compound Material APDs 14
2.5.2 Germanium APD 14
2.6 Induced Junction Photodiodes 15
2.7 Summary 16

CHAPTER III - GERMANIUM 17

3.1 Introduction 17
3.2 General Properties 17
3.3 Band Structure 17
3.4 Mobility and Diffusion Coefficient 19

Page

3.5 Optical Properties 20
3.6 Heavily Doped Germanium 23

CHAPTER IV - THEORY 25

4.1 Introduction....................25
4.2 Quantum Efficiency....................25
4.2.1 Absorption Rate Density, A(λ,x) 26
4.2.2 Quantum Yield, Y(λ,x)....................28
4.2.3 Collection Efficiency, P(x) 29
4.2.4 Internal Quantum Efficiency 31
4.3 Derivation of the Photocurrent for Monochromatic Light....................32
4.4 Surface Effects....................46
4.5 Summary 50

CHAPTER V - DESIGN CONSIDERATIONS....................54

5.1 Introduction....................54
5.2 Leakage Current 54
5.3 Quantum Efficiency....................55
5.3.1 Device Thickness 56
5.3.2 Collection Efficiency 57
5.3.2.1 Front Surface 57
5.3.2.2 Emitter....................57
5.3.2.3 Base....................58
5.3.2.4 Back Surface 59
5.4 Summary 59

CHAPTER VI - FABRICATION OF GERMANIUM PHOTODIODES........61

6.1 Introduction....................61
6.2 Wafers 61
6.3 Photolithography....................61
6.4 Oxidation....................62
6.4.1 Sputtered SiO_2....................63
6.4.2 Chemical Vapor Deposition (CVD)....................64
6.4.3 SiO_2-Ge Interface 65
6.5 Ion Implantation 66
6.5.1 Implantation Impurities 66
6.5.2 Implantation Annealing....................67

Page

6.5.3 Implantation Diagnosis....68
6.5.3.1 Spreading Resistance Technique....68
6.5.3.2 Four Point Probe Technique....69
6.6 Metalization....75
6.6.1 Sputtering System....77
6.6.2 Deposition Procedures....78
6.6.3 Post-metalization Annealing....78
6.7 Photodiode Design....79
6.8 Test Cells....83
6.9 Summary....83

CHAPTER VII - MEASUREMENTS AND RESULTS....86

7.1 Introduction....86
7.2 Electrical Measurements....86
7.2.1 Dark Current Measurements....86
7.2.2 I_{sc}-V_{oc} Measurements....90
7.2.3 Series Resistance R_s Measurements....94
7.2.4 C-V Measurements....96
7.2.5 MOS Transistor Measurements....98
7.3 Optical Measurements....98
7.4 Summary....104

CHAPTER VIII - NUMERICAL ANALYSIS....107

8.1 Introduction....107
8.2 Program Description and Modifications....108
8.2.1 General Description....108
8.2.2 Recombination....109
8.2.3 Generation....110
8.2.4 Bandgap and Intrinsic Carrier Concentration....110
8.2.5 Mobility and Diffusion Coefficient....111
8.2.6 Optical Properties....114
8.2.7 Minority Carrier Lifetime and Surface Recombination Velocity....117
8.2.8 Normalizations and Boundary Conditions....118
8.2.9 Numerical Techniques....122
8.3 Simulations....123
8.4 Summary....145

Page

CHAPTER IX - SUMMARY AND CONCLUSIONS 151

9.1 Summary 151
9.2 Conclusions 152

LIST OF REFERENCES 154

APPENDIX - FABRICATION PROCEDURES 161

VITA 163

LIST OF TABLES

Table Page

4.1 Device parameters 39

8.1 Mobility in germanium....................113

8.2 Coefficient constants in Eq.(8.22) 116

8.3 Normalization factors 119

8.4 Device parameters for simulation 125

LIST OF FIGURES

Figure Page

1.1 Block diagram of a radiometric measurement system. 1

1.2 Optical configuration of a light trapped radiometer. 5

2.1 Absorption coefficient of materials with respect to wavelength. 10

3.1 Energy band diagram of germanium. 18

3.2 Absorption coefficient of single-crystal germanium at 77°K and 300°K. 21

3.3 Absorption coefficient for p-type germanium with 0.07 Ω-cm resistivity. 22

4.1 Cross section of an n^+pp^+ photodiode. 27

4.2 Quantum yield in germanium as a function of photon energy. 30

4.3 Measured (□) and computed (○) internal quantum efficiency of an n^+pp^+ photodiode. The dashed lines are the three components of the internal quantum efficiency expressed by Eq. (4.34). The device parameters are shown in Table 4.1. 40

4.4 Calculated internal quantum efficiency of n^+pp^+ photodiodes with emitter junction depth $x_j = 0.1\ \mu m$ (□), $x_j = 0.2\ \mu m$ (○), and $x_j = 0.3\ \mu m$ (△). The device parameters are shown in Table 4.1. 42

Figure Page

4.5 Computed (□) internal quantum efficiency of an n^+pp^+ photodiode with $x_j = 0.3\ \mu m$. The dashed lines are the three components of internal quantum efficiency expressed by Eq.(4.34). The diode parameters are shown in Table 4.1. 43

4.6 Computed (solid line) internal quantum efficiency of an n^+pp^+ photodiode with $x_j = 0.1\ \mu m$. The dashed lines are the three components of internal quantum efficiency expressed by Eq.(4.34). The diode parameters are shown in Table 4.1. 44

4.7 Computed internal quantum efficiency of an n^+pp^+ photodiode with $S = 10^3$ cm/sec (□), $S = 10^5$ cm/sec (○), and $S = 10^6$ cm/sec (△). The device parameters are shown in Table 4.1. 45

4.8 (a) Charge distribution in an induced junction diode and (b) energy band diagram near the surface. 47

4.9 The normalized potential as a function of position with $U_s = 12$. The dashed line is the Fermi level. 51

4.10 The electric field as a function of position with $U_s = 12$. 52

4.11 The normalized electron carrier concentration as a function of position with $U_s = 12$. 53

6.1 Measured carrier concentration profile of implanted arsenic with dosage/energy of 2×10^{15} cm^{-2}/70KeV and 6×10^{14} cm^{-2}/40KeV on a 0.1 Ω-cm germanium substrate. 70

6.2 Measured carrier concentration profile of implanted arsenic with dosage/energy of 5×10^{15} cm^{-2}/70KeV on a 0.5 Ω-cm germanium substrate. 71

6.3 Measured carrier concentration profile of implanted arsenic with dosage/energy of 5×10^{15} cm^{-2}/70KeV on a 1.0 Ω-cm germanium substrate. 72

Figure Page

6.4 Measured carrier concentration profile of implanted arsenic with dosage/energy of 5×10^{15} cm^{-2}/70KeV on a 2.0 Ω-cm germanium substrate. 73

6.5 Measured carrier concentration profile of implanted arsenic with dosage/energy of 5×10^{15} cm^{-2}/35KeV on a 2.0 Ω-cm germanium substrate. 74

6.6 Sheet resistivity versus anneal temperature for arsenic implants with dosage/energy of $5\times10^{15}cm^{-2}$/70KeV on 2 Ω-cm (□), $5\times10^{15}cm^{-2}$/70KeV on 1 Ω-cm (○), $5\times10^{15}cm^{-2}$/70KeV on 0.5 Ω-cm (△), $2\times10^{15}cm^{-2}$/70KeV and $6\times10^{14}cm^{-2}$ /40KeV on 0.1 Ω-cm (Y), germanium substrate. 76

6.7 (a) Before and (b) after the 400°C post-metalization anneal. 80

6.8 Cross section of an n^+pp^+ diode. 81

6.9 Cross section of an induced junction diode. 82

6.10 Top view of the photodiode. 84

6.11 Top view of the test cells. 85

7.1 Dark I-V characteristic of an n^+pp^+ diode. 88

7.2 Dark I-V characteristic of an induced junction diode. 89

7.3 Saturation currents as a function of substrate resistivity. 91

7.4 $I_{sc}-V_{oc}$ and forward current of an n^+pp^+ diode. 92

7.5 $I_{sc}-V_{oc}$ and forward current of an induced junction diode. 93

7.6 Cross section of a four-terminal resistor for contact resistance measurements. 95

Figure Page

7.7 The measured high frequency MOS CV characteristic (solid line). The device was fabricated on a $N_A = 1\times10^{16}/cm^3$ germanium substrate with an oxide thickness of 2830 Å and an area of 5.625×10^{-3} cm^2. The dashed line is the ideal CV curve and is shifted to the left along the voltage axis by 48.5 volts. 97

7.8 (a) Top view of the test MOS transistors; (b) the I-V characteristics of a MOS transistor....99

7.9 Internal quantum efficiency of an n^+pp^+ photodiode (dashed line) and an induced junction photodiode (solid line)....101

7.10 Internal quantum efficiency of two n^+pp^+ photodiodes with substrate resistivity of 0.1 Ω-cm (dashed line) and 2 Ω-cm (solid line). 103

7.11 Internal quantum efficiency of two induced junction photodiodes with substrate resistivity of 0.5 Ω-cm (dashed line) and 2 Ω-cm (solid line). 105

7.12 Internal quantum efficiency of two n^+pp^+ photodiodes with estimated emitter junction depth of 1.2 μm (solid line) and 1.7 μm (dashed line). 106

8.1 Flowchart of SCAP1D and SCAP2D operation. 124

8.2 Measured (□), SCAP1D simulated (○), and SCAP2D simulated (△) $I_{sc} - V_{oc}$ of an n^+pp^+ photodiode. 127

8.3 Measured (□), SCAP1D simulated (○), and SCAP2D simulated (△) $I_{sc} - V_{oc}$ of an induced junction photodiode. 128

8.4 Measured (□), SCAP1D simulated (○), and SCAP2D simulated (△) internal quantum efficiency of an n^+pp^+ photodiode. 129

8.5 Measured (□), SCAP1D simulated (○), and SCAP2D simulated (△) internal quantum efficiency of an induced junction photodiode....130

8.6 Doping profile of an n^+pp^+ photodiode near the emitter. 132

Figure Page

8.7 Doping-dependent mobility of an n^+pp^+ photodiode for holes and electrons....132

8.8 Generation rate and integrated generation rate in germanium as a function of position (λ=0.9 μm)....133

8.9 Generation rate and integrated generation rate in germanium as a function of position (λ=1.5 μm)....133

8.10 Energy band diagram as a function of position in an n^+pp^+ photodiode....134

8.11 Energy band diagram as a function of position in an induced junction photodiode....134

8.12 Potential and equilibrium potential as a function of position in a n^+pp^+ photodiode....135

8.13 Potential and equilibrium potential as a function of position in an induced junction photodiode....135

8.14 Electric field as a function of position in an n^+pp^+ photodiode....137

8.15 Electric field as a function of position in an induced junction photodiode....137

8.16 Recombination rate and integrated recombination rate as a function of position in an n^+pp^+ photodiode (λ=0.9 μm)....138

8.17 Recombination rate and integrated recombination rate as a function of position in an induced junction photodiode (λ=0.9 μm). 138

8.18 Recombination rate and integrated recombination rate as a function of position in an n^+pp^+ photodiode (λ=1.5 μm)....139

8.19 Recombination rate and integrated recombination rate as a function of position in an induced junction photodiode (λ=1.5 μm)....139

Figure Page

8.20 Carrier concentration as a function of position in an n^+pp^+ photodiode. 141

8.21 Carrier concentration as a function of position in an induced junction photodiode. 141

8.22 Excess carrier concentration as a function of position in an n^+pp^+ photodiode. 142

8.23 Excess carrier concentration as a function of position in an induced junction photodiode. 142

8.24 Internal quantum efficiency of n^+pp^+ photodiodes with the junction depths of 0.1 μm (□), 0.2 μm (○), and 0.3 μm (△). 143

8.25 Internal quantum efficiency of n^+pp^+ photodiodes with the surface recombination velocities of 10^3 cm/sec (□), 10^4 cm/sec (○), 10^5 cm/sec (△), and 8×10^5 cm/sec (*). 144

8.26 Internal quantum efficiency of induced junction photodiodes with fixed positive charge densities of $2\times12^{11}/cm^2$ (□), $10^{12}/cm^2$ (○), $8\times10^{11}/cm^2$ (△), and $6\times10^{11}/cm^2$ (*). The device parameters are shown in Table 8.4. 146

8.27 Internal quantum efficiency of induced junction photodiodes with the $q\Phi_o$ of 10 mA/cm^2 (□), 100 mA/cm^2 (○), 300 mA/cm^2 (△), and 500 mA/cm^2 (*). 147

8.28 Two-dimensional potential distribution under the low intensity illumination in an induced junction photodiode. 148

8.29 Two-dimensional potential distribution under the high intensity illumination in an induced junction photodiode. 149

ABSTRACT

This work is concerned with the design and fabrication of an absolute radiometric detector operated over the 0.7 to 1.5 μm wavelength range. This application requires a semiconductor photodiode with high internal quantum efficiency and long term stability. Of many possible materials, germanium is chosen because high quality material is available, the fabrication processes are relatively straight forward, and a high quantum efficiency is achievable.

The fabrication procedures for a germanium cell were developed. Two types of germanium photodiodes were fabricated and tested. In both photodiodes, a channel stop has been employed to reduce the lateral current due to surface inversion. Ion implantation is used to form the n^+-p junction, the channel stop and the back surface field. To reduce the surface recombination, CVD SiO_2 was deposited for surface passivation. A Ti/Pd/Ag metal layer was then sputtered to make the interconnections. With this process, dark current as low as 0.35 mA/cm^2 has been observed on a 2 Ω-cm substrate.

The n^+pp^+ photodiodes had a considerably low quantum efficiency than the induced junction photodiodes. It is shown by computer simulation that the internal quantum efficiency, η, of an n^+pp^+ diode is strongly affected by the carrier lifetime, τ, in the emitter and the surface

recombination velocity, S, at the SiO_2-Ge surface. The high quantum efficiency in the induced junction diodes can be attributed to the absence of implantation induced damage in the emitter, and an electric field near the surface, induced by the fixed charges of the SiO_2 layer. With the induced junction structure, we have observed an internal quantum efficiency of 98.8% at 0.7 μm and of 97% at 1.5 μm.

CHAPTER I
INTRODUCTION

1.1. Radiometry

Radiometry is the science and technology of the measurement of electromagnetic radiant energy. A complete radiometric measurement system consists of a number of components including a source of radiant energy, an optical system, a detector which converts the EM energy to electrical energy, and a signal processing device, as shown in Fig. 1.1.

Figure 1.1 A block diagram of a radiometric measurement system.

Typical sources of radiant energy include the sun, lasers, electrical discharge sources, fluorescent materials, etc.. Optical systems used in radiometric measurement consist of lenses, mirrors, apertures, prisms, gratings, filters, polarizers, fiber optics, or other devices. Detectors play a

fundamental role in the history of radiometry. Much of the progress in radiometry is associated with progress in the development of detectors. The most important physical detectors are photomultipliers, photographic detectors, pyroelectric detectors, thermocouples, and of course, semiconductors detectors. Signal processing is also an essential part of a radiometric measurement. Signal processing can involve sophisticated digital and analog circuitry, such as the receivers in optical communication systems, or it can be as simple as a direct measurement of the electrical output signals, such as the quantum efficiency measurement.

1.2. Self-calibrating Absolute Radiometer

In an absolute radiometric measurement, one has to have either a standard (calibrated) source, or a standard (calibrated) photodetector. In the past, the light source was calibrated based on the luminance of a blackbody radiator. The accuracy of this method could be within 1% but the process is very tedious. Another approach to the absolute radiometric measurements is to use a calibrated photodetector. The development of an electrically calibrated pyroelectric radiometer (ECPR) makes this approach much more practical than before [1]. Since electrical power measurements can be made very accurately, the inherent accuracy of the radiometer is increased.

Semiconductor photodetectors have been widely used in radiometric measurement systems. It was suggested that a self-calibration based on the unity internal quantum efficiency of a photovoltaic cell provides a accurate and inexpensive technique for radiometric measurements [2]. The self-

calibration technique was first demonstrated in silicon photodiodes operating over the 0.4 to 1.1 μm wavelength range [3]. It is of considerable practical interest to extend this technique for the use over a wider wavelength range.

At present, the spectral responsivity, R, is often used as a calibration curve for photodiodes. The spectral responsivity is defined as

$$R = \frac{J_L}{W} \tag{1.1}$$

where J_L is the photon-generated current density and W is the power of the incident photon flux. J_L can be written as

$$J_L = \eta\,(1 - r)\,q\,\Phi_0 \tag{1.2}$$

and W as

$$W = \Phi_0\,h\,\nu \tag{1.3}$$

where η is the internal quantum efficiency, r the reflectance of the photodetector surface, q the unit charge, Φ_o the incident flux per unit area per unit time, h Planck's constant, and ν the frequency of the incident radiation. The internal quantum efficiency is defined as the ratio of the number of light-generated carriers to the photon flux Φ_o. Eq.(1.1) can be rewritten as

$$R = \eta\,(1 - r)\,\frac{q}{h\nu} = \eta\,(1 - r)\frac{\lambda}{1.2398} \quad \text{(Amp/watt)} \tag{1.4}$$

where we use the relation $\nu = \frac{c}{\lambda}$, where c is the speed of the light and λ the wavelength of the incident radiation in microns.

The spectral responsivity, R, of a photodiode will be proportional to the wavelength, λ. If the r=0 and η=1, the proportionality constant will

depend solely on the universal constants h, c, and q. A photodiode with $r=0$ and $\eta=1$ is referred to as a self-calibrated photodiode and can be used in a self-calibrating radiometric measurement.

However, a typical photodiode may lose approximately 25 to 35% of the incident power due to surface reflection. The design shown in Fig.(1.2) solves this problem [4]. This design incorporates four identical photodiodes mounted in a protective aluminum housing. The photodiodes are arranged in such a way that the fourth cell redirects the incident beam back along its original path, providing a total of seven successive absorptions of incident power. After seven reflections, a single cell reflectance of 35% reduces the effective reflectance to $(0.35)^7$, or only 0.06%.

With this technique, the effective reflectance can be reduced approximately to zero. Therefore, a self-calibrating radiometer can be achieved by fabricating a photodiode with a minimum recombination loss. The purpose of this thesis is to examine the design, fabrication and testing of a germanium photodiode which approachs the ideal internal quantum efficiency of 1.

1.3. Long-wavelength Optical Communications

The importance of the 0.7 to 1.5 μm wavelength range comes from recent developments in optical fiber communication systems. During recent years, optical fiber communication has been the subject of intensive research and development. Silica-based glass fibers show a low optical attenuation in the spectral region between 1.0 and 1.5 μm [5]. Total losses of less than 0.5 dB/km are reported. In addition, the dispersion falls to zero at a

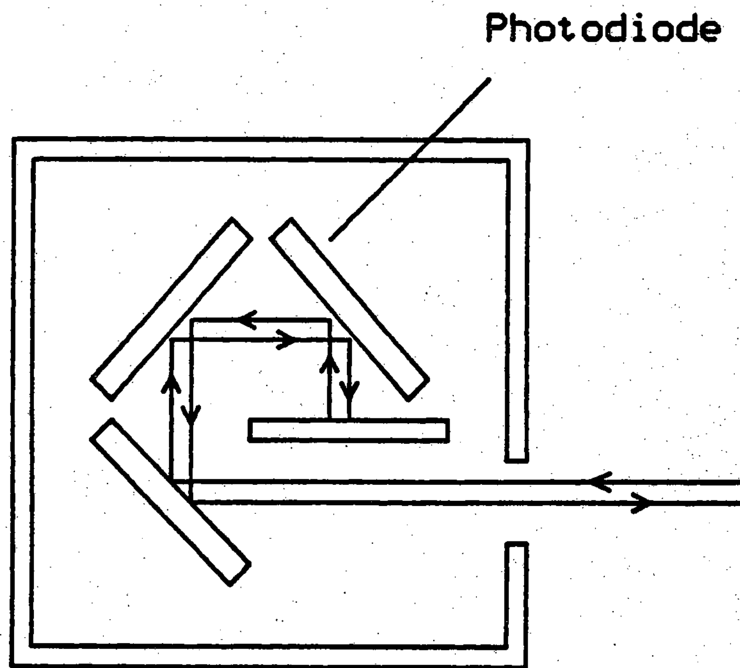

Figure 1.2   Optical configuration of a light trapped radiometer.

wavelength between 1.2 to 1.3 μm [6]. The combination of low fiber loss and negligible dispersion offer the possibility of wide-bandwidth systems operating over long distances. The silicon photodiode, with an absorption coefficient which decreases rapidly beyond 1.1 μm, is not suitable as a detector for this application. Alternative materials are needed for long wavelength photodetection.

The design of a practical radiometer over the 0.7 to 1.5 μm wavelength range becomes essential in order to monitor the full range of optical power in optical communication systems. Semiconductor photodiodes are often chosen for radiometric applications since they typically have high optical-to-electrical efficiency. In addition, they are linear over many orders of magnitude of light intensity, and stable with time and temperature. Silicon, germanium, indium gallium arsenide, and indium gallium arsenide phosphide, among others, are semiconductor photodetectors which have useful sensitivity over some or all of the 0.7 to 1.5 μm wavelength range. Si, with an energy bandgap of 1.12 ev, is useful only for wavelengths shorter than 1.1 μm and thus couldn't be used as a full range radiometer. On the other hand, Ge has a suitable energy bandgap for detecting optical signals in the above wavelength range, including 0.8, 1.33, and 1.5 μm which are the common wavelengths used in the optical fiber communication systems.

1.4. Overview

This research is concerned with the design and fabrication of a self-calibrating Ge photodiode over the 0.7 to 1.5 μm wavelength range. In the following chapter, a brief review of previous work in this area will be

presented. Some of the advantages motivating this research will then be discussed. An analytical equation for internal quantum efficiency will be derived, followed by a description of design considerations for optimal photodiodes. The cell was designed and the fabrication was carried out using our pattern generation tools and fabrication facilities at Purdue University. Measurement techniques will also be discussed, followed by the computer analysis of the measurement results. Finally, some conclusions and comments will be presented.

CHAPTER II
REVIEW

2.1. Introduction

In recent years, the rapid growth of the fiber optics communications industry has increased the demand for precise optical measurements, and attempts have been made to develop more stable and sensitive photodetectors. The most widely used detector of optical radiation is the semiconductor photodiode. The physics of this device is well understood, and its technology is well developed. Basically, the photodiode is a p-n junction diode operated under a zero or reverse biased voltage. When an optical signal impinges on the photodiode, electron-hole pairs are generated and transported to the junction. An electrical signal can then be detected at the terminals of the devices.

Although there are many types of semiconductor photodetectors, we will only review photodetectors which are commonly used in the 0.7 to 1.5 μm wavelength range, and comment on their usefulness in a self-calibrating radiometric application.

2.2. Materials

The key factor which determines if the material is useful for detection of the above wavelength range is the energy bandgap. The bandgap of the material should be narrow enough such that the photon energy can excite the electrons from the valence band to the conduction band. A photodetector is sensitive to radiation with a wavelength less than λ_c where

$$\lambda_c\ (\mu\text{m}) = \frac{1.2398}{E_g(\text{eV})} \tag{2.1}$$

E_g in Eq.(2.1) is the energy bandgap of the material. For instance, the energy bandgap should be 0.82 eV or less for the detection of 1.5 μm wavelength radiation. Fig. 2.1 shows the absorption coefficient of the materials which have useful sensitivity over some or all of the 0.7 to 1.5 μm wavelength range [7].

2.3. Photoconductors

In photoconductors, electrical conductivity increases when they are illuminated. In fact, all semiconductors and insulators become more conductive when illuminated with photons which have enough energy to generate free carriers. There are two types of photoconductors: extrinsic and intrinsic photoconductors.

2.3.1. Extrinsic Photoconductors

Extrinsic photoconductors have been used throughout the infrared spectrum [8,9]. For extrinsic photoconductors, energy levels are introduced between the band edges by introducing impurity levels into semiconductor.

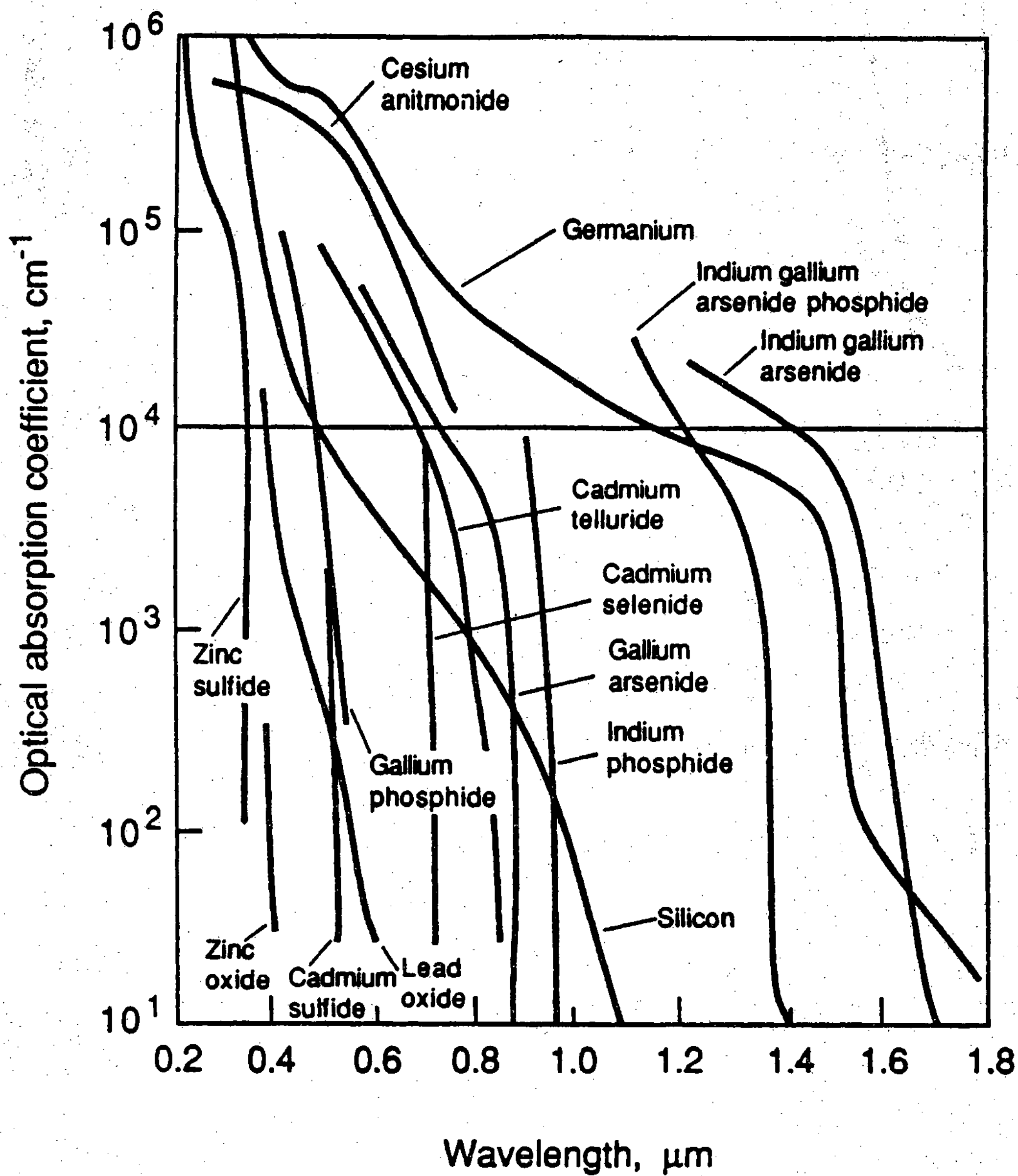

Figure 2.1 Absorption coefficient of materials with respect to wavelength [7].

The incident radiation is absorbed by these levels and free carriers are generated. Extrinsic photodetectors are typically operated at low temperature to reduce generation-recombination noise produced by the impurity states. In addition, they have smaller absorption coefficients than that of intrinsic detectors and thus require a larger physical size for efficient detection. The above factors limit their applications.

2.3.2. Intrinsic Photoconductors

Intrinsic photoconductivity requires the excitation of free electron-hole pairs by a photon whose energy is at least as great as the energy gap. Once the electron-hole pairs are generated by the incoming radiation, electrons and holes will flow to the cathode and anode contacts. The gain of a photoconductor is the ratio of the hole lifetime τ_p to the electron transit time t_r,

$$G = \frac{I}{I_p} = \frac{\tau_p}{t_r} \tag{2.2}$$

and the spectral responsivity can be written as

$$R(\lambda) = (1 - r)\,\eta G\,\frac{\lambda}{1.2398} \tag{2.3}$$

A number of photoconductors are commercially available for the use in various spectral ranges. Silicon is used in the wavelength range of 0.4 to 1.1 μm, cadmium sulphide (CdS) and cadmium selenide (CdSe) are useful in the visible range (0.5 to 0.7 μm), and lead sulphide (PbS), lead selenide (PbSe) and indium antimonide (InSb) in the near infrared range (1 to 3 μm) [76].

Another material which is photo-sensitive in 0.7 to 1.5 μm wavelength range is indium gallium arsenide (InGaAs). This photoconductor is made of either an n or p-type $In_{0.53}Ga_{0.47}As$ conducting layer, with an energy bandgap of 0.78 eV, grown on a semi-insulating substrate of indium phosphide (InP). Under carefully controlled growth conditions, InGaAs has a perfect lattice match to the InP substrate. This match reduces the dislocation density and other crystalline imperfections in the epitaxial layer.

The photoconductive gain G can have values of 10^3 and more. Therefore, in general, the photoconductors are not suitable for a standard cell because the gain of the device is not easily calibrated.

2.4. p-i-n Photodiodes

The first high-speed Si p-i-n photodiode was developed in 1962 [10]. Almost all of the short-wavelength fiber-optic systems use Si p-i-n photodiodes for short-distance communication. They are relatively easy to fabricate, are highly reliable, and have low noise.

The p-i-n device is operated under reverse bias. The cell is designed such that most of the photons are absorbed in the i-region. The photo-generated electrons and holes in the depletion region will be rapidly drawn to the opposite electrodes due to the presence of a high electric field in that region. This leads to current flow in the external circuit. The detection process in p-i-n diodes is very fast and efficient.

A number of reports have already been made on high quality InGaAs p-i-n detectors [11]. The dark current density achieved varies between 1.5×10^{-5} A/cm^2 and 10^{-4} A/cm^2, while effective carrier lifetimes range from

$\tau = 0.3$ μs to 1.7 μs. The quantum efficiency of a top-illuminated diode without antireflection coating is only $\eta \simeq 35\%$ at $\lambda = 1.3$ μm. The primary loss of carriers is due to carrier recombination at the surface and in the emitter. Surface recombination can be reduced by placing an InP cap on top of the emitter layer [12]. InP (with $E_g = 1.3$ eV) is transparent to wavelengths longer than 0.92 μm.

There are two key factors to the improvement of the quantum efficiency of InGaAs diodes: reduce the carrier loss on the surface and in the emitter, and achieve complete depletion in the intrinsic region. To achieve complete depletion, the device must be fabricated from extremely pure material.

2.5. Avalanche Photodiode (APD)

Avalanche photodiodes, similar to p-i-n photodiodes, are operated at high reverse bias voltages. The electric field in the depletion region is high enough that avalanche multiplication takes place. This impact ionization gives rise to internal current gain.

It is considerably harder to fabricate a high quality APD for detecting long-wavelength radiation. The difficulties come from the need to use narrow bandgap material, such as InGaAs and Ge. Narrow bandgap semiconductors have large dark currents at the high reverse biases which are necessary for avalanche breakdown.

2.5.1. Compound Material APDs

Current development of long-wavelength APDs is focused on III-V compound materials. The first InGaAsP APD was reported in 1978 [13]. To reduce the dark current, InGaAsP or InGaAs APDs were grown on wide-bandgap InP substrates. At present, the III-V compound material APD is more sensitive than either a p-i-n photodiode or a photoconductor at high bit rates. Therefore, it is a suitable device for optical communication systems. However, it can not be used as a self-calibrating device because of the high and variable current gain.

2.5.2. Germanium APD

Germanium is another alternative for long-wavelength detection. With an energy bandgap of 0.66 eV at room temperature, it can be designed as a practical photodetector over the 0.7 to 1.5 μm wavelength range. The fabrication processes for Ge photodiodes are straight forward using existing planar monolithic techniques. High quantum efficiency can be achieved by proper design and fabrication.

Several different Ge photodiode structures have been fabricated and studied. An n^+-p structure was developed first [14-17]. Dark currents as low as 1 mA/cm^2 with a quantum efficiency as high as 80% at 1.49 μm have been reported. p^+n Ge photodiodes were also studied [18-22]. The internal quantum efficiency obtained was about 80% at 1.15 μm and the dark current was around 2.8 mA/cm^2. The high dark current occurs because the diffusion constant of p-type impurities, such as zinc, boron, indium and gallium are rather small. High temperatures and long diffusion times are

needed to form the p^+ layer. The high temperature processes cause surface defects which result from the mismatch of the thermal expansion rates of germanium and silicon dioxide (SiO_2). Another kind of Ge photodiode, one with an n^+–n–p structure, was devised to reduce excess noise and improve quantum efficiency [23-25]. A dark current of 5.7 mA/cm^2 and internal quantum efficiency of 70 to 80 percent at 1.15 μm wavelength was obtained. These n^+–n–p structures have a rather deep junction ($x_j = 2.5\mu m$) and, therefore, it is difficult to improve the quantum efficiency.

In optical fiber communication applications, the Ge photodiodes are operated in the avalanche mode in order to obtain a high current gain. Therefore, the major concern for these diodes is to reduce the device noise and thus to improve the S/N ratio.

In this research, we have designed and fabricated a self-calibrating Ge photodiode with a high internal quantum efficiency over the 0.7 to 1.5 μm wavelength range. *The achievement of high quantum efficiency and reduced carrier losses is the primary concern in the design of a self-calibration diode.* In our design, the n^+pp^+ and induced junction structure are chosen because the processing is simple. Ion implantation techniques are used to form the shallow p-n junctions. The details of the design will be discussed in the following chapters.

2.6. Induced Junction Photodiodes

The n^+ layer in induced junction photodiodes is formed by fixed positive charges at the SiO_2–Ge interface. These positive charges invert a lightly doped p-type substrate to a shallow, damage-free n^+ layer at the device

surface. The high induced electric fields associated with induced junction help to collect the photo-generated carriers. The inversion layer cell will be demonstrated to be less sensitive to low lifetimes and high surface recombination velocities than the conventional junction cells [26].

In this research, an induced junction Ge photodiode is fabricated. We will demonstrate that the induced junction cells performs much better than n^+pp^+ diodes.

2.7. Summary

In this chapter, we have discussed various semiconductor photodetectors for use in different spectral ranges. The Si photodiode is the most popular device for the detection of 0.4 to 1.1 μm wavelength radiation. Narrow bandgap materials have to be used for detecting radiation with wavelengths greater than 1.1 μm. Of many possible materials, Ge is used in this research because high quality material is available, the fabrication processes are straight forward, and a high quantum efficiency is achievable by proper design and fabrication.

CHAPTER III
GERMANIUM

3.1. Introduction

A great deal of research work has been carried out on germanium in the past thirty years. In this section, we will review some of its properties.

3.2. General Properties

Ge crystallizes in the diamond lattice with 4.5×10^{22} atom/cm^3. The lattice constant at 20°C is 5.6575 Å, and the expansion coefficient is $5.9 - 6.6\times10^{-6}$/°C [27]. The intrinsic resistivity at 27°C is 47 Ω—cm, corresponding to an intrinsic carrier density of 2.6×10^{13} cm^{-3} [28].

3.3. Band Structure

The energy band structure of Ge, studied by Chelikowsky and Cohen [29] by using pseudopotential calculations, is shown in Fig. 3.1. The maximum of the valence band lies at the center of the Brillouin zone, and the surfaces are approximately spherical. The effective mass of the heavy hole is 0.28 m_o and that of the light hole is 0.04 m_o, where m_o is the mass of free electron. The lowest of conduction band minima are those along the

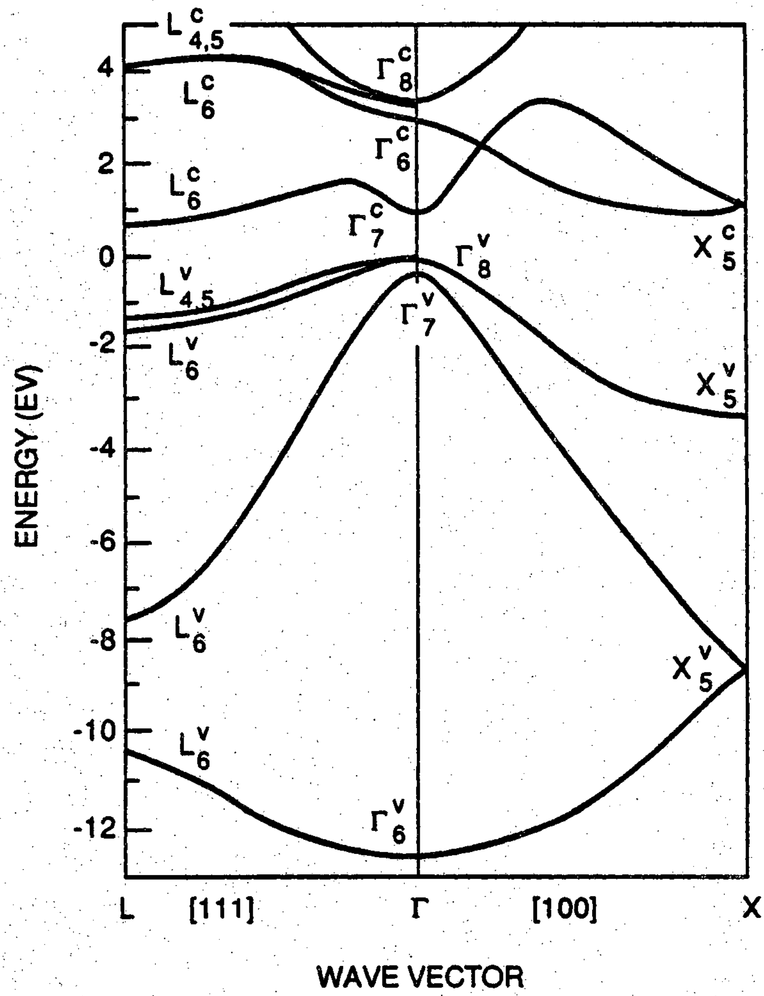

Figure 3.1 Energy band diagram of germanium [29].

[111] direction. The minima are at the zone boundary, so that there are four equivalent minima. The longitudinal effective mass, m_l, and transverse effective mass, m_t, are [30]

$$m_l = 1.6\ m_o\ , \quad m_t = 0.082\ m_o \tag{3.1}$$

3.4. Mobility and Diffusion Coefficient

The mobility μ (μ_n for electron mobility and μ_p for hole mobility) in Ge is dependent on doping concentration and temperature. As the impurity concentration increases, the mobility decreases [31]. The carrier mobility also falls off with a rise in temperature since the thermal vibrations of the lattice atoms increase, causing more intense carrier scattering. In high resistivity Ge, Morin [32] obtains the following empirical relations:

$$\mu_n = 4.90 \times 10^7\ T^{-1.66}\ \ cm^2/V.sec \qquad 100 - 300\ ^oK \tag{3.2}$$

$$\mu_p = 1.05 \times 10^9\ T^{-2.33}\ \ cm^2/V.sec \qquad 125 - 300\ ^oK \tag{3.3}$$

The carrier diffusion coefficient (D_n for electrons and D_p for holes) is another important parameters in semiconductors. In thermal equilibrium, the relationship between D_n and μ_n (or D_p and μ_p) is given by [33]

$$D_n = 2\left(\frac{kT}{q}\,\mu_n\right)\frac{F_{1/2}\left(\dfrac{E_f - E_c}{kT}\right)}{F_{-1/2}\left(\dfrac{E_f - E_c}{kT}\right)} \tag{3.4}$$

where $F_{1/2}$ and $F_{-1/2}$ are Fermi-Dirac integrals. For a nondegenerate semiconductor, where n is much smaller than N_C (or $p \ll N_V$), Eq.(3.4) can

be reduced to

$$D_n = \frac{kT}{q}\,\mu_n \tag{3.5}$$

and similarly,

$$D_p = \frac{kT}{q}\,\mu_p \tag{3.6}$$

which is better known as the Einstein relationship.

3.5. Optical Properties

Fig. 3.2 shows the absorption coefficient of Ge measured by Dash and Newman [34]. Germanium absorbs photons with energy higher than 0.66 eV (corresponding to wavelengths shorter than 1.88 μm). The absorption coefficient starts abrupt rise at about 0.78 eV ($\lambda \simeq 1.59$ μm), which is attributed to the onset of the $\Gamma_8^v - \Gamma_7^c$ direct transition (see Fig. 3.1). The "kink" at 0.87eV ($\lambda \simeq 1.45$ μm) is attributed to the onset of $\Gamma_8^v - X_5^c$ indirect transition.

Free electrons and holes can make a transition from one level to another in the conduction band and valence band by absorbing a photon. This process is referred as free carrier absorption, and can only become significant in heavily doped material. Infrared absorption for a heavily doped p-type sample is seen in Fig. 3.3 [35]. There are three peaks for room temperature measurements. This absorption is due to transitions among the three valence bands shown in Fig. 3.1. Since the absorption coefficient is very small (less than 100 cm^{-1}), this absorption process is negligible.

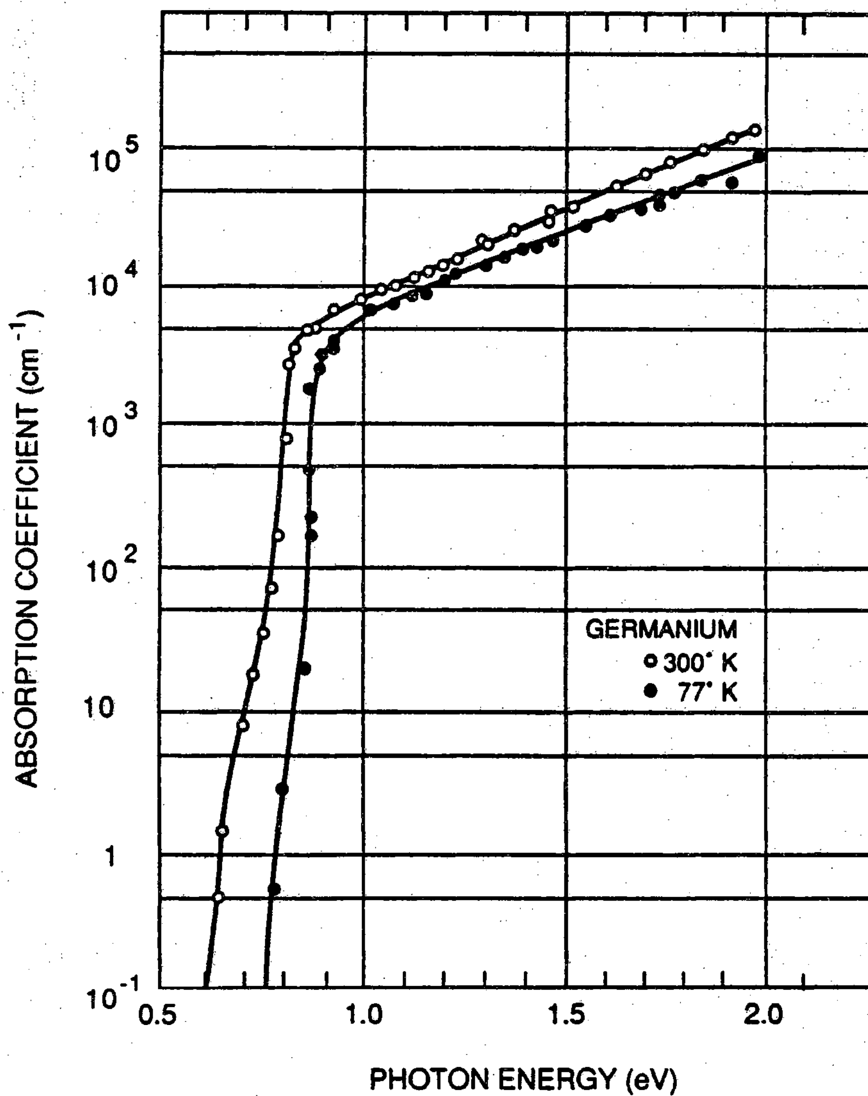

Figure 3.2 Absorption coefficient of single-crystal germanium at 77°K and 300°K [34].

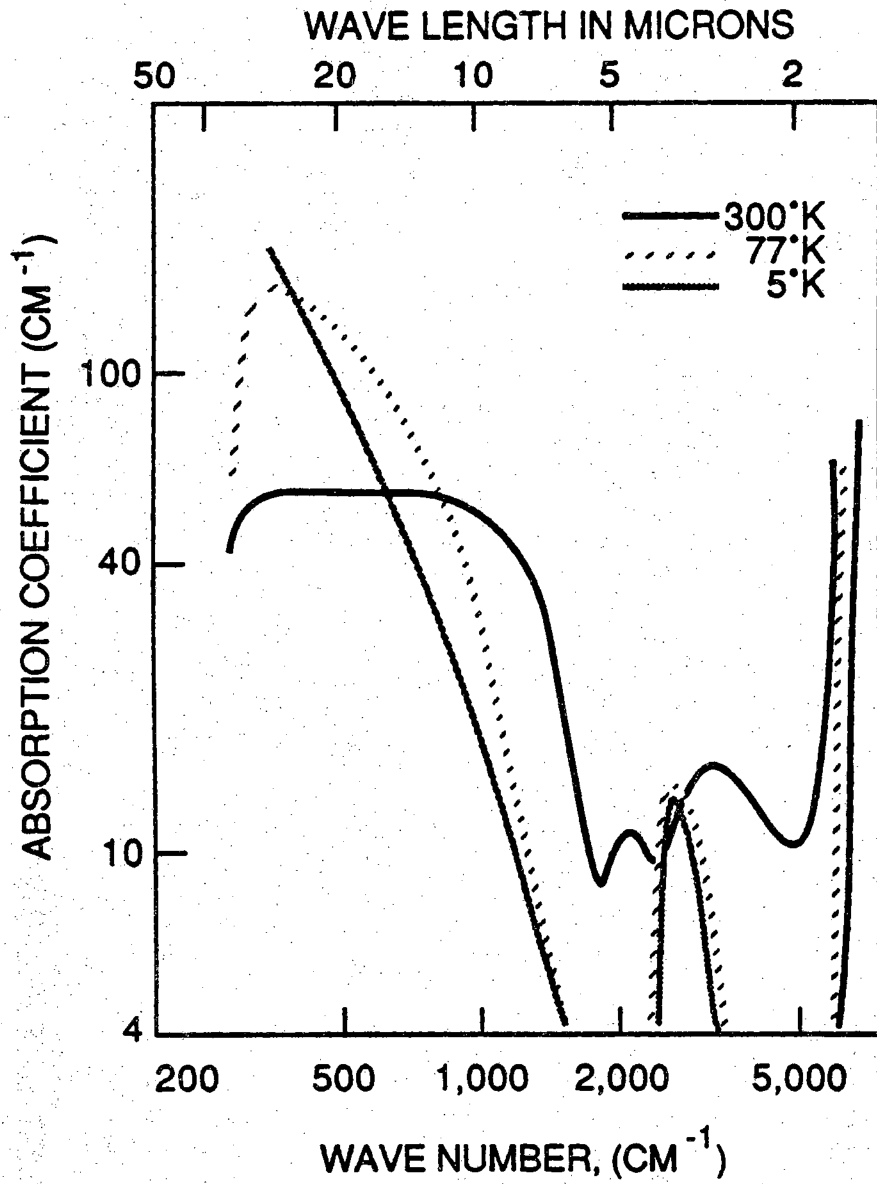

Figure 3.3 Absorption coefficient for p-type germanium with 0.07 Ω-cm resistivity [35].

3.6. Heavily Doped Germanium

In n^+pp^+ photodiodes, the emitters are usually doped heavily to reduce lateral series resistances. The high concentration of impurities produce localized imperfections which are efficient recombination centers. In addition, as the impurity concentration is increased, the energy bandgap is shrunk. The changes of the energy bandgap in heavily doped regions are due to several physical mechanisms. Aigrain [36] has shown that, as the concentration is increased, the impurity states form a band which becomes broader and eventually merges with the nearest intrinsic band edge. This impurity band shifts the majority-carrier band toward the bandgap and leaves the minority-carrier band essentially unchanged. Kane [37] assumes the impurities form clusters, sometimes compounds with semiconductor atoms. These clusters and compounds have potential wells below the band edge and therefore constitute tails of states. Bonch-Bruevich [38] also calculates the distribution of states by taking into account electron-electron interactions and finds that these cause an asymptotic tailing-off of the density of states into the energy gap.

Mahan [39] made a more comprehensive calculation of the energy gap in germanium as a function of the concentration of donor impurities. He has shown that the theoretical energy gap is affected by five important contributions. Three of them for the electrons, as the majority carriers, are the kinetic energy , exchange energy and the self-consistent interaction with the impurities. The two for the holes are the correlation energy with the electron gas and the interaction energy with the screened donors. His theoretical result for the bandgap shrinkage in germanium is

$$\Delta E_g(\mathrm{meV}) = 6.63\times(n/10^{18})^{2/3} - 4.89\times(n/10^{18})^{1/3}$$

$$- 8.2\times(n/10^{18})^{1/4} - 3.0 \qquad (3.7)$$

where n is the electron carrier concentration in the conduction band.

CHAPTER IV
THEORY

4.1. Introduction

In this chapter, the mechanisms which govern photon absorption and carrier collection will be discussed. An analytical expression for the internal quantum efficiency for monochromatic light in a p-n junction photodiode will be derived. Although rather restrictive assumptions are needed to obtain closed form solutions to the differential equations, the use of analytical solutions has proven to be very valuable in the past to predict the behavior of photodiodes, in particular to predict the effect of variations in doping level, lifetime and junction depth.

4.2. Quantum Efficiency

One of the most important figures of merit for photodiodes is the quantum efficiency. The internal quantum efficiency, $\eta(\lambda)$, of a semiconductor photodiode is defined as the ratio of the number of free electron-hole pairs, produced by incident photons of wavelength, λ, that are collected before recombination, to the number of incident photons at the diode surface. There are three mechanisms that govern the quantum efficiency in semiconductor photodiodes [2]:

(1) Absorption rate density, $A(\lambda,x)$, the rate at which photons of wavelength, λ, are absorbed per unit distance at position x in the diodes.

(2) Quantum yield, $Y(\lambda,x)$, the average number of electron-hole pairs produced by one absorbed photon.

(3) Collection efficiency, $P(x)$, the probability that minority carriers generated by absorbed photons at position x will reach the junction before recombination.

Fig. 4.1 shows the cross section of a n^+pp^+ photodiode. If we neglect the absorption of photons in the anti-reflection coating, the internal quantum efficiency can be expressed as

$$\eta(\lambda) = \int_0^H A(\lambda,x)\, Y(\lambda,x)\, P(x)\, dx \tag{4.1}$$

where H is the thickness of the photodiode.

In this section, mathematical expressions for $A(\lambda,x)$, $Y(\lambda,x)$ and $P(x)$ will be discussed. Some approximations will be made to simplify the analysis.

4.2.1. Absorption Rate Density, $A(\lambda,x)$

If r_f, and r_b are defined as the reflectances of front and back surface respectively, and normally incident light is assumed, the photon flux with wavelength, λ, can be expressed as [40]

$$\Phi(x,\lambda) = \Phi_o(\lambda)\, \frac{e^{-\alpha(\lambda)x} + r_b(\lambda)\, e^{-\alpha(\lambda)(2H-x)}}{1 - r_f(\lambda) r_b(\lambda)\, e^{-2\alpha(\lambda)H}} \tag{4.2}$$

Thus, $A(\lambda,x)$ can be written as

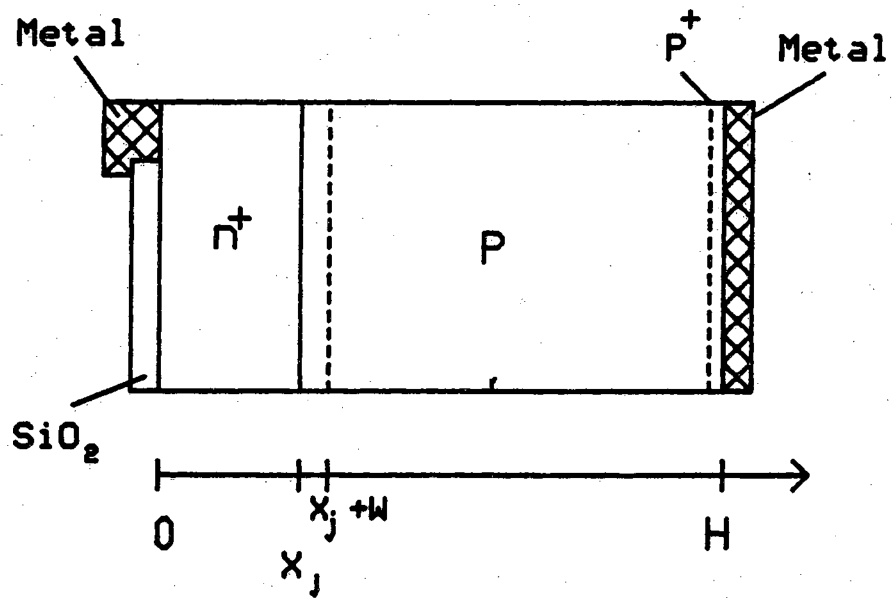

Figure 4.1 Cross section of an n^+pp^+ photodiode.

$$A(\lambda,x) = -\frac{1}{\Phi_o(\lambda)} \frac{\partial\Phi(\lambda,x)}{\partial x}$$

$$= \alpha(\lambda) \frac{e^{-\alpha(\lambda)x} + r_b(\lambda)\, e^{-\alpha(\lambda)(2H-x)}}{1 - r_f(\lambda) r_b(\lambda)\, e^{-2\alpha(\lambda)H}} \tag{4.3}$$

Eq.(4.3) also assumes that the absorption coefficient is independent of position. For a typical diode structure (long-base diode) and range of wavelength (0.7 - 1.5 μm) of interested, the following relation holds:

$$e^{-\alpha(\lambda)H} \ll 1 \tag{4.4}$$

$A(\lambda,x)$ can then be reduced to a simpler form

$$A(\lambda,x) = \alpha(\lambda) e^{-\alpha(\lambda)x} \tag{4.5}$$

However, for the wavelengths longer than 1.5μm, or for a thin diode, Eq.(4.3) must be used for the $A(\lambda,x)$.

4.2.2. Quantum Yield, $Y(\lambda,x)$

The quantum yield $Y(\lambda,x)$ can be thought of as a product of two more fundamental quantities

$$Y(\lambda,x) = Y_\alpha(\lambda,x)\, Y_I(\lambda,x) \tag{4.6}$$

where $Y_\alpha(\lambda,x)$ is the fraction of photons absorbed as a result of generating excess carriers. Some absorption processes, such as free carrier absorption, lattice absorption and impurity absorption, which occur in the far infrared region of the spectrum, do not produce excess carriers. For the region of wavelengths (0.7 - 1.5 μm), these absorption processes are negligible in germanium. Therefore, Y_α is very close to unity.

$Y_I(\lambda,x)$, which is the quantum yield due to impact ionization, is equal to one plus the average extra minority carriers generated by photons. Conservation of energy require the energy of the incident photons be at least two times the bandgap energy. However, impact ionization has not been observed in Ge for photons energy less than three times the bandgap energy, corresponding to $\lambda \leq 0.626$ μm (Fig. 4.2) [41]. Schockley [42] explains this by assuming the equal distribution of energy between minority and majority carriers produced by absorption of photons. Thus, conservation of energy requires photons to have energy more than three times the bandgap energy. For the range of wavelength (minimum of 0.7 μm) that we are interested in, Y_I is equal to 1.

4.2.3. Collection Efficiency, P(x)

The collection efficiency at position x of the photodiode is defined as the probability that a minority carrier created at x will be swept across the junction before recombination. Typically, the collection efficiency is very close to unity in the vicinity of the depletion edge and is reduced considerably in the emitter or near the front surface . The reduction of collection efficiency is mainly attributed to surface and bulk recombination. The recombination rate, U, due to recombination through an energy level within the energy gap can be expressed by the Schockley-Hall-Read model as

$$U = \frac{np - n_{io}^2}{\tau_{po}(n+n_1) + \tau_{no}(p+p_1)} \tag{4.7}$$

where n_1 and p_1 describe the location of the level, and can be expressed as

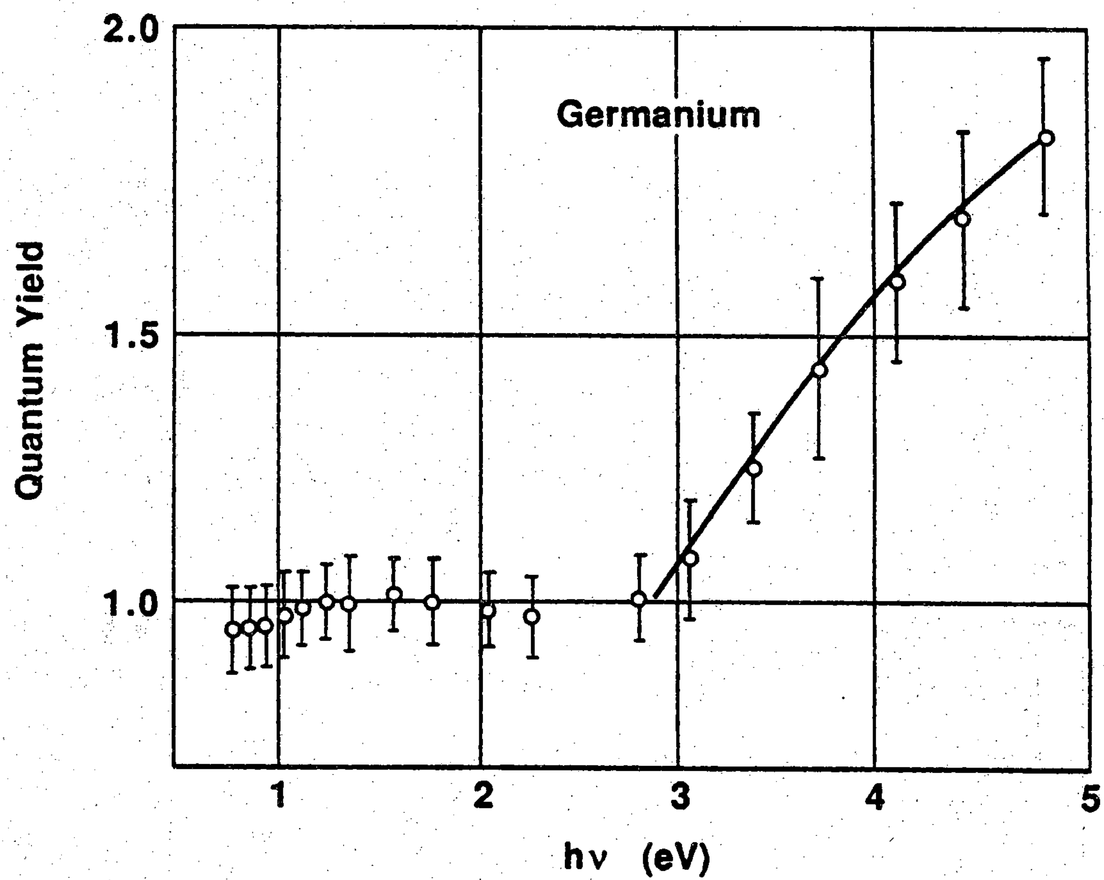

Figure 4.2 Quantum yield in germanium as a function of photon energy [41].

$$n_1 = n_{io}\, e^{\frac{E_T - E_i}{kT}} \tag{4.8}$$

and

$$p_1 = p_{io}\, e^{\frac{E_i - E_T}{kT}} \tag{4.9}$$

where E_T is the trap energy level.

In a heavily doped region, such as the emitter in photodiodes, Auger recombination becomes a significant process [43]. In n-type material, the Auger lifetime is given by

$$\tau_{Auger} = \frac{1}{A_n n^2} \tag{4.10}$$

while in p-type material

$$\tau_{Auger} = \frac{1}{A_p p^2} \tag{4.11}$$

where A_n and A_p are Auger coefficients which are commonly regarded as intrinsic properties of semiconductors.

We have neglected radiative recombination which is too weak to have any significance in indirect bandgap materials, such as germanium.

4.2.4. Internal Quantum Efficiency

In order to obtain an analytical expression for internal quantum efficiency, the following simplified equations are used

$$A(\lambda,x) = \alpha(\lambda)e^{-\alpha(\lambda)x} \tag{4.12}$$

and

$$Y(\lambda,x) = 1 \tag{4.13}$$

Therefore, $\eta(\lambda)$ can be expressed in a integral form as

$$\eta(\lambda) = \int_0^H \alpha(\lambda)e^{-\alpha(\lambda)x}P(x)\, dx \tag{4.14}$$

It is not a easy task to write P(x) in a closed form equation because the collection efficiency is a complicated function of surface conditions, carrier lifetimes, and doping concentrations. A simplified model for P(x) is needed to carry out the integration in Eq.(4.14). For instance, a "dead layer" model in the emitter was used for the approximation solution by Geist [44], or, as will be shown in the following section, one can solve the diode current equation under the assumption of constant doping in the emitter and base regions. Analytical equations are useful to predict the behavior of photodiodes. However, for detailed analysis, a numerical computation has to be used. We will demonstrate the use of a detailed numerical model in Chapter VIII.

4.3. Derivation of the Photocurrent for Monochromatic Light [45]

Before we derive the analytical expressions, the following assumptions are needed:

(1) Neglect the loss of radiation in the anti-reflection coating.

(2) The absorption coefficient, α, is a function of wavelength only.

(3) Every photon absorbed in the semiconductor results in creation of exactly one electron-hole pair; i.e., the free carrier, lattice and impurity absorptions have been neglected.

(4) The derivation is restricted to low-level injection.

(5) On both sides of the junction, the doping concentration is constant, i.e., we assume constant mobility μ and constant diffusion coefficient D.

(6) On both sides of the junction, the minority carrier lifetime τ is constant.

(7) A single trap level is assumed.

(8) There is no back surface reflection in the diode.

Fig. 4.1 shows the cross section of an n^+pp^+ photodiode. When light with wavelength λ is incident on the semiconductor, the photons will be absorbed and electron-hole pairs will be generated. The flux of photons decreases with position as

$$\Phi(\lambda,x) = (1 - r)\ \Phi_o(\lambda)e^{-\alpha(\lambda)x} \tag{4.15}$$

where $\Phi(\lambda,x)$ is number of photons with wavelength λ at position x, r is the reflectance of the device surface, $\Phi_o(\lambda)$ is the incident photon flux density with wavelength λ, and $\alpha(\lambda)$ is the absorption coefficient. Eq. (4.15) has assumed no back surface reflection in the diode. The generation rate of electron-hole pairs, according to assumption (3), is

$$G(\lambda,x) = -\frac{d}{dx}\Phi(\lambda,x) = (1 - r)\ \alpha(\lambda)\Phi_o(\lambda)\ e^{-\alpha(\lambda)x} \tag{4.16}$$

First consider only the emitter region. The continuity equation for holes under steady state condition is

$$\frac{1}{q}\frac{dJ_p}{dx} - G_p + U_p = 0 \tag{4.17}$$

where U_p is the recombination rate due to single level recombination trap in the energy bandgap and is expressed in Eq.(4.7). Under the simplified condition $\tau_{po} \simeq \tau_{no}$, n>>p, and $E_T \simeq E_i$, with assumption (4), Eq.(4.7) can be reduced to

$$U_p = \frac{p_n - p_{no}}{\tau_{po}} \tag{4.18}$$

The current equation for holes in the emitter is

$$J_p = q\mu_p p_n E - qD_p \frac{dp_n}{dx} \tag{4.19}$$

where μ_p is the hole mobility and D_p is the hole diffusion coefficient. The electric field E in Eq. (4.5) is zero because quasi-neutrality is assumed in the emitter and base regions. Substituting Eq.(4.16), (4.18) and (4.19) into (4.17) with constant μ_p and D_p, Eq.(4.17) becomes

$$\frac{d^2(p_n - p_{no})}{dx^2} + \frac{(1-r)\,\alpha\Phi_o e^{-\alpha x}}{D_p} - \frac{p_n - p_{no}}{D_p \tau_{po}} = 0 \tag{4.20}$$

The general solution for Eq.(4.20) is

$$p_n - p_{no} = A\cosh\left(\frac{x}{L_p}\right) + B\sinh\left(\frac{x}{L_p}\right) - \frac{(1-r)\,\alpha\Phi_o\tau_{po}}{\alpha^2 L_p^2 - 1}\, e^{-\alpha x} \tag{4.21}$$

After applying the boundary conditions

$$\frac{d(p_n - p_{no})}{dx} = \frac{S_p}{D_p}(p_n - p_{no}) \qquad \text{at } x=0 \tag{4.22}$$

and

$$p_n - p_{no} = p_{no}(e^{qV/kT} - 1) \qquad \text{at } x = x_j \tag{4.23}$$

The hole current density at the junction edge is

$$J_p(x_j) = -qD_p \frac{d(p_n - p_{no})}{dx}\Big|_{x=x_j}$$

$$= \frac{q(1-r)\Phi_o \alpha L_p}{\alpha^2 L_p^2 - 1} \left\{ \frac{\frac{S_p L_p}{D_p} + \alpha L_p - e^{-\alpha x_j}\left[\frac{S_p L_p}{D_p}\cosh\left(\frac{x_j}{L_p}\right) + \sinh\left(\frac{x_j}{L_p}\right)\right]}{\frac{S_p L_p}{D_p}\sinh\left(\frac{x_j}{L_p}\right) + \cosh\left(\frac{x_j}{L_p}\right)} - \alpha L_p e^{-\alpha x_j} \right\}$$

$$- \frac{qD_p n_{io}^2}{L_p N_D} \frac{\sinh\left(\frac{x_j}{L_p}\right) + \frac{S_p L_p}{D_p}\cosh\left(\frac{x_j}{L_p}\right)}{\cosh\left(\frac{x_j}{L_p}\right) + \frac{S_p L_p}{D_p}\sinh\left(\frac{x_j}{L_p}\right)} (e^{qV/kT} - 1) \tag{4.24}$$

Similarly, one can obtain the electron current density in p-bulk region by solving

$$\frac{d^2(n_p - n_{po})}{dx^2} + \frac{\alpha \Phi_o e^{-\alpha x}}{D_n} - \frac{n_p - n_{po}}{D_p \tau_{no}} = 0 \tag{4.25}$$

with boundary conditions

$$n_p - n_{po} = n_{po}(e^{qV/kT} - 1) \qquad \text{at } x = x_j + W \tag{4.26}$$

and

$$\frac{d(n_p - n_{po})}{dx} = -\frac{S_n}{D_n}(n_p - n_{po}) \qquad \text{at } x=H \tag{4.27}$$

where W is the width of depletion region, H is the width of the entire cell and S_n is electron surface velocity at back side of the cell. The electron current which diffuses to the edge of the depletion region is

$$J_n(x_j+W) = \alpha D_n \frac{d(n_p - n_{po})}{dx}\bigg|_{x=x_j+W}$$

$$= \frac{q(1-r)\Phi_o \alpha L_n}{\alpha^2 L_n^2 - 1} e^{-\alpha(x_j+W)}$$

$$\times \left\{ \alpha L_n - \frac{\sinh\left(\frac{H-x_j-W}{L_n}\right) + \frac{S_n L_n}{D_n}\cosh\left(\frac{H-x_j-W}{L_n}\right) + \left(\alpha L_n - \frac{S_n L_n}{D_n}\right) e^{-\alpha(H-x_j-W)}}{\frac{S_n L_n}{D_n}\sinh\left(\frac{H-x_j-W}{L_n}\right) + \cosh\left(\frac{H-x_j-W}{L_n}\right)} \right\}$$

$$- \frac{qD_n n_{io}^2}{L_n N_A} \frac{\sinh\left(\frac{H-x_j-W}{L_n}\right) + \frac{S_n L_n}{D_n}\cosh\left(\frac{H-x_j-W}{L_n}\right)}{\frac{S_n L_n}{D_n}\sinh\left(\frac{H-x_j-W}{L_n}\right) + \cosh\left(\frac{H-x_j-W}{L_n}\right)} (e^{qV/kT} - 1) \tag{4.28}$$

The photocurrent generated in the space charge region can be written as

$$J_d = q\Phi_o e^{-\alpha x_j}(1 - e^{-\alpha W}) \tag{4.29}$$

The total current J at a given wavelength λ is then the sum of Eq.(4.24), (4.28) and (4.29).

$$J = J_p + J_n + J_d \tag{4.30}$$

If $\Phi_o(\lambda)$ is set to zero, J is then reduced to the conventional diode current equation as

$$J = J_o\,(e^{qV/kT} - 1) \tag{4.31}$$

where

$$J_o = \frac{qD_p n_{io}^2}{L_p N_D}\;\frac{\sinh\left(\dfrac{x_j}{L_p}\right) + \dfrac{S_p L_p}{D_p}\cosh\left(\dfrac{x_j}{L_p}\right)}{\cosh\left(\dfrac{x_j}{L_p}\right) + \dfrac{S_p L_p}{D_p}\sinh\left(\dfrac{x_j}{L_p}\right)}$$

$$+ \frac{qD_n n_{io}^2}{L_n N_A}\;\frac{\sinh\left(\dfrac{H-x_j-W}{L_n}\right) + \dfrac{S_n L_n}{D_n}\cosh\left(\dfrac{H-x_j-W}{L_n}\right)}{\dfrac{S_n L_n}{D_n}\sinh\left(\dfrac{H-x_j-W}{L_n}\right) + \cosh\left(\dfrac{H-x_j-W}{L_n}\right)} \tag{4.32}$$

The internal quantum efficiency, $\eta(\lambda)$, of a photodiode is defined as the ratio of the number of free electron-hole pairs, produced by incident photons of wavelength λ, that are collected before recombination, to the number of incident photons at the diode surface. Thus,

$$\eta = \frac{J_L}{q\,(1 - r)\,\Phi_o} \tag{4.33}$$

where J_L is the light-generated current density. J_L is the sum of the terms in the braces in Eq. (4.24) and (4.28), and Eq. (4.29). Therefore, $\eta(\lambda)$ can be written as

$$\eta = \frac{\alpha L_p}{\alpha^2 L_p^2 - 1} \left\{ \frac{\dfrac{S_p L_p}{D_p} + \alpha L_p - e^{-\alpha x_j} \left[\dfrac{S_p L_p}{D_p} \cosh\left(\dfrac{x_j}{L_p}\right) + \sinh\left(\dfrac{x_j}{L_p}\right) \right]}{\dfrac{S_p L_p}{D_p} \sinh\left(\dfrac{x_j}{L_p}\right) + \cosh\left(\dfrac{x_j}{L_p}\right)} \right.$$

$$+ \frac{\alpha L_n}{\alpha^2 L_n^2 - 1} e^{-\alpha(x_j + W)}$$

$$\times \left\{ \alpha L_n - \frac{\sinh\left(\dfrac{H - x_j - W}{L_n}\right) + \dfrac{S_n L_n}{D_n} \cosh\left(\dfrac{H - x_j - W}{L_n}\right) + \left(\alpha L_n - \dfrac{S_n L_n}{D_n}\right) e^{-\alpha(H - x_j - W)}}{\dfrac{S_n L_n}{D_n} \sinh\left(\dfrac{H - x_j - W}{L_n}\right) + \cosh\left(\dfrac{H - x_j - W}{L_n}\right)} \right\}$$

$$+ e^{-\alpha x_j} (1 - e^{-\alpha W}) \tag{4.34}$$

Figure 4.3 shows the measured internal quantum efficiency of a n^+pp^+ photodiode, compared with the theoretical calculation by Eq.(4.34). The emitter of this photodiode is formed by the double As implantation with dosage/energy of 6×10^{14} cm^{-2}/40KeV and 2×10^{15} cm^{-2}/70KeV on a 0.1 Ω-cm p-Ge substrate. The device parameters in Eq.(4.34) are listed in Table

Table 4.1 Device parameters

Variable	Value
Base	p-Ge, 0.1 Ω—cm
Thickness	300 μm
Doping concentration	$5\times10^{16}/cm^3$
Emitter	
Junction	Step
Junction depth	0.75 μm
Doping concentration	$2\times10^{19}/cm^3$
Carrier lifetime for electrons, τ_n	5.5 μ sec
Carrier lifetime for holes, τ_p	5 n sec
Surface recombination velocity	2×10^6 cm/sec

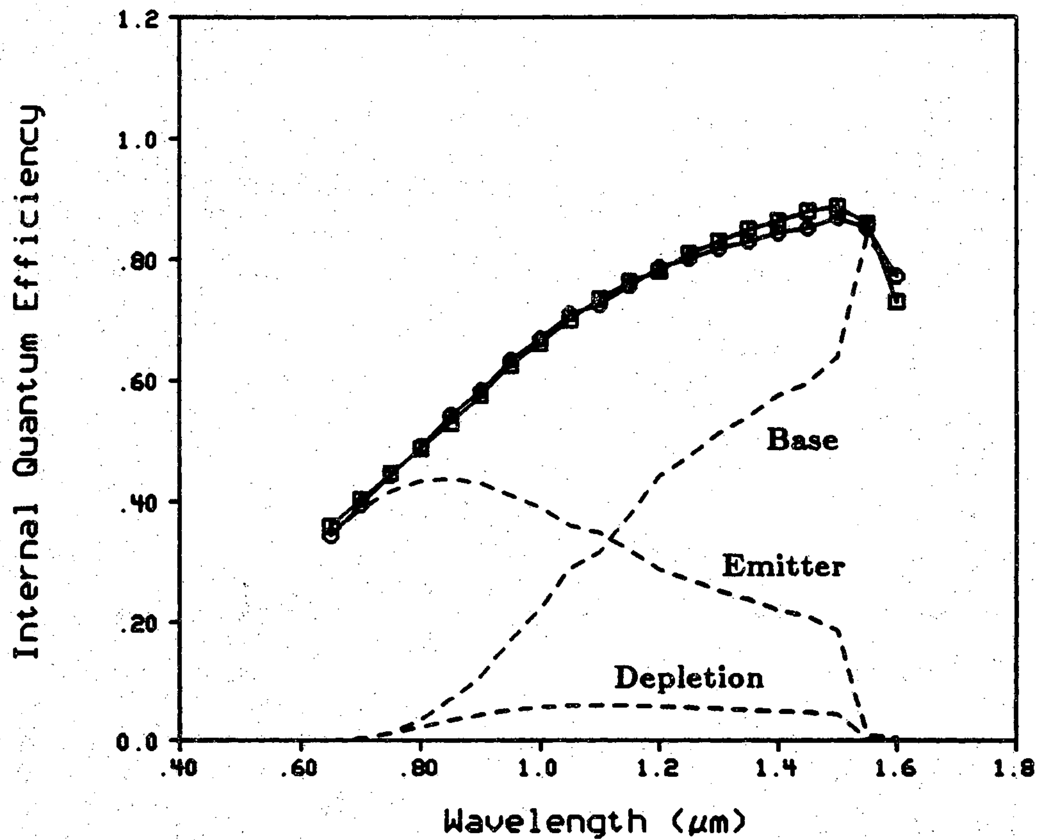

Figure 4.3 Measured (□) and calculated (○) internal quantum efficiency of an n^+pp^+ photodiode. The dashed lines are the three components of the internal quantum efficiency expressed by Eq. (4.34). The device parameters are shown in Table 4.1.

4.1. Good agreement between the measured data and theoretical calculation is shown in the figure. The dashed lines in the figure illustrate the three components of the quantum efficiency in Eq.(4.34) contributed by the carrier collection from the emitter, base, and space charge region.

Figure 4.4 shows the effect of the emitter junction depth on the internal quantum efficiency. This figure shows that the quantum efficiency can be close to unity if x_j is reduced to 0.1 μm or less. Figure 4.4-6 also illustrates the change in the three components in the quantum efficiency due to a change of x_j. The high quantum efficiency in the shallow emitter diode (Fig. 4.6) is due to the fact that most of the incident photons are absorbed in the base region where carrier lifetime is longer.

The surface recombination velocity affects the carrier collections, especially for those generated near the surface by the short wavelength radiation. Fig. 4.7 illustrates the quantum efficiency varies with the front surface recombination velocity S_p. This calculation indicates that the surface of the cell needs to be passivated to reduce the surface state density, and consequently, reduce the S_p.

We have demonstrated the usefulness of the analytical solution of internal quantum efficiency. This solution gives us quick information about the diode characteristics. In many semiconductor diodes, however, the doping concentration in the emitter is not constant, and the mobility μ and diffusion coefficient D vary with position as well. Therefore, computer simulation becomes a essential tool for any accurate description of diode characteristics.

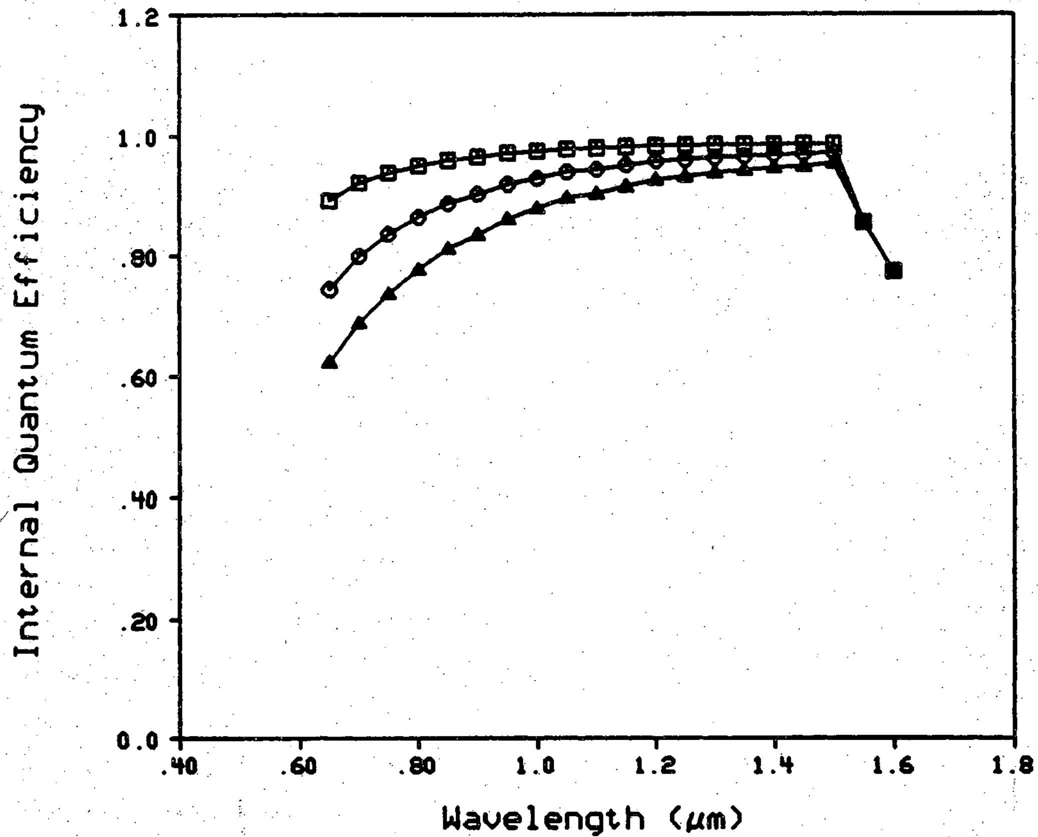

Figure 4.4 Calculated internal quantum efficiency of n^+pp^+ photodiodes with emitter junction depth $x_j = 0.1$ μm (□), $x_j = 0.2$ μm (○), and $x_j = 0.3$ μm (△). The device parameters are shown in Table 4.1.

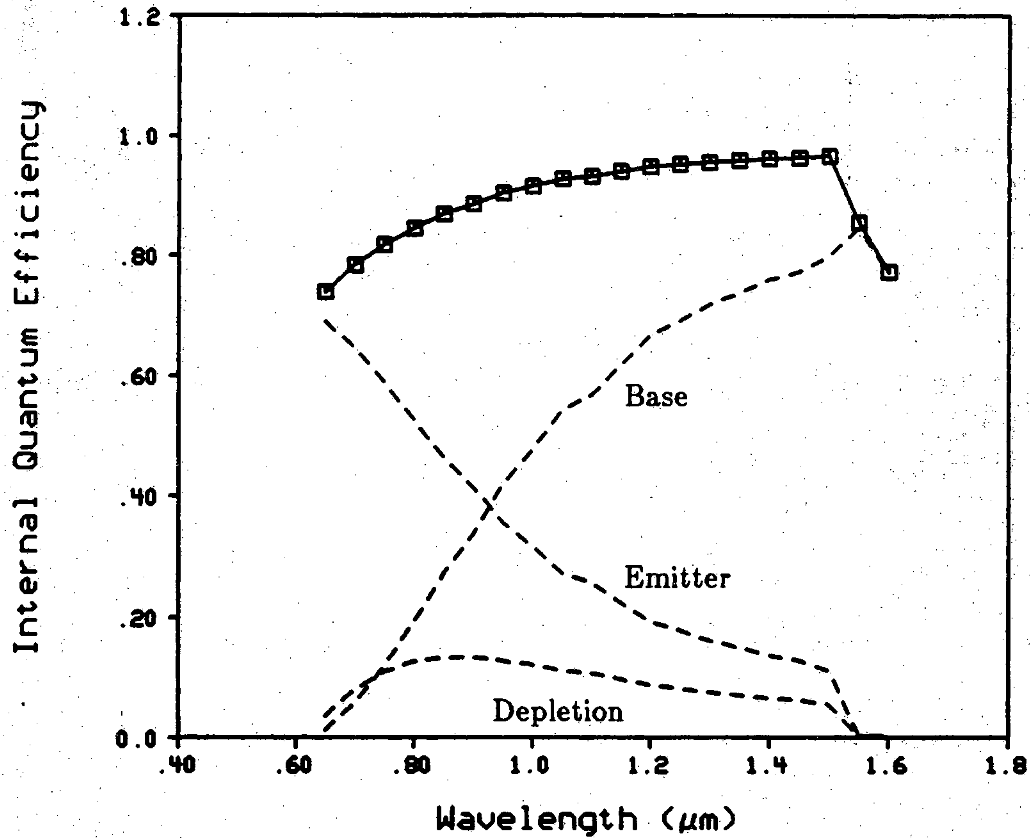

Figure 4.5 Computed (□) internal quantum efficiency of an n^+pp^+ photodiode with $x_j = 0.3$ μm. The dashed lines are the three components of internal quantum efficiency expressed by Eq.(4.34). The diode parameters are shown in Table 4.1.

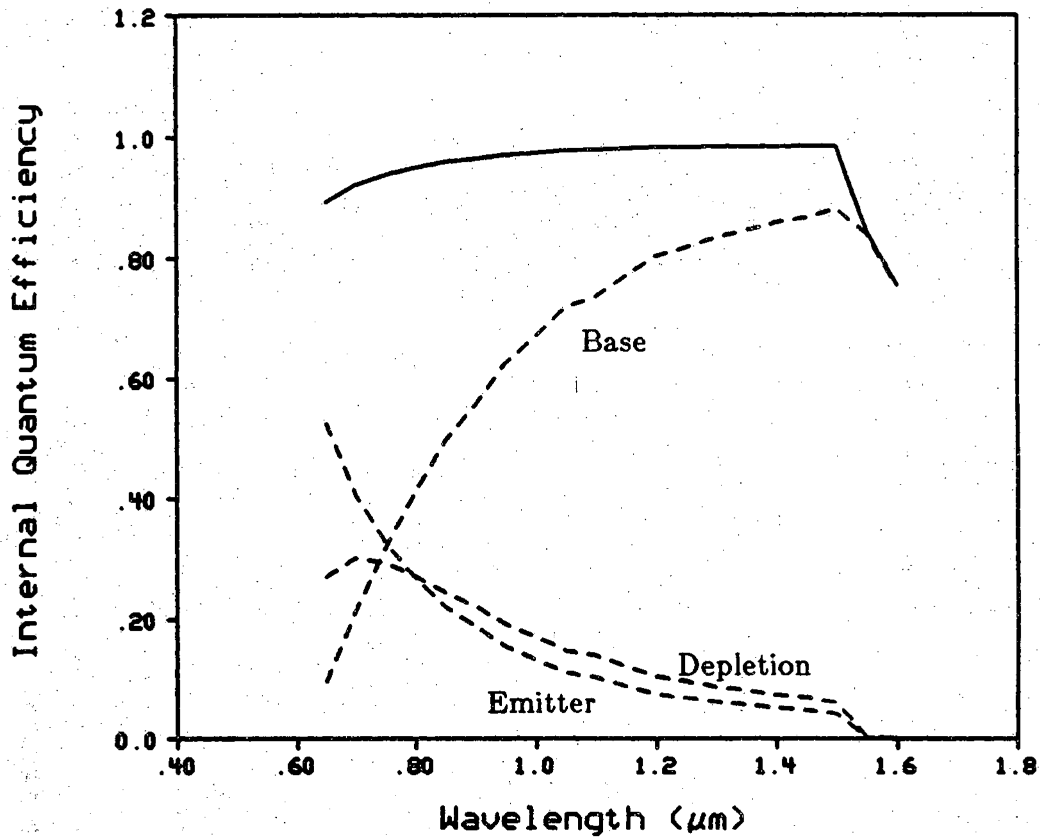

Figure 4.6 Computed (solid line) internal quantum efficiency of an n^+pp^+ photodiode with $x_j = 0.1$ μm. The dashed lines are the three components of internal quantum efficiency expressed by Eq.(4.34). The diode parameters are shown in Table 4.1.

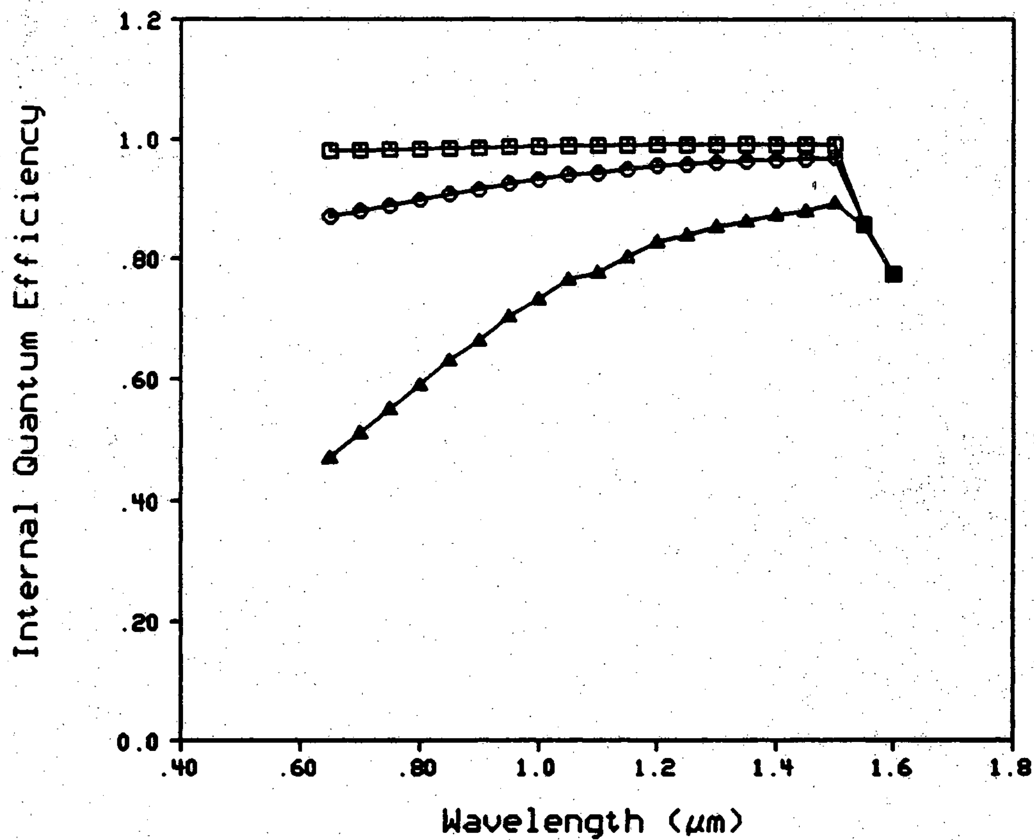

Figure 4.7 Computed internal quantum efficiency of an n^+pp^+ photodiode with $S = 10^3$ cm/sec (□), $S = 10^5$ cm/sec (○), and $S = 10^6$ cm/sec (△). The device parameters are shown in Table 4.1.

4.4. Surface Effects

As mentioned in the last section, the shallow junction depth in an n^+pp^+ is essential for high internal quantum efficiency, especially for the collection of carriers generated by the short wavelength photons. However, the crystal damage introduced during the implantation is high, which results in a decreased carrier lifetime This limits the maximum collection efficiency which can be achieved. An alternative approach to this problem is to use a n-type inversion layer induced by fixed positive charges in the SiO_2. In this device, the induced n^+-layer region is damage-free so that carriers have longer lifetime. Also, the induced electric field helps to collect the photon-generated carriers and improves the collection efficiency.

The induced junction diode can be analyzed based on standard MOS theory [57]. Fig. 4.8 shows the charge distribution and the energy band diagram in the SiO_2-Ge region. Assuming a one-dimensional structure, the expressions of the charge density, the electric field, and the potential as a function of position in the induced junction diode can be obtained by solving Poisson's equation. The Poisson's equation is

$$\frac{d^2V}{dx^2} = -\frac{\rho}{K_s\epsilon_o} = -\frac{q}{K_s\epsilon_o}(p - n + N_D - N_A) \tag{4.35}$$

It is convenient to introduce the dimensionless quantities U's as

$$U(x) = [E_i(bulk) - E_i(x)]/kT \tag{4.36}$$

$$U_{Fn}(x) = [E_i(bulk) - E_{Fn}(x)]/kT \tag{4.37}$$

$$U_{Fp}(x) = [E_i(bulk) - E_{Fp}(x)]/kT \tag{4.38}$$

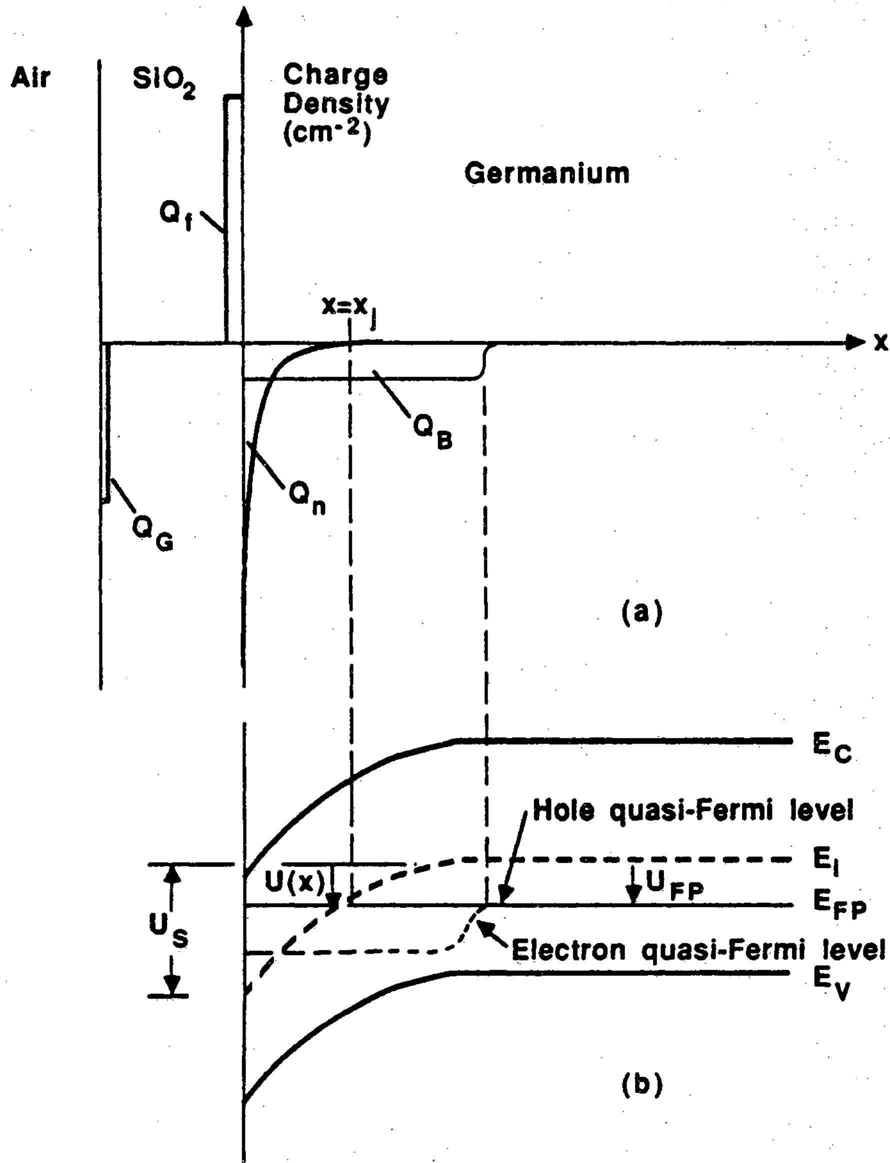

Figure 4.8 (a) Charge distribution in an induced junction diode and (b) energy band diagram near the surface.

$$U_s = [E_i(\text{bulk}) - E_{is}]/kT \tag{4.39}$$

where $E_i(x)$, $E_{Fn}(x)$, $E_{Fp}(x)$, and E_{is} are the intrinsic energy level, quasi-Fermi level for electrons, quasi-Fermi level for holes, and the intrinsic energy level at surface, respectively. Therefore, the electron and hole concentrations can be expressed in terms of the U's as

$$n(x) = n_i\, e^{[U(x) - U_{Fn}(x)]} \tag{4.40}$$

and

$$p(x) = n_i\, e^{[U_{Fp}(x) - U(x)]} \tag{4.41}$$

We assume charge neutrality in the bulk of the device, i.e.

$$\rho\,(x{=}\infty) = 0 = p_{bulk} - n_{bulk} + N_D - N_A \tag{4.42}$$

and, therefore,

$$N_D - N_A = n_{bulk} - p_{bulk}$$

$$= -\,2\, n_i \sinh(U_{Fp}) \tag{4.43}$$

where we have assumed $U_{Fn} = U_{Fp}$ at $x = \infty$. Substitute Eq.(4.43) into (4.35) and normalize the potential V, Eq.(4.35) becomes

$$\frac{d^2U(x)}{dx^2} = \frac{2}{L_D}\left[e^{[U(x)-U_{Fn}]} - e^{[U_{Fp}-U(x)]} + 2n_i \sinh(U_{Fp})\right] \tag{4.44}$$

where L_D is the intrinsic Debye length and is defined as

$$L_D = \left(\frac{kT\epsilon_o K_s}{2q^2 n_i}\right)^{1/2} \tag{4.45}$$

Multiply by $\left(\frac{dU}{dx}\right)$ on both sides of the Eq.(4.44) and use

$$\frac{dU}{dx}\frac{d}{dx}\left(\frac{dU}{dx}\right) \equiv \frac{1}{2}\frac{d}{dx}\left(\frac{dU}{dx}\right)^2$$

together with the boundary conditions E=0 and U=0 at x=∞, to get

$$\left[\frac{dU(x)}{dx}\right]^2 = \frac{1}{L_D^2}\left\{ e^{-U_{Fn}}\left[e^{U(x)} - 1\right] + e^{U_{Fp}}\left[e^{-U(x)} - 1\right] + 2U(x)\sinh(U_{Fp})\right\} \quad (4.46)$$

The electric field E(x) in the semiconductor can be expressed as

$$E(x) = \frac{kT/q}{L_D} F\left[U_{Fn}, U_{Fp}, U(x)\right] \quad (4.47)$$

where

$$F\left[U_{Fn}, U_{Fp}, U(x)\right] = \left\{ e^{-U_{Fn}}\left[e^{U(x)} - 1\right] + e^{U_{Fp}}\left[e^{-U(x)} - 1\right] + 2U(x)\sinh(U_{Fp})\right\}^{1/2} \quad (4.48)$$

The variable x can be obtained by integrating Eq.(4.47) as

$$x = L_D \int_{U_s}^{U(x)} \frac{dU'(x)}{F\left[(U_{Fp}, U_{Fn}, U'(x)\right]} \quad (4.49)$$

The total charge in the SiO_2-Ge system should be

$$Q_f + Q_n + Q_B + Q_G = 0 \quad (4.50)$$

where Q_f is the fixed charges in the SiO_2, Q_n is the inversion charge at surface, Q_B is the depletion charge, and Q_G is the induced charge at SiO_2 surface (see Fig. 4.8). If the SiO_2 is thick enough, Q_G can be neglected [46]. Therefore,

$$Q_f = -(Q_n + Q_B) \tag{4.51}$$

>From the Gauss's law,

$$E_s = \frac{Q_f}{K_s\epsilon_o} \tag{4.52}$$

i.e.,

$$Q_f = \frac{kT}{q}\frac{K_s\epsilon_o}{L_D} F[U_{Fn}, U_{Fp}, U_s] \tag{4.53}$$

Eq. (4.40), (4.41), (4.47), (4.49), and (4.53) are the complete descriptions of the induced junction diode. The results of the theoretical calculations under low-level injection condition, shown in Fig. 4.9-11, indicate that induced junction diodes typically have shallow junctions ($\simeq$ 0.2 μm, Fig. 4.9), high inversion carrier concentration (Fig. 4.10) and high electric field at the surface (Fig. 4.11). This calculation is based on $U_s = 12$ which corresponds to a fixed charge density of $1.85\times10^{11}/cm^2$.

4.5. Summary

In this chapter, we have described the mechanisms which govern the internal quantum efficiency. A analytical expression of quantum efficiency for constant doping in the emitter and base region was derived. The theoretical calculation indicates that a shallow emitter and passivated surface are essential for a high quantum efficiency n^+pp^+ photodiode. The high electric field in a direction to aid the collection of carriers, plus the damage-free shallow emitter make the induced junction cell better able to tolerate low carrier lifetime and high surface recombination velocity than the n^+pp^+ junction cells.

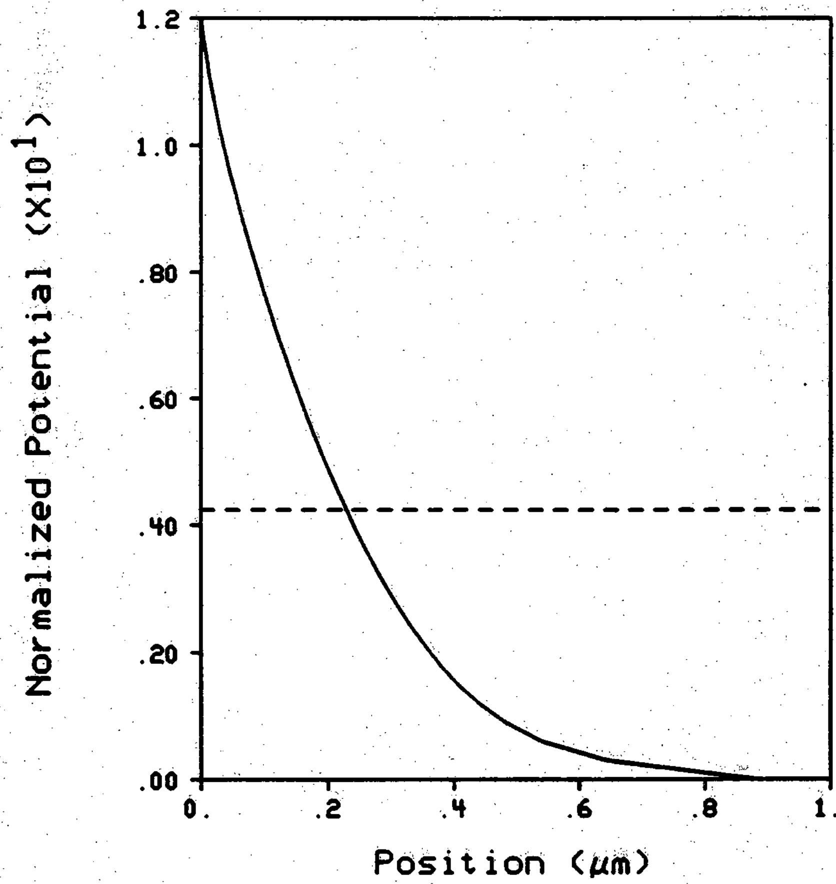

Figure 4.9 The normalized potential as a function of position with U_s = 12. The dashed line is the Fermi level.

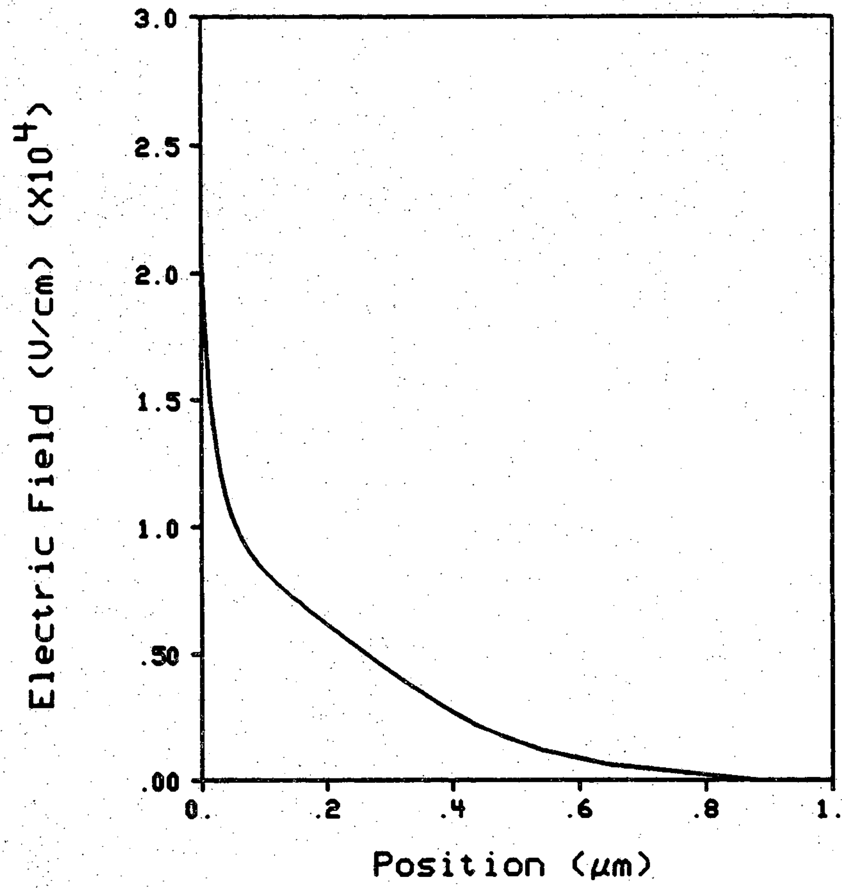

Figure 4.10 The electric field as a function of position with $U_s = 12$.

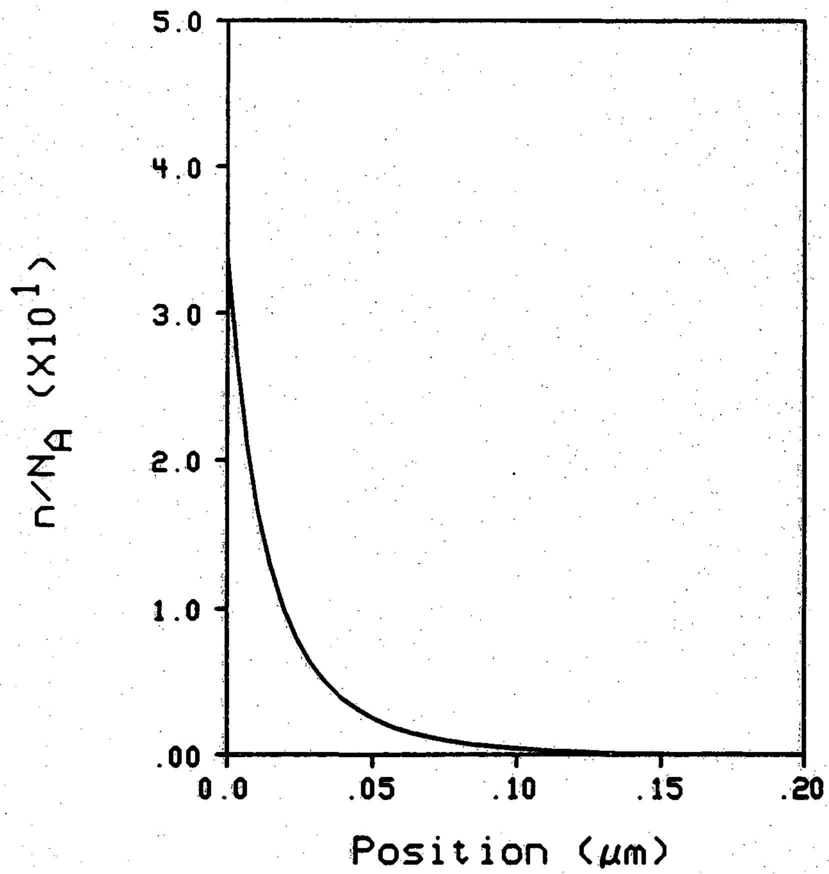

Figure 4.11 The normalized electron carrier concentration as a function of position with $U_s = 12$.

CHAPTER V
DESIGN CONSIDERATIONS

5.1. Introduction

In this chapter, the design of an optimal germanium photodiode for radiometric applications is discussed. The main concerns are to have low leakage current which will reduce the noise, and high quantum efficiency. Small series resistance is also desired for diodes operating under high intensity flux conditions.

5.2. Leakage Current

For an ideal diode, the dark current density can be written as

$$J = J_0(e^{qv/KT} - 1) \tag{5.1}$$

where J_0, in the simplest case of no heavy doping effects, constant doping, and long emitter and base width, is

$$J_0 = \frac{qn_{i0}^2 D_p}{N_D L_p} + \frac{qn_{i0}^2 D_n}{N_A L_n} \tag{5.2}$$

One would expect J_0 to decrease as the doping concentrations of the two sides of the junction are increased. However, as the doping density is

increased, other parameters become adversely affected. The diffusion lengths are reduced in heavily doped regions because of reductions in lifetime and mobility. The reduction in mobility is due to the increase of impurity scattering of carriers. As a result, the diffusion coefficient decreases accordingly. The lifetime is dependent on doping level and free-carrier concentration. In heavily doped regions, the lifetime can be dominated by Auger recombination.

Band gap narrowing (BGN) becomes significant in heavily doped regions. The intrinsic concentration n_{i0}^2 in Eq.(2) needs to be replaced by n_{ie}^2 where

$$n_{ie}^2 = n_{i0}^2 \, e^{\frac{\Delta_G}{KT}} \tag{5.3}$$

where Δ_G is the effective band gap narrowing for various heavy doping effects [47]. Heavy doping effects can result in an increase in n_{ie}^2 of an order of magnitude or more.

In practical diodes, it is necessary to make trade-offs among parameters in order to obtain optimal devices. Usually the emitters are doped heavily to reduce the series resistance and base regions are doped intermediately to improve minority carrier lifetime.

5.3. Quantum Efficiency

Quantum efficiency is the single most important photodiode parameter for radiometric applications. As mentioned in chapter IV, with quantum yield $Y(\lambda,x)$ set to 1, the internal quantum efficiency is

$$\eta(\lambda) = \int_0^H \alpha(\lambda) e^{-\alpha(\lambda)x} P(x)\, dx$$

$$= \int_0^{x_j} \alpha(\lambda) e^{-\alpha(\lambda)x} P(x)\, dx + \int_{x_j}^H \alpha(\lambda) e^{-\alpha(\lambda)x} P(x)\, dx \qquad (5.4)$$

where H is the thickness of the diode and P(x) is the collection efficiency. Eq.(5.4) shows that the internal quantum efficiency depends on many parameters, such as the thickness, H, of the device, the absorption coefficient α, the emitter junction depth x_j, and the collection efficiency P(x), therefore, the carrier lifetime. We shall examine these parameters and determine how to optimize the design for maximum $\eta(\lambda)$.

5.3.1. Device Thickness

First we need to have H large enough to absorb most of the radiation. Germanium is an indirect band gap material. As a consequence, the absorption coefficient $\alpha(\lambda)$ of the band edge absorption ($\lambda \simeq 1.8$ μm) increases relatively slowly compared with that of direct band gap material (see Fig. 2.1). Relatively thick germanium must be used to absorb this radiation. For the λ from 0.7 t0 1.5 μm where the absorption coefficient is larger than 5×10^3 cm^{-1}, over 99.99% of the radiation is absorbed after propagating 20 μm into germanium. However, for the λ greater than 1.6 μm where the absorption coefficient drops to below 100 cm^{-1}, part of the photons will transmit through the device. Usually, for fabrication convenience, the thickness of the wafer is much thicker, typically 250 - 300 μm. This thickness guarantees nearly total absorption of radiation over the 0.7 to 1.5 μm wavelength range.

5.3.2. Collection Efficiency P(x)

Collection efficiency can be improved by reducing the loss of free carriers. The carrier losses due to recombination may occur at the front surface, in the emitter, or in the base region.

5.3.2.1. Front Surface

The imperfections on the surface of semiconductor serve as the source of generation-recombination centers. If the density of such states is N_{ss} cm^{-2}, the recombination rate at the surface can be described in terms of a surface recombination velocity

$$S = \sigma_s v_{th} N_{ss} \tag{5.5}$$

where σ_s is the capture cross section of surface states, and v_{th} is the thermal velocity of the carriers. The value of S is extremely sensitive to surface conditions. Among various surface treatments, thermal oxidation has been proved to be advantageous in device stability and performance [48]. GeO_2-Ge surfaces have attracted less attention than, say SiO_2-Ge because the water solubility of GeO_2 prevents its use as an effective passivation agent. Chemically vapor deposited SiO_2 can be used as a passivation layer.

5.3.2.2. Emitter

The emitter of a n^+pp^+ diode may be formed by implantation, using a high energy ion beam of the dopant. The use of implantation techniques has several advantages over the traditional diffusion method. For example, the beam energy can be used to control the depth of the p-n junction, and the

ion dosage concentration can be used to control the doping profile. The implantation produces considerable damage in the implanted areas so that the sample must be annealed after implantation.

Usually, the emitters are doped heavily to reduce the series resistance. As a consequence, heavy doping effects, plus the damage due to the implantation, severely degrade the collection efficiency in the emitter. Therefore, the contribution from the first term in Eq.(5.4) to the internal quantum efficiency is small because of small P(x). In order to improve the total quantum efficiency, a shallow emitter junction is used. In the shallow emitter diode, a larger fraction of the carriers are generated in the base region and, therefore, have better chance to be collected. The calculations in chapter IV demonstrated that the emitter junction depth must be 0.1 μm or less to be suitable for the use as an self-calibrating detector.

5.3.2.3. Base

Shockley-Read-Hall recombination is the most dominant recombination process in the base region. The choice of the base resistivity is determined by the relations between carrier lifetime, junction depth, base thickness, and leakage current. In general, high resistivity substrates are desired for our work. The minority carrier lifetime in the base region is high due to the lightly doped substrate. In addition, the breakdown voltage of this diode is also high. The high breakdown voltage gives us one additional degree of freedom to operate the diode. Under reverse biased conditions, the high electric field in the space charge region helps to sweep the photogenerated carriers to the depletion edge and where they can be collected.

A lightly doped substrate is desired for the induced junction diode as well. It is easier for the fixed positive charges in the SiO_2 to induce a n-type inversion layer on a lightly-doped substrate.

5.3.2.4. Back Surface

In silicon photovoltaic devices, the presence of a minority carrier block built-in field at the back surface of a conventional diode immensely enhances the cell performance [49]. This back-surface-field (BSF) is formed by a high-low junction. The electric field created by the high-low junction will direct the minority carriers toward the depletion region, and reduce the carrier recombination at the back surface. This process, consequently, increases the collection efficiency. The high-low junction is most effective in a thin base device where the minority carrier diffusion length is much larger than the base width.

In our work, ion implantation is used to form a thin p^+ layer at the back surface of the germanium photodiodes. This p-p^+ junction reduces the surface recombination velocity of minority carriers and also provides a good ohmic contact for majority carriers.

5.4. Summary

In order to obtain an absolute radiometric detector, a careful design of the photodiode is necessary. Basically, the design has to minimize minority carrier loss in the device. The device must be passivated to reduce the recombination at the front surface. At the back surface, a high-low junction is needed to form a potential barrier for the minority carriers. A shallow

emitter is essential also for a high quantum efficiency cell. A high resistivity substrate is used because of the high carrier lifetime in the lightly-doped material. In the next chapter, the fabrication processes needed to implement these design principles are discussed.

CHAPTER VI

FABRICATION OF GERMANIUM PHOTODIODES

6.1. Introduction

In this chapter, the fabrication procedures for Ge photodiodes will be discussed. The fabrication processes required the adaptation of existing Si planar monolithic techniques to germanium. Nearly every step required some special adaptation to make the process suitable for use on a germanium device.

6.2. Wafers

The Ge wafers were are p-type, (111) orientation, 2" in diameter and have resistivities ranging from 0.1 to 40 Ω-cm. The thickness of the wafers is about 300 μm, which is thick enough to ensure total absorption over the wavelengths of interest. The wafers were chemically and mechanically polished. Both sides of the wafers are polished.

6.3. Photolithography

Photolithography is the process of transferring a specific patterns to the surface of a semiconductor wafer. These patterns define various parts of the device, such as the impurity doping areas and metal interconnections.

In our work, the mask patterns were drawn using the graphic software CMASK. These patterns were then reduced to the actual size and transferred to photosensitive glass plates. In the photolithographic process, photoresist is applied to define the specific patterns. KTI negative photoresist and AZ1350 positive photoresist were used for this purpose.

6.4. Oxidation

Imperfections on the Ge surface serve as the source of the generation-recombination centers. The surface condition can be characterized by the surface recombination velocity, S. The value of S is extremely sensitive to surface conditions. Therefore, surface passivation is very important for the device performance. In silicon devices, a thin film of SiO_2 is used very successfully to passivate the surface. Finding a suitable passivating film for germanium was a key issue in this work. This passivation film is also used as an insulating layer, as a diffusion and ion-implantation mask, and as a capping layer over the doped region to prevent outdiffusion during thermal annealing cycles.

GeO_2 has the serious disadvantage of being somewhat water soluble. It causes unstabilities in the cleaning and etching steps necessary for planar fabrication techniques. This undesired property also prevents its use as an effective passivation agent because of the presence of moisture in the atmosphere.

Many films, including SiO_2, Si_3N_4, Al_2O_3 and combinations of these materials have been the subject of intensive studies by many researchers [50]. These films were compared with respect to their etch rate, dopant

masking capabilities, mechanical stress, and oxygen and water permeability. SiO_2 has proven to have the most favorable properties. SiO_2 is effective not only for masking against ion implantation, but also in reducing the surface state density at the SiO_2—Ge interface.

There are two prime candidates for SiO_2 deposition on Ge: sputter deposition and chemical vapor deposition (CVD). Many of the other technique which as used to deposit or grow SiO_2 on Si are not appropriate to deposition on germanium.

6.4.1. Sputtered SiO_2

The sputter deposition is undertaken at room temperature using an ion mill technique. This film is uniform over the entire wafer. However, there are several disadvantages which limit its application:

(1) The growth rate of the sputtered film is low. The typical deposition rate is less than 100 Ä/min. It takes about 90 minutes to grow a 8000 Å film, the thickness is required to effectively mask the ion implanted impurities. This slow throughput will seriously limit its application in production.

(2) A complicated mixture of Si, Ge, and O is formed at the SiO_2-Ge interface. This Si-Ge-O mixture is difficult to etch and produces severe problems in processing, such as the SiO_2 undercutting and photoresist lifting. It was found that the problem can be resolved by depositing a layer of CVD SiO_2 between the Ge substrate and sputtered SiO_2.

6.4.2. Chemical Vapor Deposition (CVD)

Many other methods are available for the deposition of SiO_2 films. However, CVD techniques are most frequently used in semiconductor processing because of the relative ease of deposition and the high quality of the resulting films.

The deposition of SiO_2 by reacting dichlorosilane with nitrous oxide at 900°C at low pressure is given by [51]

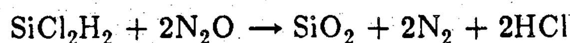

$$SiCl_2H_2 + 2N_2O \rightarrow SiO_2 + 2N_2 + 2HCl$$

This method gives excellent quality SiO_2 with good uniformity. However, since the reaction takes place at 900°C, which is too close to the melting point of Ge (950°C), this method was not used.

The decomposition of tetraethoxysilane, $Si(OC_2H_5)_4$, abbreviated as TEOS, in a low pressure reactor is another common technique for depositing SiO_2 films [52]. The processing takes place at 650 to 750°C with the following reaction

$$Si(OC_2H_5)_4 \rightarrow SiO_2 + \text{by products}$$

The advantage of TEOS deposition are excellent uniformity, conformal step coverage, and good film quality. The disadvantages are the high-temperature process and liquid source requirements.

In this work, the SiO_2 films were formed by reacting silane and oxygen at a temperature of 400°C. The main advantages of the silane-oxygen reaction are the relatively low deposition temperature, and the fact that the deposition can be carried out at atmospheric pressure. The SiO_2 layer is formed on the surface of a wafer which is placed on a hot plate and heated

to about 400°C. The chemical reaction is as following:

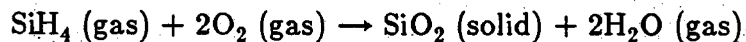

$$SiH_4 \text{ (gas)} + 2O_2 \text{ (gas)} \rightarrow SiO_2 \text{ (solid)} + 2H_2O \text{ (gas)}$$

The deposition rate is a function of the silane partial pressure. The deposition rate is around 1000 Å/min.

6.4.3. SiO_2-Ge Interface

At the germanium-silicon dioxide interface, the material composition of the interfacial region is single-crystal germanium, covered by the amorphous SiO_2. Various charges and traps are associated with this transition region.

The imperfection of the crystal structure at the SiO_2-Ge interface produces surface states and affects the ideal characteristics of the device. These states are located in the energy bandgap of germanium, and can exchange charge with germanium thus acting as carrier recombination centers. These states come from several sources, including structural defects and metal impurities. A CV measurement technique is typically used to determine the density of surface states [53].

Studies of fixed charge, Q_f, have been concentrated on the SiO_2-Si interface. It has been suggested that excess silicon or deficient oxygen that results from a nonstoichiometric silicon-oxygen structure at the SiO_2-Si interface is the origin of the fixed oxide charge [54]. Only a few studies have been done on the SiO_2-Ge interface. However, by analogy, it is quite possible that, at the SiO_2-Ge interface, the fixed charge is the result of the excess germanium and/or silicon in the SiO_2 which is formed during the CVD oxidation and/or post-implant anneal. Typical values of Q_f range from $3\times10^{11}/cm^2$ to $8\times10^{12}/cm^2$ [50,55,56].

In the present work, we have not attempted to maximize Q_f of the induced junction photodiode. The following information about the fixed oxide charge at SiO_2-Si interface [54,57] may be helpful in the future study of SiO_2-Ge interface:

(1) Q_f is fixed positive charge, very close to the SiO_2-Si interface. It cannot be charged or discharged.

(2) Q_f is independent of the oxide thickness, the semiconductor doping concentration, and the semiconductor doping type.

(3) Its value is a function of substrate orientation, the final oxidation and the anneal conditions.

6.5. Ion Implantation

The p^+ channel stop and n^+ emitter (see Fig. 6.8) are formed by ion implantation. The use of implantation techniques has several advantages over the traditional diffusion method. In the ion implantation process, the doping parameters can be precisely controlled. For example, the beam energy can be used to control the depth of the p-n junctions, and the ion dosage concentration can be used to control the doping concentration.

6.5.1. Implantation Impurities

For a high quantum efficiency n^+pp^+ photodiode, a shallow n^+ emitter region is essential. Arsenic ions ($^+As^{75}$) which is relatively large and heavy has a small projected range R_p [58] when implanted into a Ge substrate. Small R_p yields a shallow n^+ junction. Since the diffusivity coefficient of As in Ge is relatively small ($\simeq 4\times10^{-13}$ cm^2/sec at 700°C), the arsenic layer can

be annealed at a high temperature with very little change in doping profile. Therefore, As is suitable for the shallow emitter dopant.

Phosphorus can be used as a n^+ dopant for a deep junction because of its light atomic weight and deeper projected range R_p [58]. However, in heavily phosphorus-doped Ge samples, post-implant anneal caused cracking on the surface. Dislocations are probably caused by the misfit of the germanium and phosphorus atoms in heavily doped samples. The cracking results in the high leakage currents. Phosphorus cannot be used in radiometric diodes. Therefore, arsenic was used as the n^+ impurity for both deep and shallow junctions.

Boron is used as the p^+ dopant for the channel stop on the front surface and high-low junction on the back of the device. Since B^+ implantation at room temperature does not produce amorphous layers, high temperature annealing is required to break the Ge-Ge bonds for activating boron. In addition, the channeling effect is more severe for the light B^+ ion. This problem can be alleviated by using the molecular species BF_3 [59]. The heavy BF_3 ion creates an amorphous zone in the bombarded areas, and the disassociation of the B and F in BF_3 upon the atomic scattering gives a low energy boron dosage and thus shallow junctions.

6.5.2. Implantation Annealing

The ion implantation process produces considerable lattice damage. This damage results in a degradation of material parameters such as mobility and minority carrier lifetime. In addition, only part of the implanted ions reside in the substitutional sites where they are electrically

active. Complete recovery of lifetime, mobility and carrier activation could be achieved by melting the semiconductor so as to return to its single-crystalline state. Practical thermal anneal cycles can only partially remove the lattice damage. Therefore, the minority carrier lifetime in the implanted region is much shorter than that in the base region.

In the fabrication of a germanium diode, the post-implantation anneal is essential to bring the impurities to the proper lattice sites. We use a conventional thermal anneal in our work. The samples are placed in the furnace at 700°C for 20 minutes in an Argon ambient. Before the anneal, the samples were capped with a SiO_2 layer to prevent impurity outdiffusion. The results of this approach will be shown in the following section.

6.5.3. Implantation Diagnosis

Several techniques have been developed for monitoring the impurity profiles and activation of implanted semiconductor samples. Rutherford Backscattering Spectroscopy (RBS) and Secondary Ion Mass Spectroscopy (SIMS) are the most commonly used for the depth profiles of the impurity concentration. Since these two techniques are not available to us, we used spreading resistance and four-point-probe measurements to obtain the doping profiles and monitor the impurity activation instead.

6.5.3.1. Spreading Resistance Technique

The spreading resistance technique is a method used to obtain quantitative measurement of the local resistivity of semiconductor material. If the carrier mobility is known, a corresponding impurity concentration can be calculated. This technique is very sensitive to local impurity

concentrations, therefore, high spatial resolution is obtainable. However, this measurement must be evaluated through the use of a calibration curve produced by making spreading resistance measurements on samples of known resistivity and doping.

In a spreading resistance measurement of a doping profile, an ion implanted sample is bevelled at a small angle to the original surface. The measurement profiles are obtained by stepping the probe points from the surface down to the substrate. For a bevelled sample, the calculation of the corresponding dopant profile is complicated. Usually a multilayer model is assumed and numerical analysis is used to deduce a dopant profile [60].

Fig. 6.1-5 show the spreading resistance measurements on samples with different background concentration and ion implantation conditions. The samples were subjected to a thermal anneal at 700°C for 20 minutes after the implantation. During the anneal, the samples were capped with SiO_2 to prevent impurity outdiffusion. These figures show that arsenic implanted with energy of 70 Kev produces a junction depth of 1.2 μm which is suitable for the deep n^+ region underneath the metal contacts. For shallow junctions of 0.5 μm or less, however, the implant energy has to be less than 35 Kev. All the spreading resistance measurements were conducted by Solecon Laboratories.

6.5.3.2. Four Point Probe Technique

The only readily available tool for monitoring the thermal annealing process in our lab is the four-probe sheet resistivity measurement. The sheet resistance R_s is given by

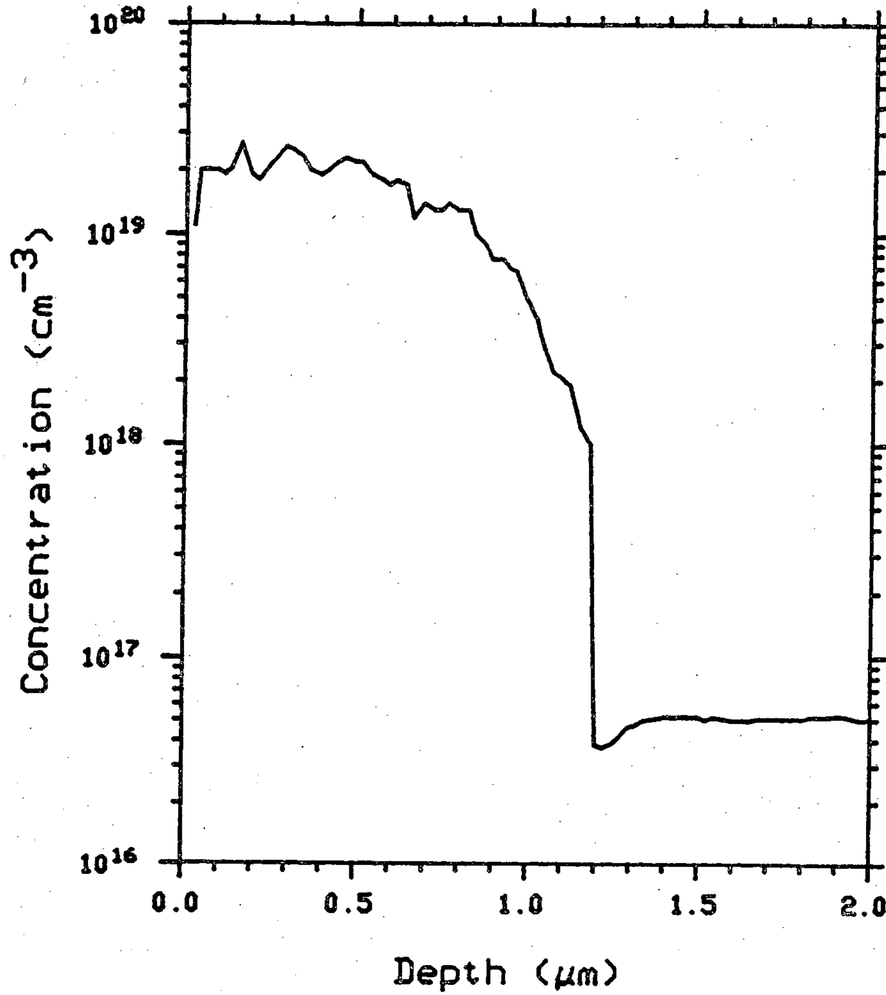

Figure 6.1 Measured carrier concentration profile of implanted arsenic with dosage/energy of $2{\times}10^{15}$ cm^{-2}/70 KeV and $6{\times}10^{14}$ cm^{-2}/40 KeV on a 0.1 Ω-cm germanium substrate.

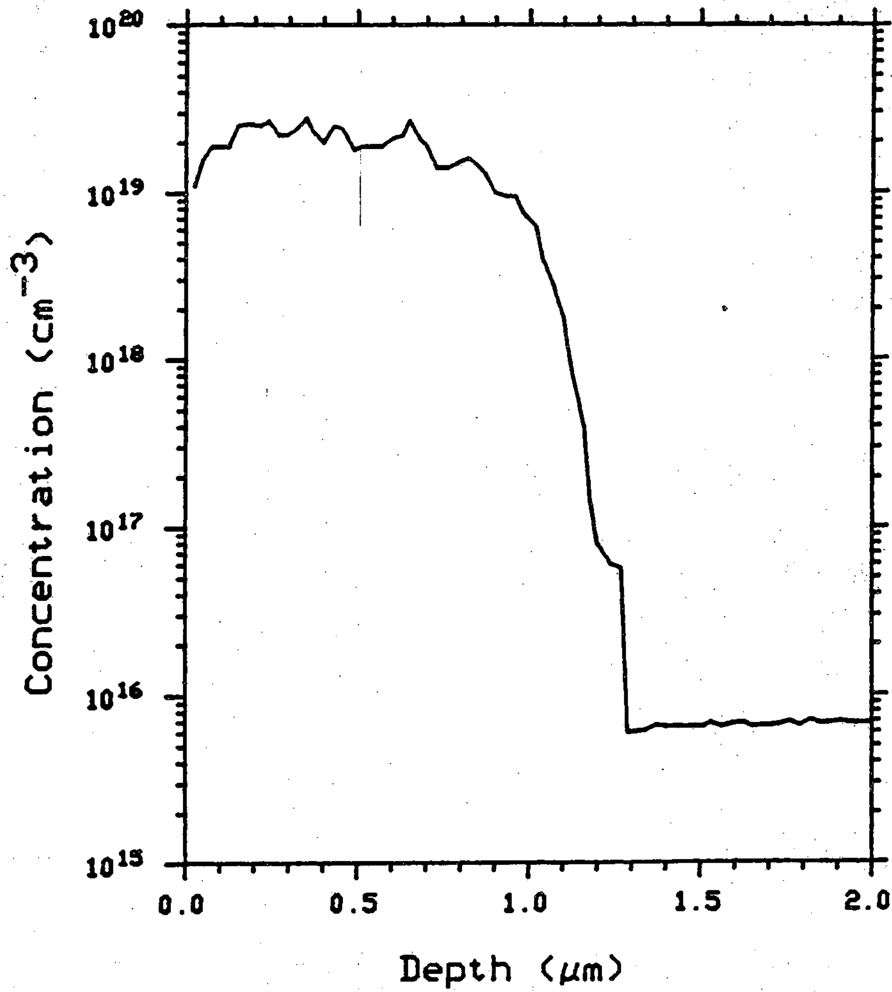

Figure 6.2 Measured carrier concentration profile of implanted arsenic with dosage/energy of 5×10^{15} cm^{-2}/70 KeV on a 0.5 Ω-cm germanium substrate.

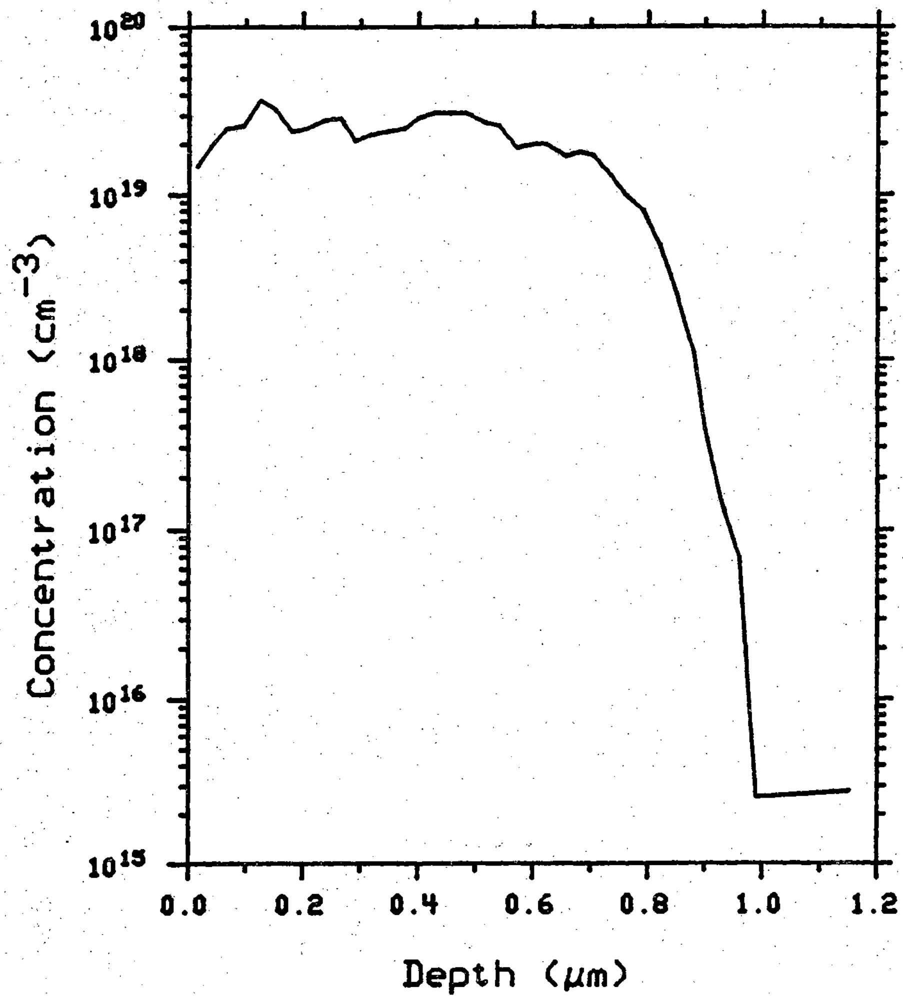

Figure 6.3 Measured carrier concentration profile of implanted arsenic with dosage/energy of 5×10^{15} cm^{-2}/70 KeV on a 1.0 Ω-cm germanium substrate.

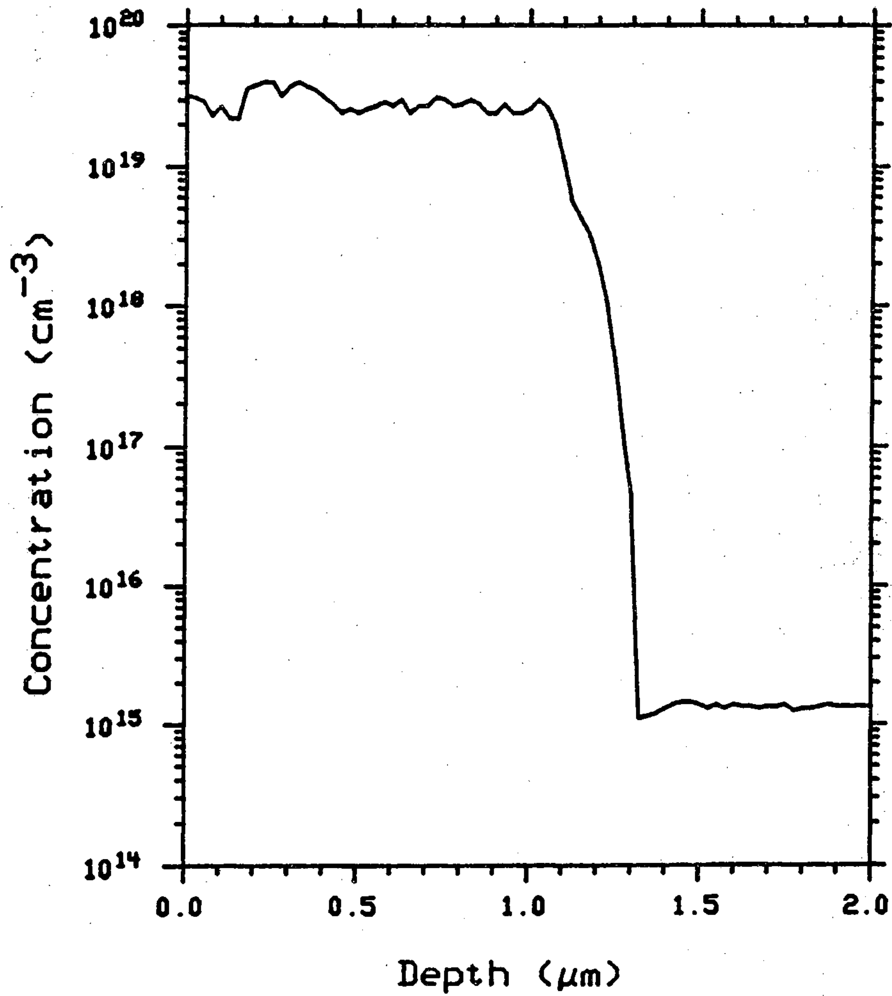

Figure 6.4 Measured carrier concentration profile of implanted arsenic with dosage/energy of 5×10^{15} cm^{-2}/70 KeV on a 2.0 Ω-cm germanium substrate.

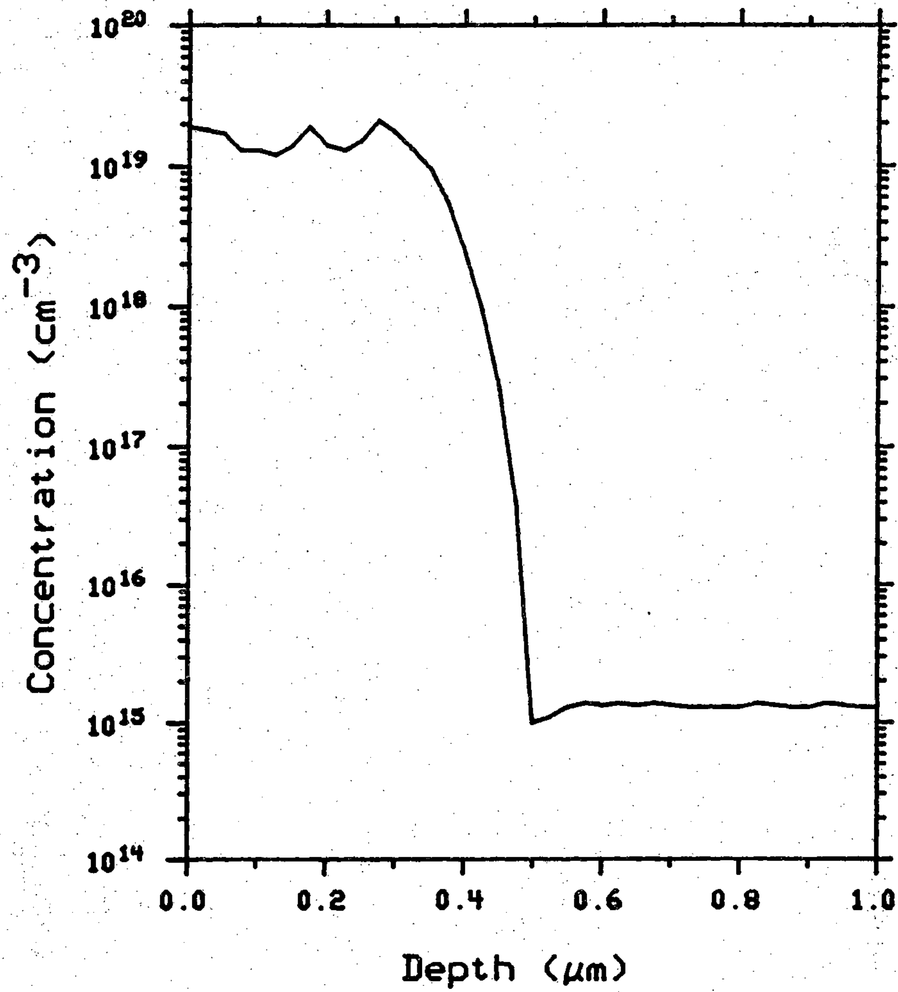

Figure 6.5 Measured carrier concentration profile of implanted arsenic with dosage/energy of 5×10^{15} cm^{-2}/35 KeV on a 2.0 Ω-cm germanium substrate.

$$R_s = \frac{V}{I} \, CF \tag{6.1}$$

where I is the forcing current in two outer probes, V is the measured voltage drop across the two inner probes, and CF is the correction factor. This constant is a function of sample size, shape and the probe spacing [61].

For a given doping profile, the sheet resistance is related to the junction depth x_j, the carrier mobility μ, and the impurity concentration N(x) by the following expression:

$$R_s = \frac{1}{q \int_0^{x_j} \mu[N(x)] \, N(x) \, dx} \tag{6.2}$$

The N(x) in Eq.(6.2) is a function of the impurity concentration in substitutional sites. Therefore, the four point probe sheet resistance measurement provide a simple means of checking the degree of the electrical activation in implanted samples after thermal annealing.

Several samples with different resistivity and implant conditions were prepared for annealing experiments. The impurity activation was monitored by the four-point-probe measurement. The results are shown in Fig. 6.6. Together with the spreading resistance measurement, the percentage of the impurity activation can be estimated. With the 700°C for 20 minutes thermal annealing, more than 50% of the impurities have been activated.

6.6. Metalization

Metalization brings the internal electrical properties to the outside world. High quality metalization requires low-resistance interconnections, and low-resistance contacts to n^+ and p^+ semiconductors. In addition, the

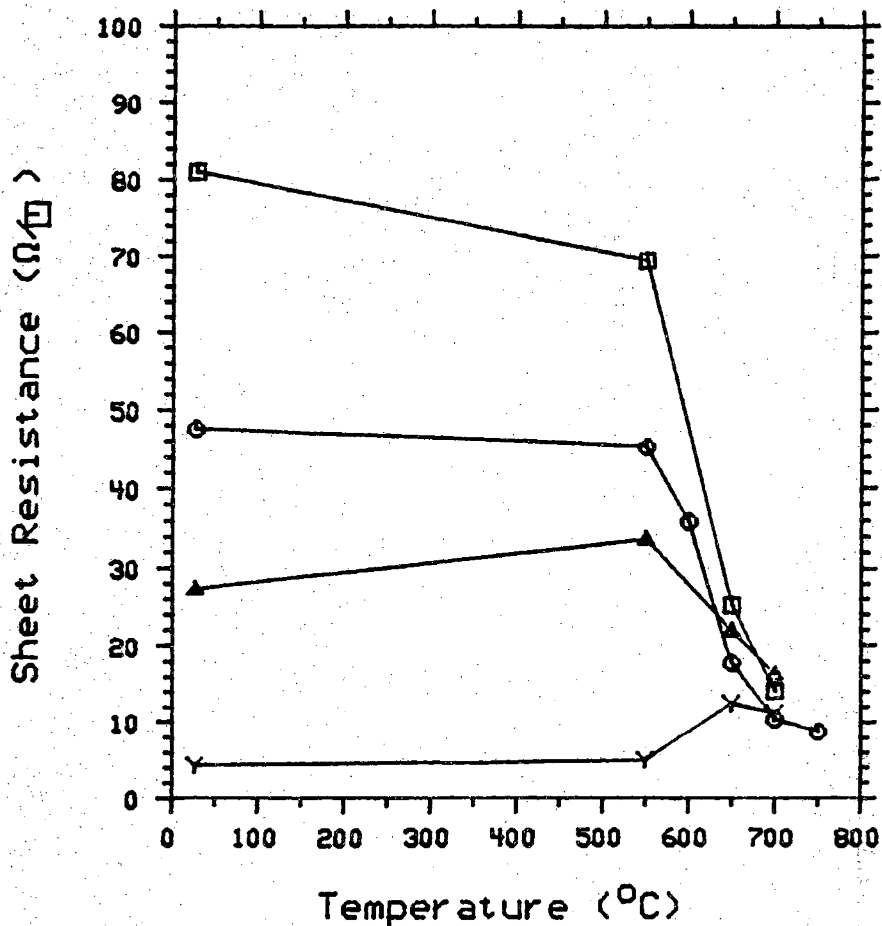

Figure 6.6 Sheet resistivity versus anneal temperature for arsenic implants with dosage/energy of $5\times10^{15}cm^{-2}$/70KeV on 2 Ω-cm (□), $5\times10^{15}cm^{-2}$/70KeV on 1 Ω-cm (○), $5\times10^{15}cm^{-2}$/70KeV on 0.5 Ω-cm, (△), $2\times10^{15}cm^{-2}$/70KeV and $6\times10^{14}cm^{-2}$ /40KeV on 0.1 Ω-cm (Y), germanium substrate.

metal adherence should be high , and electromigration and corrosion should be low under use.

In our research, a three layer Ti/Pd/Ag metal is used for the interconnections. The Ti makes a low resistance ohmic contact to the germanium and the Ag provides electrical conductivity. The Pd in the middle is to prevent an electrochemical reaction that takes place between Ti and Ag in the presence of moisture. This is the conventional metal contact system used in high quality silicon solar cells. The ion beam sputter technique is used for metal deposition.

6.6.1. Sputtering System

The sputtering system used in our research is the Commonwealth Scientific Ion Millitron II, the ion beam milling and coating system. The ion mill has the capability of sputter coating and etching in the same low pressure chamber. In this system, ionized Argon gas (Ar^+) is accelerated to a high energy and bombards a metal target which is located in a low pressure chamber. Through the momentum transfer, the surface of the target atoms become volatile, and are then transported to the substrate surface. Sputter metalization is a clean process and the thickness of the metal layer can be precisely controlled. The sputtering rate can be controlled by the ion beam current and the duration of the deposition. A typical metal deposition rate is about 60 Å/min.

6.6.2. Deposition Procedures

The germanium substrate is cleaned before being placed in the deposition chamber. Any residuals remaining in the contact window areas will degrade the metal adhesion and increase contact resistance. The most common cleaning process involves the use of buffered HF to remove the thin residual oxide, followed by an extensive DI water rinse and N_2 blow dry. The substrates are loaded into the ion mill chamber shortly after the cleaning process.

Prior to the metal deposition, the accelerated Argon gas is directed to the substrate for a short period of time (typically, 30 seconds). This process is referred to as the sputter etching. Sputter etching may further remove the residual film from contact window areas and enhance the contact between the metal and germanium.

The metal patterns are defined by a lift-off process. This process is attractive if an unusual alloy is used. In lift-off the inverse pattern is formed by lithography using AZ1350 positive photoresist, followed by a metal deposition. The whole wafer is then immensed into a warm acetone solvent and the undesired metal will be lifted off the wafer and only the desired metal will remain.

6.6.3. Post-metalization Annealing

A potential barrier may still exist between metal and germanium after the metalization. This potential barrier may be due to a thin layer of GeO_2 resulting from the deionized water rinse and exposure to air. This barrier increases the contact resistance and, sometimes, degrades the device

performance. A high temperature anneal to form the metal-semiconductor alloy can remove this barrier. Fig. 6.7 shows the of IV characteristics of a diode before and after the anneal. A Schottky barrier at metal-germanium interface is evident as shown by the "kink" on the IV curve at V=0 (see Fig. 6.7(a)). However, after 5 minutes at 400 °C in the Argon ambient, the barrier is completely removed (Fig. 6.7(b)).

6.7. Photodiode Design

Fig. 6.8 and 6.9 show the cross section of the n^+pp^+ and induced junction germanium diodes, respectively. In the conventional n^+pp^+ photodiode, the ion implanted arsenic is used to form the shallow emitter active region. In the induced junction photodiode, the fixed positive charge in the SiO_2 induces an n-type inversion layer on the lightly-doped p-type substrate. The boron-implant p^+ channel stop prevents lateral current flow, and the p^+ layer on the back of the device forms a high-low junction. CVD SiO_2 is used for passivation and as an ion implantation mask. A three layer Ti/Pd/Ag metal is deposited, using ion mill techniques, for a low resistivity contact. The n^+ regions under the metal contacts are implanted deeply (about 1.5 μm) to prevent metal-substrate shorting.

Fig. 6.10 is the top view of the diode and various test cells used for device characterization. The area of the active region in the photodiode is 2×2 mm. All the test results of the photodiode will be shown in the next chapter.

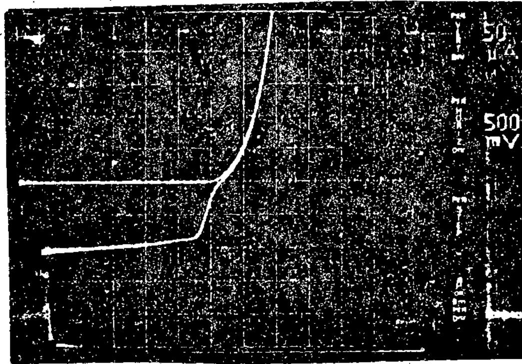

(a)

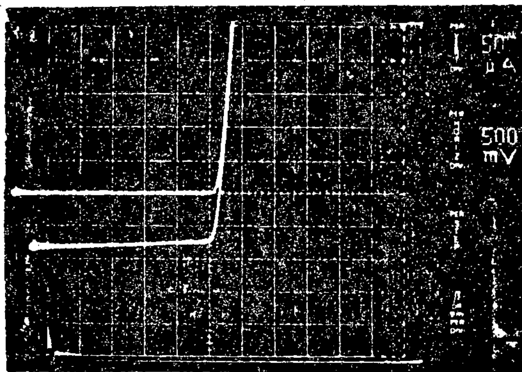

(b)

Figure 6.7 (a) Before and (b) after the 400°C post-metalization anneal.

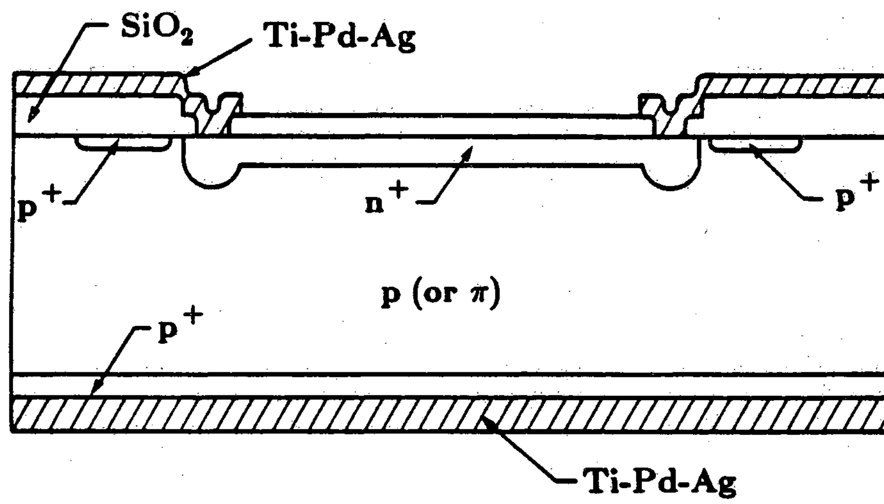

Figure 6.8 Cross section of an n^+pp^+ diode.

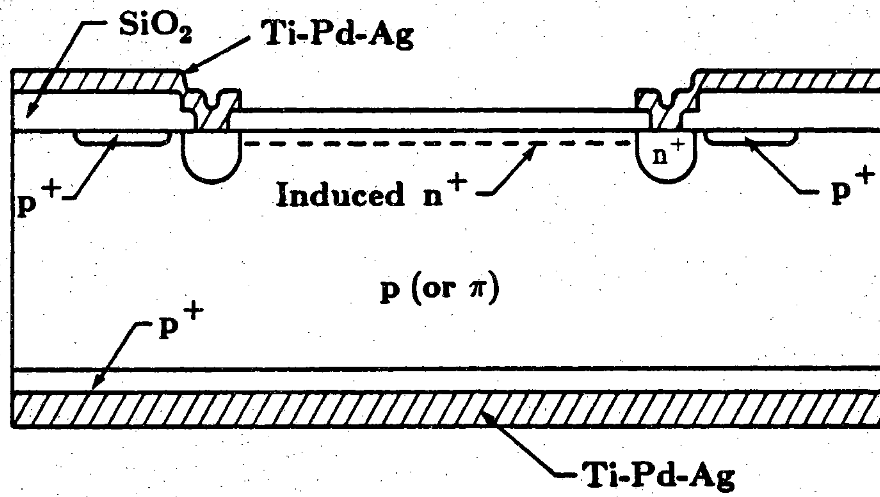

Figure 6.9 Cross section of an induced junction diode.

6.8. Test Cells

Several test devices are fabricated along with the photodiodes. Fig. 6.11 shows the top view of these devices. The MOS capacitors and the MOS transistors can be used to monitor the quality of SiO_2-Ge interfaces. The four-contact resistors are used to measure the contact resistance and resistivity of implanted impurities. The diodes of various sizes and structures are useful to the design of the cell. All the information gathered from these test devices are valuable, especially in the development of the fabrication procedures.

6.9. Summary

In this chapter, the fabrication procedures of a germanium photodiode were discussed. P-type germanium was chosen for the starting material. Silane-oxygen CVD SiO_2 was used to passivate the surface. The n^+-p junction was formed by the ion implantation, followed by the thermal annealing to activate the impurities. The metalization was accomplished by ion milling deposition and a lift-off process. Finally, a post-metalization was carried out to ensure ohmic contact. The detailed fabrication procedure is listed in the Appendix A.

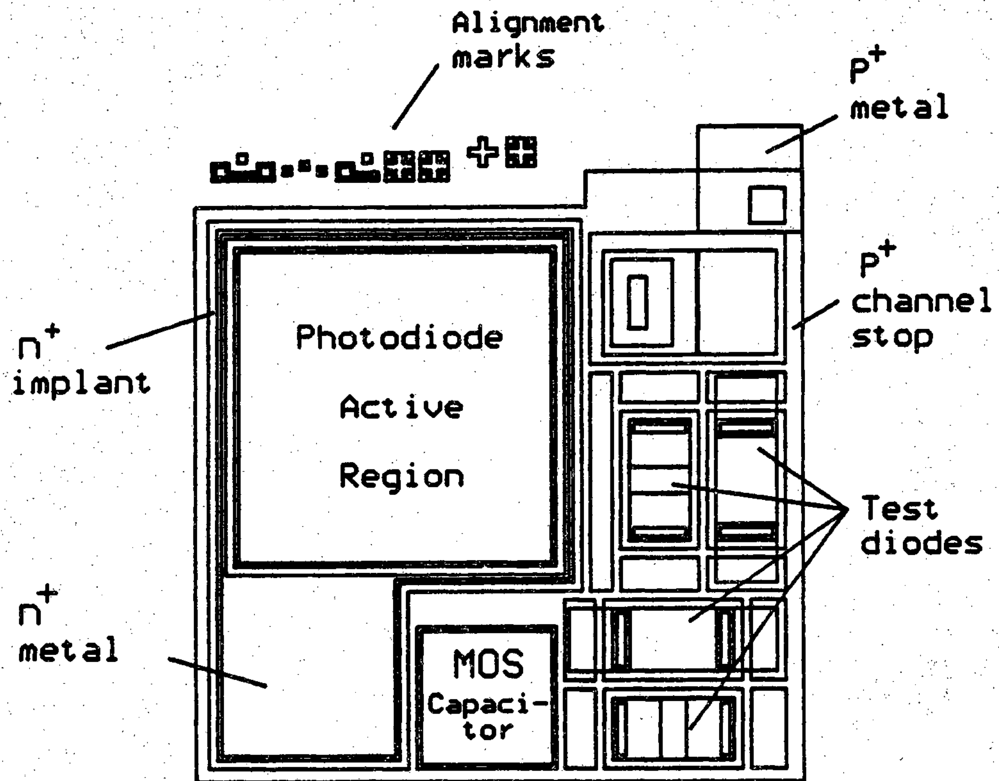

Figure 6.10 Top view of the photodiode.

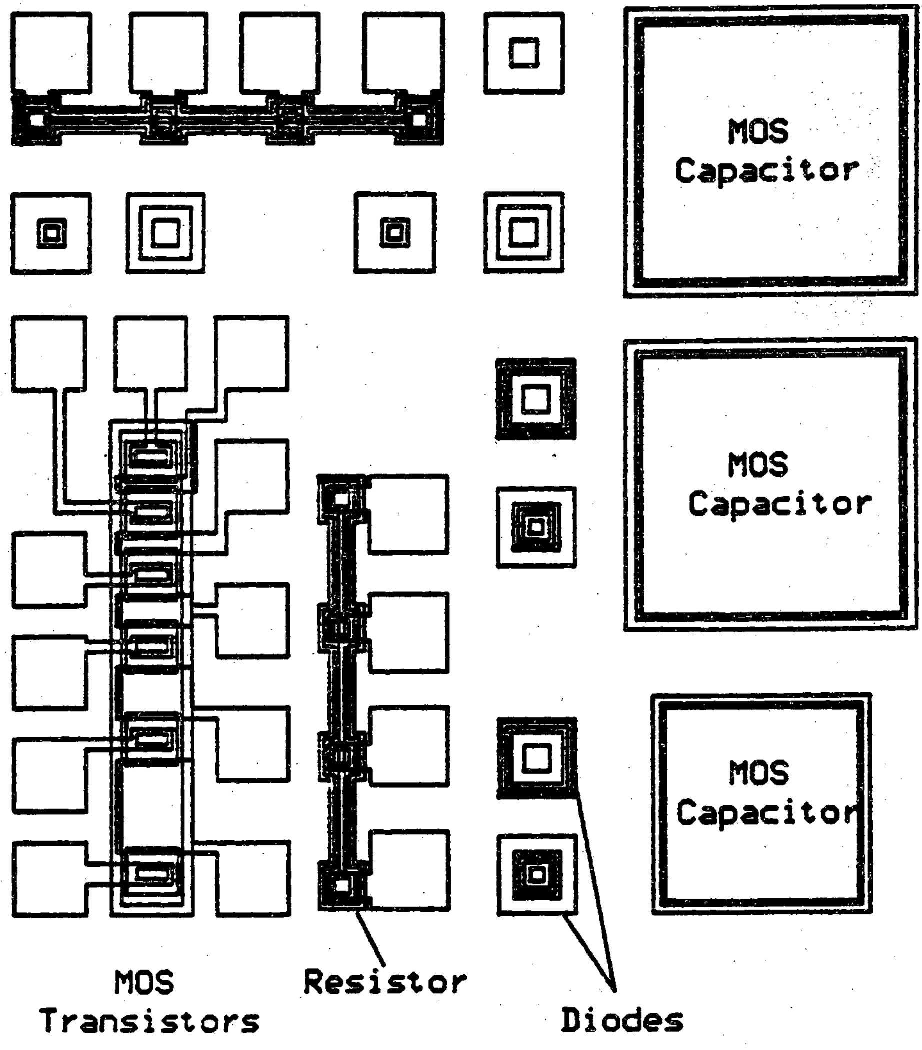

Figure 6.11 Top view of the test cells.

CHAPTER VII

MEASUREMENTS AND RESULTS

7.1. Introduction

In this chapter, the electrical and optical properties of n^+pp^+ implanted junction and induced junction diodes will be studied. The electrical tests were conducted in our lab at Purdue University, and the optical tests in the optical lab at the University of Arizona and at the National Bureau of Standards.

7.2. Electrical Measurements

The I-V characteristics were measured using a HP4151A Semiconductor Parameter Analyzer which is a fully automatic instrument designed to measure, analyze, and graphically display the DC parameters and characteristics of diodes and transistors.

7.2.1. Dark Current Measurements

The cross sections of an n^+pp^+ and an induced junction photodiode are shown in Fig. 6.9 and Fig. 6.10 respectively. The top view of the cells is shown in Fig. 6.11. The major difference between these two diodes is in the active region. For the conventional n^+pp^+ photodiode, the active region is

formed by a shallow n^+ ion implantation. In the induced junction cell, the n^+ layer in the active region is formed by surface inversion due to positive fixed charges near the SiO_2—Ge interface.

Typical dark I-V characteristics of an n^+pp^+ cell and an induced junction cell are shown in Fig. 7.1 and 7.2 respectively. These particular diodes were fabricated on a 2 Ω-cm, p-Ge wafer with (111) orientation. The fabrication procedures were described in chapter VI. the reverse current is about 18 μA and 15 μA at -5 volt for the n^+pp^+ and induced junction diode, respectively. The higher current observed in the n^+pp^+ diode can be explained as follow. There are two components in the saturation current (see Eq.(5.2)). The minority carrier currents in the base are comparable in these two diodes. This is because the inversion layer in the device forms a n^+p junction similar to that of a implanted diode. However, in the n^+pp^+ diode, the short hole diffusion length in the n^+-emitter increases the hole current and therefore, increases the total saturation current.

For a diode with step junction approximation, the dark current can be written as

$$I = I_o \left[\exp[\frac{q}{nkT}(V - IR_s) - 1] \right] \tag{7.1}$$

where n is the ideality factor and R_s is the series resistance. I_o, in the simplest case of no heavy doping effect, is given by

$$I_o = \left[\frac{qn_{io}^2 D_p}{N_D L_p} + \frac{qn_{io}^2 D_n}{N_A L_n} \right] \times (\text{area}) \tag{7.2}$$

where n_{io}, D_p, D_n, L_p, L_n, N_D, and N_A are defined in chapter four.

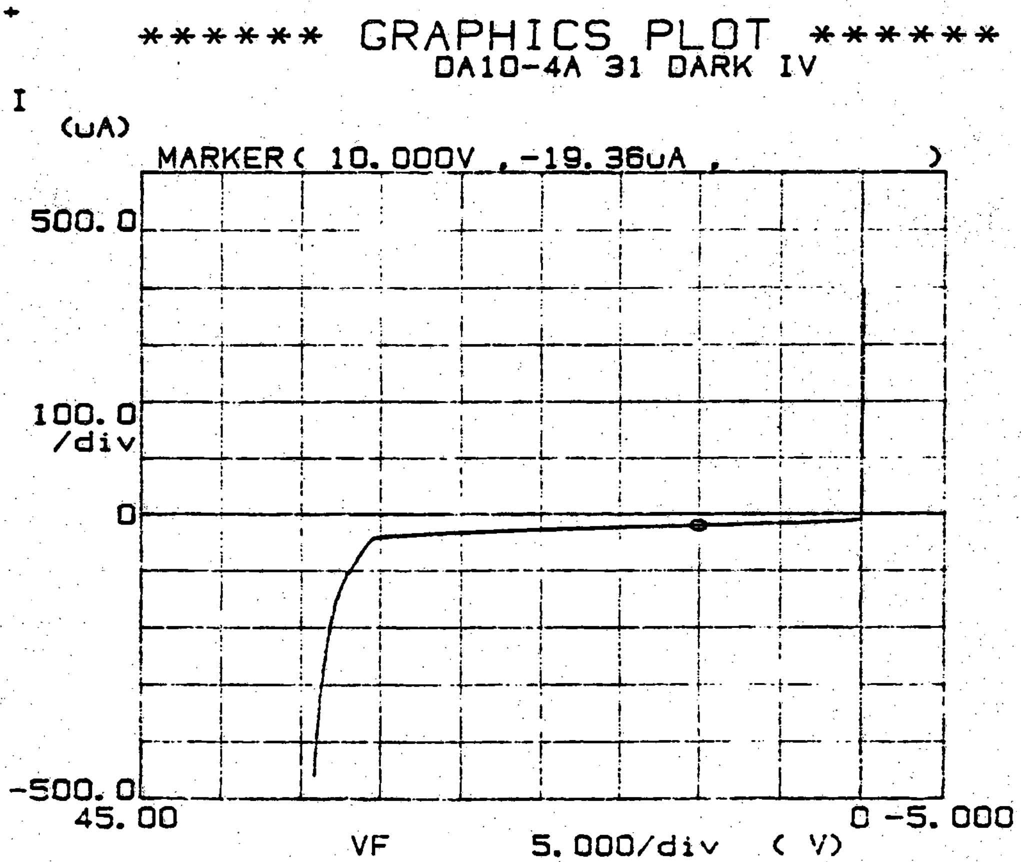

Figure 7.1 Dark I-V characteristic of an n^+pp^+ diode.

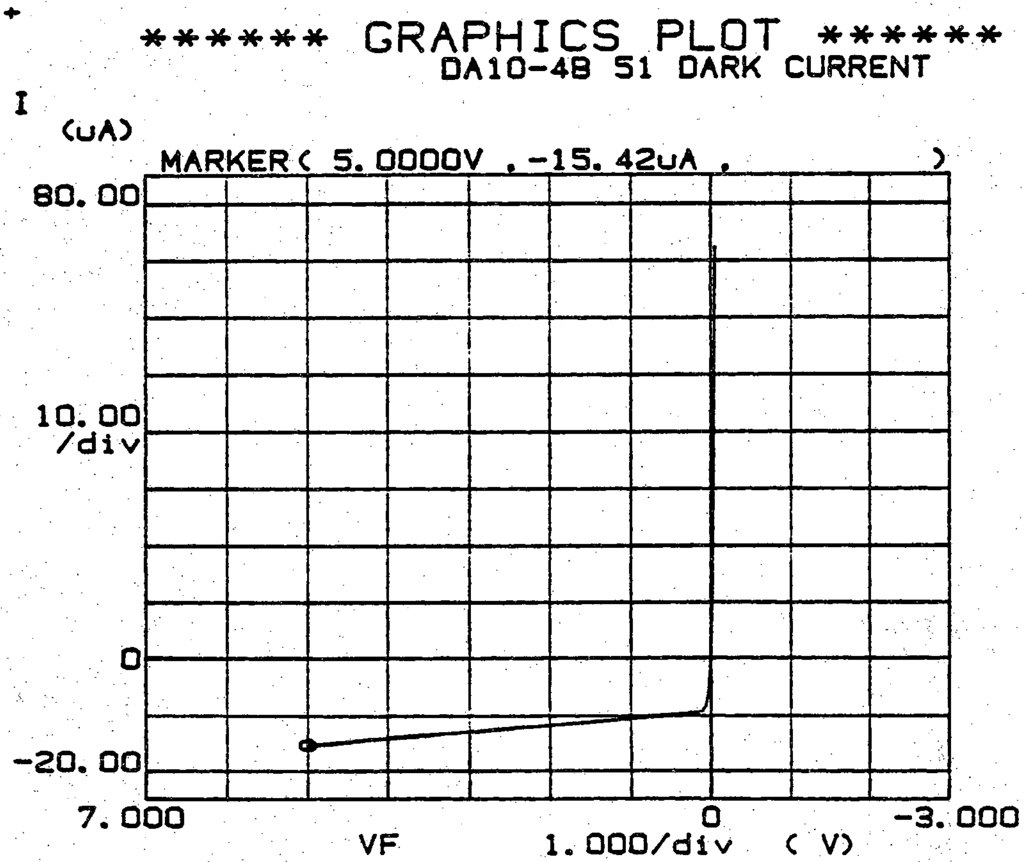

Figure 7.2 Dark I-V characteristic of an induced junction diode.

The saturation current I_o is a function of doping concentration N_A and N_D, and the minority carrier diffusion length which itself is a function of the doping concentration. Fig. 7.3 shows the saturation current distribution of 10-20 diodes from each wafer versus the substrate resistivity. The low substrate resistivity cells have low saturation current which is good for S/N ratio. However, the shorter carrier lifetime in low resistivity substrates reduced the quantum efficiency of the photodiode. It is found in our work that the photodiodes of 2 Ω-cm substrate have a moderate saturation current and by far the highest quantum efficiency. This is true in both of the n^+pp^+ and induced junction photodiodes.

7.2.2. I_{sc}-V_{oc} Measurements

The I-V characteristics for the illuminated diodes can be written as

$$I = I_L - I_o \left[\exp[\frac{q}{nkT} (V - IR_s)] - 1 \right] \quad (7.3)$$

where I_L is the light generated current. To eliminate series resistance effects, the open circuit voltage V_{oc} and short circuit current I_{sc} were measured by varying the illumination intensities. At open circuit voltage, V_{oc}, where the total current is zero, Eq.(7.3) can be written as

$$I_L \simeq I_{sc} = I_o \left[\exp(\frac{qV_{oc}}{nkT}) - 1\right] \quad (7.4)$$

In a $\log(I_{sc})$-V_{oc} plot, the intercept with the current axis gives the value of I_o, and the slope of the curve gives the ideality factor n. The ideality factor n of 1.05 for n^+pp^+ diode, and 1.1 for induced junction diode are shown in Fig. 7.4 and 7.5. They are very close to the ideal case of 1.0.

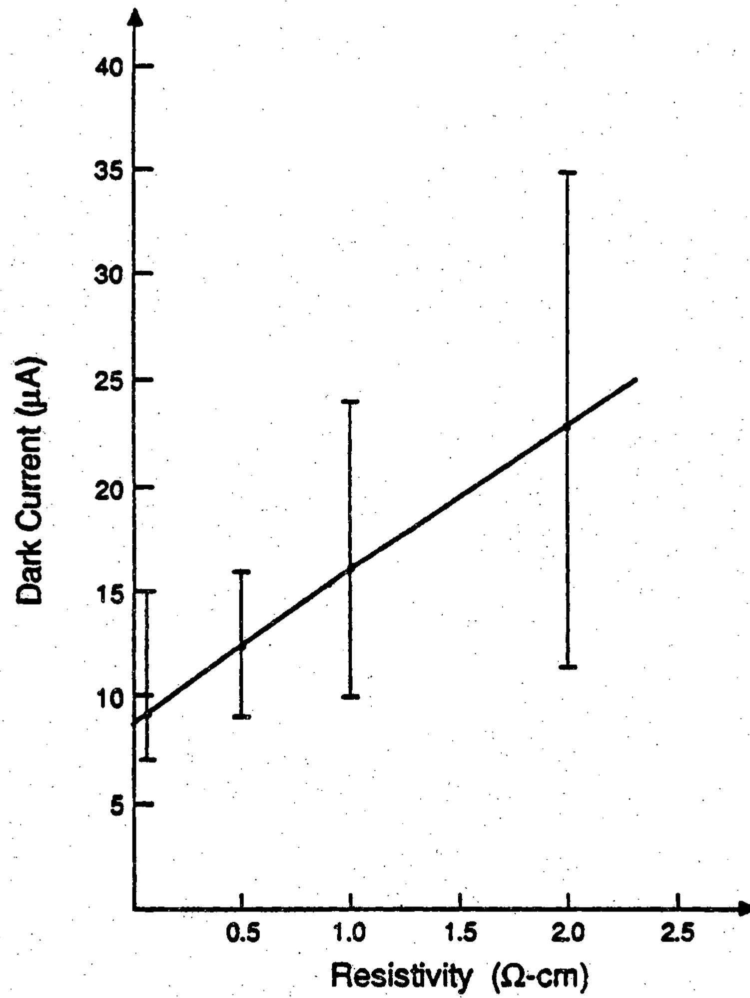

Figure 7.3 Saturation currents of n^+pp^+ photodiodes as a function of substrate resistivity.

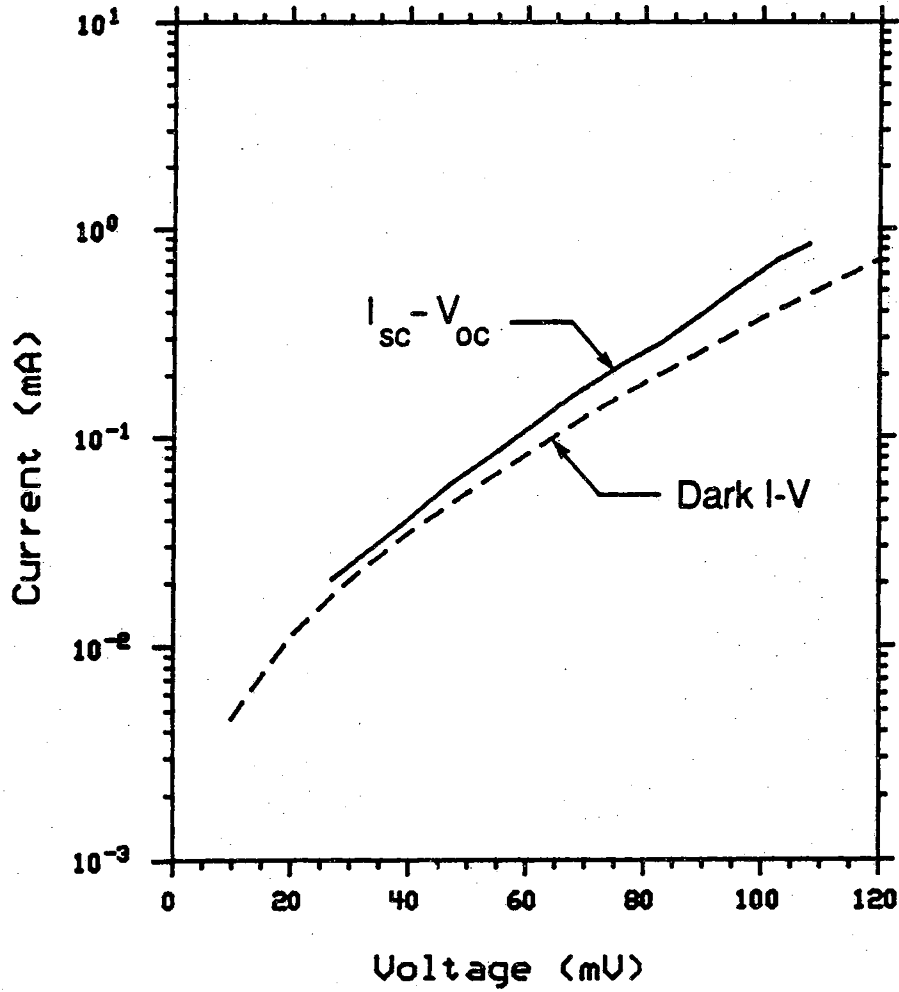

Figure 7.4 $I_{sc}-V_{oc}$ and forward current of an n^+pp^+ diode.

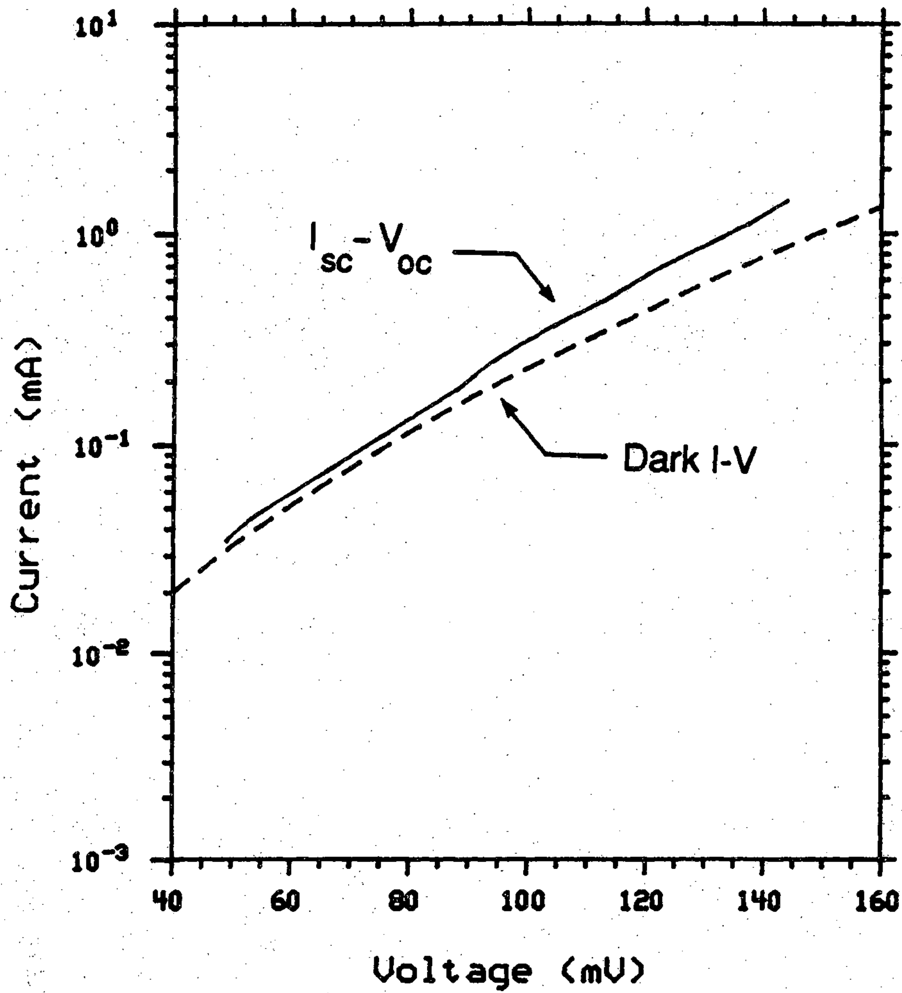

Figure 7.5 I_{sc}–V_{oc} and forward current of an induced junction diode.

7.2.3. Series Resistance R_s Measurements

The series resistance of a photodiode can arise from the resistance of the base region, the sheet resistance of the thin emitter, and the front and back contact resistance. The base and emitter resistance can be estimated by a four-point probe measurement. This technique is also used to monitor the post-implant anneal.

The metal-semiconductor contact resistance can be estimated by a four-terminal test resistor shown in Fig. 7.6. The four contacts are equally separated by a distance l. R_l, the resistance between two contacts, and R_c, the contact resistance at the contact window, can be measured by forcing a known current between two contacts and measuring the voltage between these contacts. If R_1 is measured by forcing a current between contact 1 and 4, and R_2 is measured in a similar fashion using contact 2 and 3, R_l and R_c can be determined by

$$R_l = \frac{1}{2}(R_1 - R_2) \tag{7.5}$$

and

$$R_c = \frac{1}{4}(3R_2 - R_1) \tag{7.6}$$

The typical contact resistivity of the Ag/Pd/Ti-Ge system is $3.6\times10^{-4}\ \Omega\text{—cm}^2$. This contact resistivity contributes less than 1 Ω to the total series resistance of the Ge photodiodes fabricated in this study.

Fig. 7.4 and 7.5 shows the effect of series resistance on the I-V characteristics. As shown in Fig. 7.4 and 7.5, the forward I-V characteristics are displaced from the $I_{sc}-V_{oc}$ curve indicating the presence of a high series

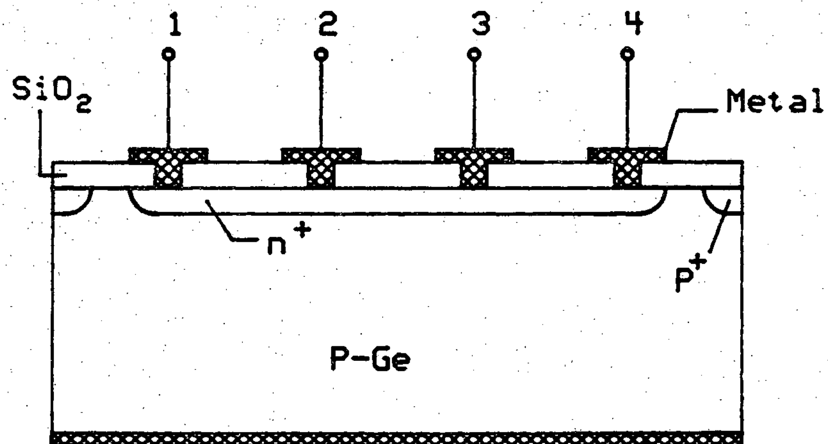

Figure 7.6 Cross section of a four-terminal resistor for contact resistance measurements.

resistance in the cell. The high R_s is a result of the shallow n^+ emitter. The R_s shown in the figures is 15 Ω for the n^+pp^+ diode and 15.5 Ω for the induced junction diode. High series resistance may cause significant resistive voltage drop under high intensity illumination. This voltage drop has little effect on the n^+pp^+ diodes. However, for the induced junction diode, the voltage drop on the surface forward biases the inversion layer and, therefore, reduces the quantum efficiency. We will demonstrate this effect by using a computer simulation in the next chapter.

7.2.4. CV Measurements

The C-V measurements were made on the MOS capacitors fabricated along with the induced junction cells (see Fig. 6.11). The high frequency CV measurement is shown in Fig. 7.7. This capacitor was fabricated on a germanium substrate with a background concentration of $10^{16}/cm^3$. The thickness of the SiO_2 layer is 2830 Å and the area of the capacitor is 5.625×10^{-2} cm^2. The dashed line in Fig. 7.7 represents the theoretical curve obtained for this MOS capacitor [57]. The curve is shifted to the left along the voltage axis to match the experiment value at flat-band. This CV measurement shows that the surface is inverted at zero gate voltage and the threshold voltage is about -35 volts. The Q_f/q is estimated to be around $3.77\times10^{11}/cm^2$, assuming all the shifting is caused by the fixed charges in the SiO_2.

The stretchout in the measured CV curve indicates the presence of a large surface state density. As mentioned before, these states act as the carrier recombination centers and affect the ideal characteristics of the devices.

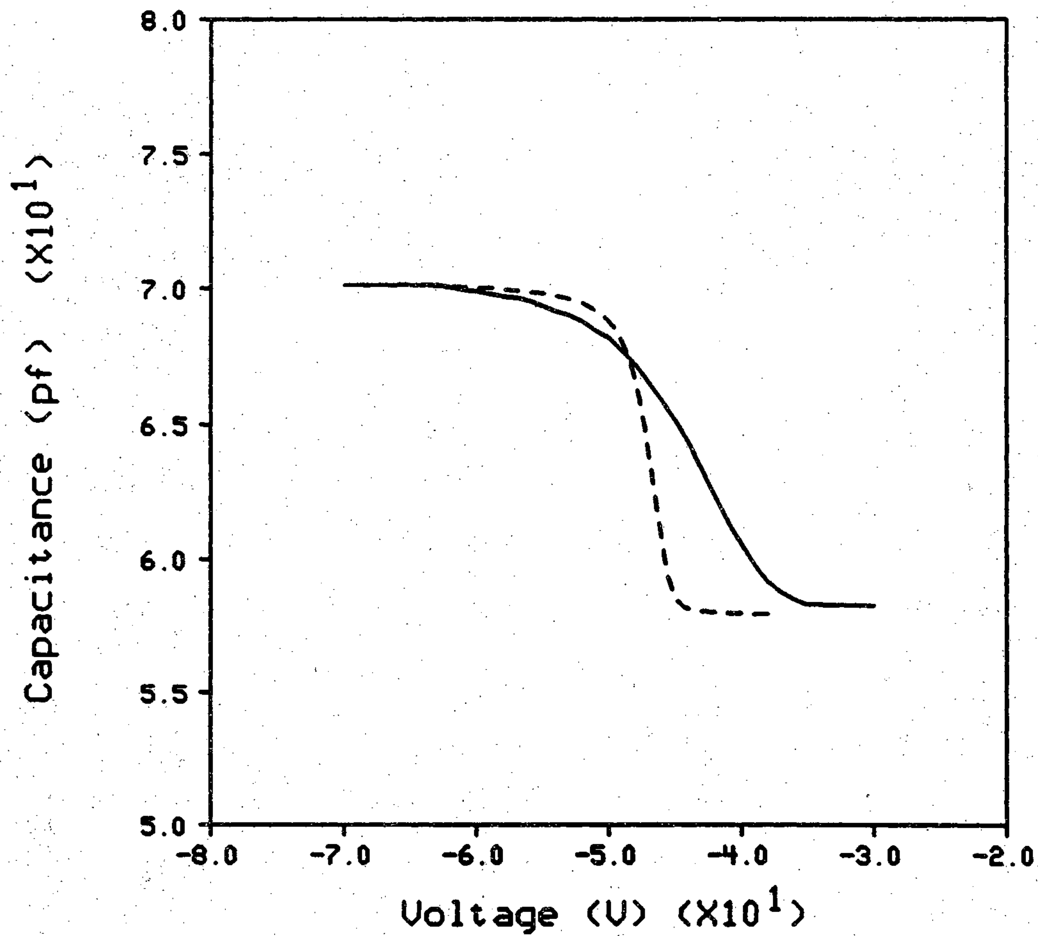

Figure 7.7 The measured high frequency MOS CV characteristic (solid line). The device was fabricated on a $N_A = 1\times10^{16}/cm^3$ germanium substrate with an oxide thickness of 2830 Å and an area of 5.625×10^{-3} cm^2. The dashed line is the ideal CV curve and is shifted to the left along the voltage axis by 48.5 volts.

7.2.5. MOS Transistor Measurements

The IV characteristics of a MOS transistor also reveal evidence of the surface inversion. Fig. 7.8(a) is the top view of test transistors with a gate width of 200 μm and gate length of 20, 40, 80, 160, and 320 μm, respectively. Fig. 7.8(b) shows the IV characteristic of a MOS transistor with 160 μm gate length fabricated on a 40 Ω-cm Ge-substrate. At zero gate voltage, the transistor was turned on by the fixed charges in the SiO_2, and turned off by a gate voltage of -10 volts. The 1 mA current at V_g=-10 V is the leakage current from drain and source of the transistor.

7.3. Optical Measurements

The primary objective of this work is to design and fabricate a self-calibrating radiometer operated over the 0.7 to 1.5 μm wavelength range. The quantum efficiency is the single most important characteristic of a self-calibrating radiometric diode.. This application requires the quantum efficiency of the photodiode be within a few percent of unity.

The optical measurements were conducted at University of Arizona by Mike Nofsiger. The measurements include the power of the light source P_{opt} with radiation frequency ν, the reflectance r(λ), and the light generated current I_L. The internal quantum efficiency $\eta(\lambda)$ can be calculated by the following expression,

$$\eta(\lambda) = \frac{I_L/q}{[P_{opt}/h\nu]\,[1 - r(\lambda)]} \tag{7.7}$$

The effective reflectance r(λ) can be reduced to near zero by the set-up shown in Fig. 1.2. Therefore, to increase I_L, or to reduce the carrier losses in

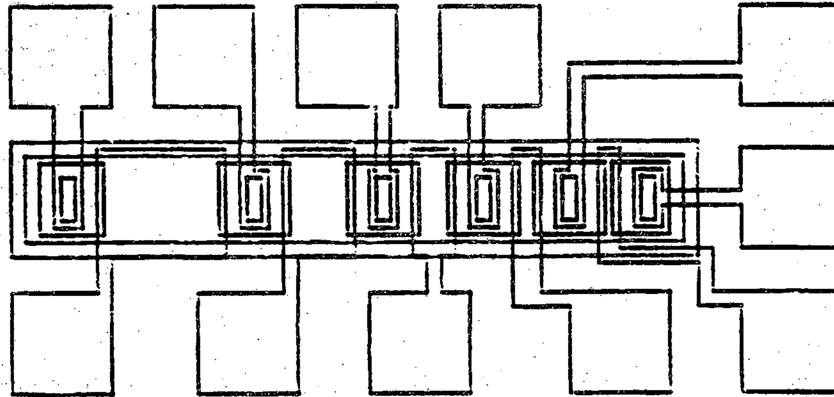

(a)

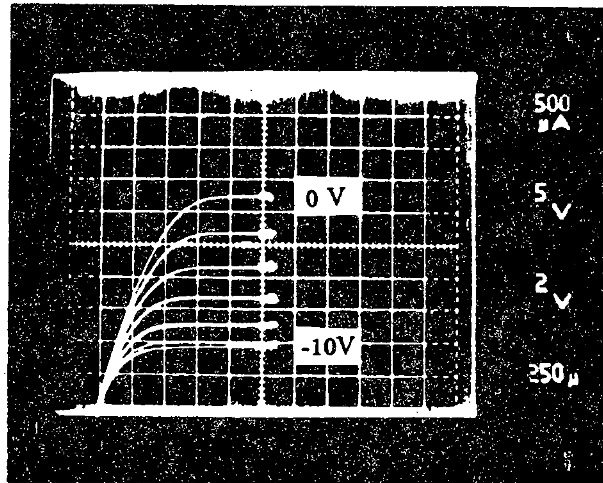

(b)

Figure 7.8 (a) Top view of the test MOS transistors; (b) the I-V characteristics of a MOS transistor.

the cells is the major concern in order to maximize $\eta(\lambda)$.

The measured internal quantum efficiency for both n^+pp^+ and induced junction cells are shown in Fig. 7.9. The emitter of the n^+pp^+ photodiode was formed by an As implant with a doping density of $10^{14}/cm^2$ and an energy of 30 Kev on a 2 Ω-cm substrate. The estimated junction depth in the active region is around 0.35 μm. In the n^+pp^+ cell, the rapid fall of $\eta(\lambda)$ at short wavelengths is due to carrier losses at the front surface and in the emitter region. The presence of high concentrations of interstitial donors in the emitter region increases the probability of the electron-hole recombination and, therefore, reduces the minority carrier lifetime, τ_p. In addition, the surface states at the $SiO_2 - Ge$ interface are electron-hole recombination centers. The surface recombination mechanism can be characterized by the surface recombination velocity, S_p. A relatively large S_p and short carrier lifetime have been found in the Ge photodiodes. The typical values for τ_p in the emitter and S_p at the surface are 10^{-8} sec and 10^5 cm/sec, respectively. We will discuss this in detail in chapter VIII.

In the induced junction diode, the internal quantum efficiency is less sensitive to the carrier lifetime and surface recombination velocity. This is especially true for the short wavelength radiation with which the electron-hole pairs are generated near the surface. The high quantum efficiency in induced junction diodes can be attributed to the following:

(1) Since ion-implantation induced damage is not present in the induced junction diode, the emitter lifetime should be higher than that of the n^+pp^+ diodes.

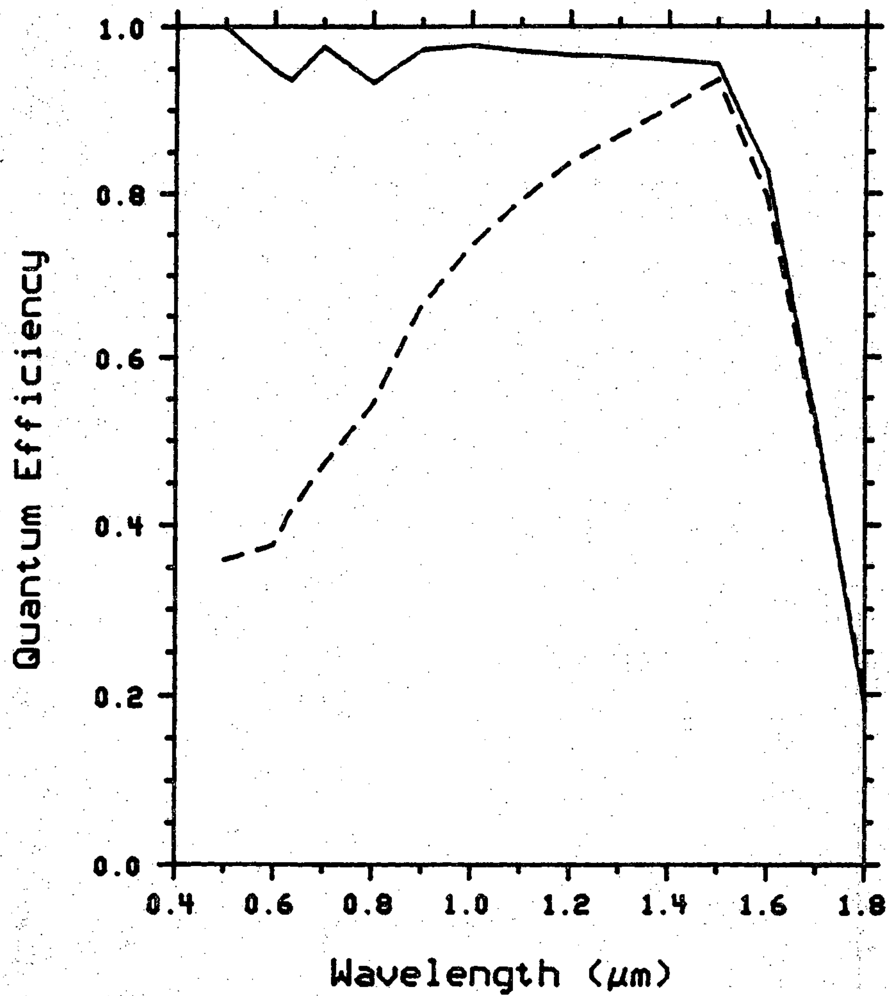

Figure 7.9 Internal quantum efficiency of an n^+pp^+ photodiode (dashed line) and an induced junction photodiode (solid line).

(2) The fixed positive charges in the SiO_2 invert the surface of the p-substrate. An electric field is induced near the surface due to the energy band bending. This surface field helps to separate the photon-generated carriers and increases the collection efficiency.

The quantum efficiency is a function of the substrate resistivity as well. Generally speaking, the higher the substrate resistivity, the higher the quantum efficiency will be. This is because of the longer carrier lifetime of the high base resistivity material, which corresponds to a low background impurity concentration. There is another advantage to using a high resistivity substrate for the induced junction diodes. The lightly doped substrate can easily be inverted to form a n^+ layer at the surface. However, as has been shown in Fig. 7.3, the saturation current increases as the base resistivity increases. A trade-off has to be made if an optimal photodiode is to be designed.

Fig. 7.10 and 7.11 show the measured quantum efficiency for the n^+pp^+ and induced junction photodiodes with different base resistivities, respectively. In Fig. 7.10, the quantum efficiencies of two n^+pp^+ photodiodes are plotted. The dashed line is the cell with substrate resistivity of 0.1Ω-cm. Its emitter was formed by an As implant with a doping density of $10^{14}/cm^2$ and an energy of 45 Kev. For the solid line cell, the emitter was implanted using the same impurity and density but using an energy of 30 Kev on a 2 Ω-cm substrate. Higher quantum efficiency in the solid line cell is found at short wavelengths due to the shallow emitter junction depth, and at long wavelengths due to the longer minority carrier lifetime in the base.

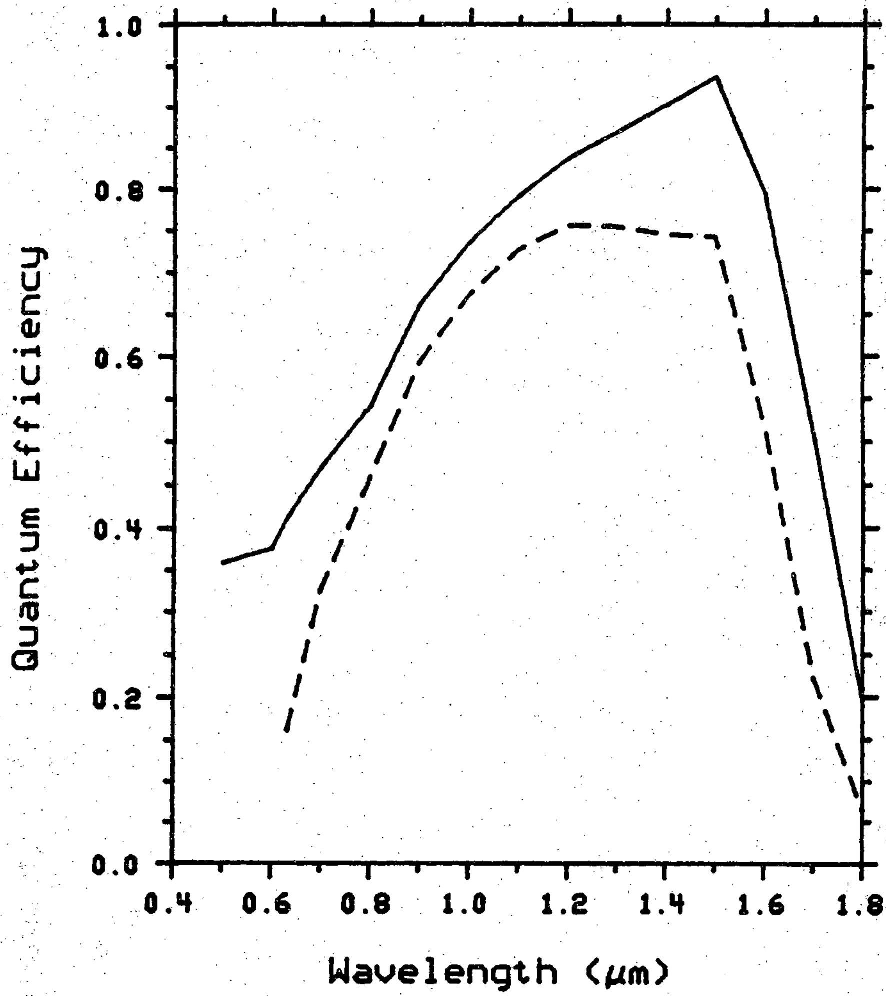

Figure 7.10 Internal quantum efficiency of two n^+pp^+ photodiodes with substrate resistivity of 0.1 Ω-cm (dashed line) and 2 Ω-cm (solid line).

In induced junction diodes, the substrate resistivity also affects the quantum efficiency. In Fig. 7.11, two diodes with the same structure but different substrate resistivities are compared. The quantum efficiencies are virtually independent of the wavelength over 0.7 to 1.5 μm range. However, at wavelengths greater than 1.5 μm, the quantum efficiency is noticeably larger in the higher resistivity substrate.

Emitter junction depth x_j in the n^+pp^+ diodes also plays an important role in affecting the quantum efficiency. Fig. 7.12 shows the quantum efficiency of two n^+pp^+ diodes with the same substrate but different x_j, The emitter of the dashed line cell was formed by multiple arsenic implantation with dosage/energy of 1.5×10^{15} cm^{-2}/25Kev, 1.7×10^{15} cm^{-2}/60Kev and 4×10^{15} cm^{-2}/140Kev. The estimated junction depth is around 1.7 μm. The estimated junction depth of the solid line cell is about 1.2 μm which was formed by an 5×10^{15} cm^{-2}/70Kev implantation. The shallower emitter diode leads to a higher quantum efficiency, as we have discussed in chapter V.

7.4. Summary

It has been demonstrated that the induced junction photodiode with natural inversion layer performs significantly better than the n^+pp^+ photodiode, especially in the short wavelength range. The induced junction implies a high electric field at the surface and in the depletion region. This field aids the collection of photon-generated carriers, especially of those generated near the Ge surface. All these features demonstrate that the induced junction photodiodes are suitable for the use as a absolute self-calibrating radiometer over 0.7 to 1.5 μm wavelength range.

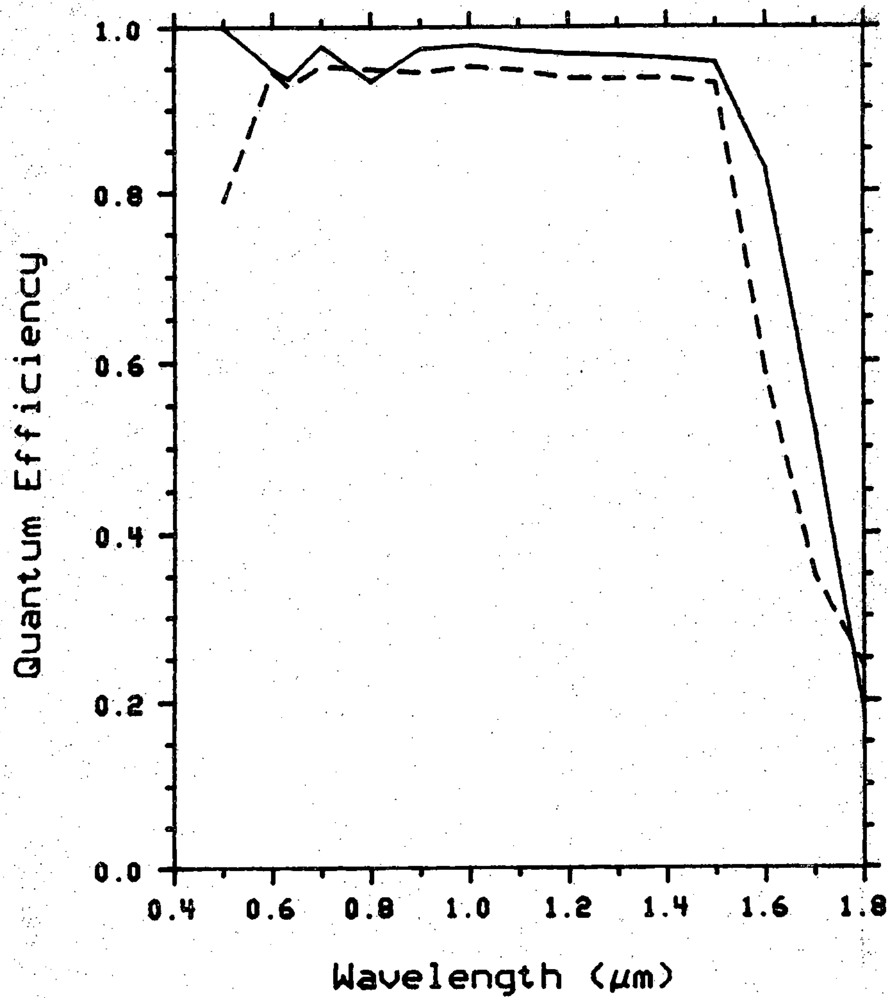

Figure 7.11 Internal quantum efficiency of two induced junction photodiodes with substrate resistivity of 0.5 Ω-cm (dashed line) and 2 Ω-cm (solid line).

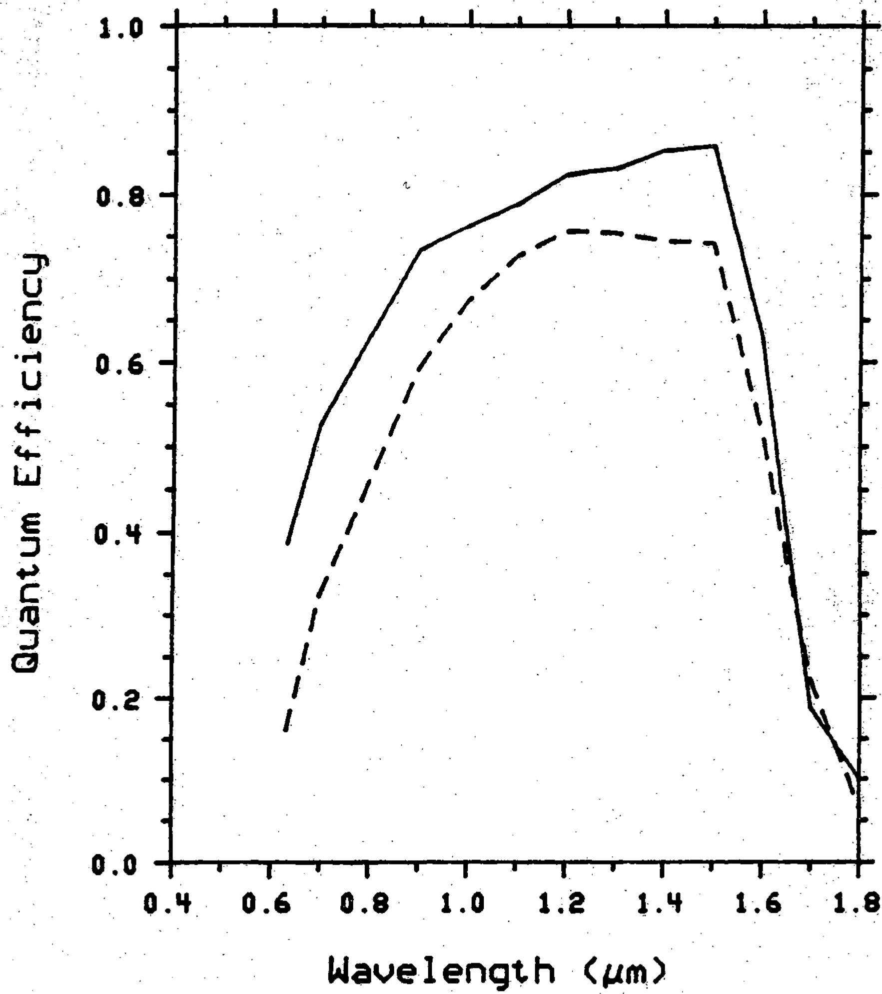

Figure 7.12 Internal quantum efficiency of two n^+pp^+ photodiodes with estimated emitter junction depth of 1.2 μm (solid line) and 1.7 μm (dashed line).

CHAPTER VIII
NUMERICAL ANALYSIS

8.1. Introduction

In deriving an analytical solution for a p-n junction photodiode quantum efficiency, assumptions are needed to obtain a closed-form solution to the differential equations which have been presented in chapter IV. Since the internal quantum efficiency depends on many parameters in a complicated fashion, a computer simulation is absolutely necessary for the accurate description of a photodiode. In this chapter, we will discuss two device simulation programs, SCAP1D (**S**olar **C**ell **A**analysis **P**rogram in **One** **D**imension) and SCAP2D (**S**olar **C**ell **A**nalysis **P**rogram in **Two** **D**imension), which were developed by Lundstrom and Gray of Purdue University, respectively [62,63].

SCAP1D was originally developed to analyze conventional n^+pp^+ (or p^+nn^+) solar cells. This code has been very successful used for studying and predicting the performance of a solar cell operating at low intensity. However, for two-dimensional devices such as IBC (Integrated Back Contact) and point contact solar cells, SCAP2D has to be used to accurately analyze the devices.

8.2. Program Description and Modifications

Since the codes were designed for Si solar cells, they have to be modified for use in modeling germanium photodiodes. In the following sections, a brief description of the modifications will be presented, followed by a comparison of the computed values and the experimental results. We will demonstrate that the modified SCAP1D is adequate for the n^+pp^+ and induced junction photodiodes operated at the low level illumination. However, for high intensity illumination, the surface potential in the induced junction diode will be affected by the lateral flow of the photo-generated current in the inversion layer. In that case, SCAP2D has to be used to analyze this problem.

8.2.1. General Description

The simulation programs simultaneously solve the Poisson's equation

$$\nabla^2 V = \frac{q}{\epsilon_s \epsilon_o} (n - p + N_A^- - N_D^+) \tag{8.1}$$

and the hole and electron continuity equations

$$\nabla \cdot \mathbf{J}_p = q\,(G - R) \tag{8.2}$$

and

$$\nabla \cdot \mathbf{J}_n = -\,q\,(G - R) \tag{8.3}$$

where $\mathbf{J}_p$ and $\mathbf{J}_n$ are the current density for the hole and electron, respectively. $\mathbf{J}_p$ and $\mathbf{J}_n$ can be written, in one dimension with consideration of the heavy doping effects [62], as

$$J_p = -\,pq\mu_p \frac{d}{dx}\,[V - (\gamma - 1)\frac{\Delta_G}{q}] - kT\mu_p \frac{dp}{dx} \tag{8.4}$$

and

$$J_n = -\,nq\mu_n\,[\frac{d}{dx}\,(V - \gamma\,\frac{\Delta_G}{q})] + kT\mu_n \frac{dn}{dx} \tag{8.5}$$

where γ is an effective asymmetry factor and Δ_G is the effective bandgap shrinkage. γ and Δ_G include the effects of bandgap narrowing and position dependent density of states.

8.2.2. Recombination

The net recombination rate R in Eq.(8.2) and (8.3) can be written as

$$R = (np - n_{ie}^2)\left[\, A_n n + A_p p + \frac{1}{\tau_{no}(p + p_1) + \tau_{po}(n + n_1)} \right] \tag{8.6}$$

This expression is obtained under the assumptions of Boltzmann statistics and a single level Schockley-Read-Hall recombination center. The quantities p_1 and n_1 are defined in terms of the trap level E_T as

$$p_1 = n_{ie}\, e^{(E_i - E_T)/kT} \tag{8.7}$$

and

$$n_1 = n_{ie}\, e^{(E_T - E_i)/kT} \tag{8.8}$$

where n_{ie} is the effective intrinsic concentration including the heavy doping effects of bandgap narrowing and position-dependent density of states. n_{ie} can be written as

$$n_{ie}^2 = n_{io}^2\, e^{\Delta_G/kT} \tag{8.9}$$

where n_{io} is the intrinsic concentration of lightly doped germanium.

The Auger recombination is also included in Eq.(8.6) and is characterized by the constants A_n and A_p. This recombination has a significant influence on high level injection characteristics, where excess carrier densities may be very large.

8.2.3. Generation

The optical generation, G, in Eq.(8.2) and (8.3) is a function of the incident flux Φ_o and the surface reflectance r. With the assumption of unity quantum yield, the generation rate at position x can be written as

$$G(x) = (1 - r)\, \Phi_o\, \alpha(\lambda)\, e^{-\alpha(\lambda)x} \tag{8.10}$$

where $\alpha(\lambda)$ is the absorption coefficient at wavelength λ. The theoretical calculation of α will be discussed in the following section.

8.2.4. Bandgap and Intrinsic Carrier Concentration

The bandgap of germanium changes with variations in the pressure, temperature, and doping concentration. At one atmosphere pressure, the high purity germanium temperature-dependent bandgap is given by the empirical formula of Thurmond [64] as

$$E_g(T) = E_g(0) - \frac{\beta T^2}{T + \varsigma} \tag{8.11}$$

where $\beta = 4.774\times10^{-4}/^{o}K$ and $\varsigma = 235\ ^{o}K$.

Bandgap narrowing in Ge is calculated using Mahan's model [65]. Mahan made a comprehensive calculation of the energy gap in germanium as a function of the concentration of donor impurities. His theoretical expression for the bandgap shrinkage in germanium is

$$\Delta E_g(\text{meV}) = 6.63\times(n/10^{18})^{2/3} - 4.89\times(n/10^{18})^{1/3}$$

$$- 8.2\times(n/10^{18})^{1/4} - 3.0 \qquad (8.12)$$

where n is the electron carrier concentration in the conduction band. This calculation is in good agreement with experimental data [66].

The intrinsic concentration in lightly doped germanium is given by the expression

$$n_{io} = \sqrt{N_C N_V}\, e^{-E_g/2kT}$$

$$= 4.9\times10^{15} \left(\frac{m_{de}m_{dh}}{m_o}\right)^{3/4} T^{3/2}\, e^{-E_g/2kT} \qquad (8.13)$$

where N_C and N_V are the effective density of states in the conduction and valence bands, respectively, m_{de} and m_{dh} are the density-of-state effective mass for electrons and holes, respectively and m_o is the electron rest mass. n_{io} at room temperature is $2.4\times10^{13}/cm^3$ for germanium. The intrinsic carrier concentration, including bandgap shrinkage effects, is expressed by Eq.(8.9).

8.2.5. Mobility and Diffusion Coefficient

The doping-dependent carrier mobility in Ge is approximated by the Caughey-Thomas expression [67]

$$\mu_n = \frac{\mu_{n,max} - \mu_{n,min}}{1 + \left(\dfrac{N}{N_{ref,n}}\right)^{\beta_n}} + \mu_{n,min} \qquad (8.14)$$

and

$$\mu_p = \frac{\mu_{p,max} - \mu_{p,min}}{1 + \left(\frac{N}{N_{ref,p}}\right)^{\beta_p}} + \mu_{p,min} \tag{8.15}$$

where μ's are the electron and hole mobilities and N is the doping concentration. The parameters β_n, β_p and N_{ref}'s are determined by computer fitting to experiment measurements. Table 8.1 lists the parameter values which result in a best fit to the measured results.

The mobility also varies with electric field and free carrier concentration. The dependence on the electric field is neglected because no strong electric field occur in the photodiode under normal operation conditions, , except in the space charge region. Carrier-carrier scattering is also neglected. This effect can be important under very high intensity illuminations [68].

The carrier diffusion coefficient (D_n for electrons and D_p for holes) is another important parameter. In thermal equilibrium, the relationship between D_n and μ_n (or D_p and μ_p) is given by [33]

$$D_n = 2\left(\frac{kT}{q}\mu_n\right)\frac{F_{1/2}\left(\frac{E_f - E_c}{kT}\right)}{F_{-1/2}\left(\frac{E_f - E_c}{kT}\right)} \tag{8.16}$$

where $F_{1/2}$ and $F_{-1/2}$ are Fermi-Dirac integrals. For a nondegenerate semiconductor, where n is much smaller than N_C (and $p \ll N_V$), Eq.(8.16) can be reduced to

Table 8.1 Mobility in germanium.

Electron		Hole	
$\mu_{n,max}$	5000 $cm^2/V-sec$	$\mu_{p,max}$	1980 $cm^2/V-sec$
$\mu_{n,min}$	10 $cm^2/V-sec$	$\mu_{p,min}$	24 $cm^2/V-sec$
β_n	0.42	β_p	0.467
$N_{ref,n}$	$2.76\times10^{16}/cm^3$	$N_{ref,p}$	$1.37\times10^{17}/cm^3$

$$D_n = \frac{kT}{q} \mu_n \tag{8.17}$$

and similarly,

$$D_p = \frac{kT}{q} \mu_p \tag{8.18}$$

which is better known as the Einstein relationship. In the computer codes, Eq.(8.17) and (8.18) are used for the D_n and D_p.

8.2.6. Optical Properties

The reflectance, r, of the Ge surface, the shadowing factor of metal contact grids, the intensity of incident flux, Φ_o, and the absorption coefficient, $\alpha(\lambda)$, are the quantities that have to be known to calculate the optical generation rate, $G(\lambda)$. In the simulation codes, the value of reflectance, shadowing factors, and incident flux are given in the input data card.

The absorption coefficient, α, of Ge is evaluated by an empirical formula. α is a function of temperature and the wavelength of the radiation and can be written as

$$\alpha(\lambda,T) = \alpha_D(\lambda,T) + \alpha_I(\lambda,T) \tag{8.19}$$

where $\alpha_D(\lambda,T)$ and $\alpha_I(\lambda,T)$ are the absorption of direct and indirect energy band transitions respectively. For a parabolic band approximation, with E_{gd} as the direct band gap energy, α_D can be written as [33]

$$\alpha_D = A_d[\hbar\omega - E_{gd}(T)]^{1/2} \tag{8.20}$$

where A_d is the proportionality constant. The energy band gap is a function

of temperature and can be expressed as Eq.(8.11). The same value of β and ς is assumed for all values of the Ge bandgap.

α_I is the absorption of indirect energy band transitions. This absorption process involves either a phonon absorption or a phonon emission to conserve the electron momentum. For a parabolic energy band approximation, α_I can be written as [69]

$$\alpha_I = \sum_{i,j} C_i A_j(T) \left[\frac{(\hbar\omega - E_{gj}(T) + E_{pi})^2}{\exp(E_{pi}/kT) - 1} + \frac{(\hbar\omega - E_{gj}(T) - E_{pi})^2}{1 - \exp(-E_{pi}/kT)} \right] \tag{8.21}$$

where suffix i refers to various possible phonons of energy E_p and the suffix j refers to the indirect band E_g. For simplicity, we only consider the Γ_8^v–L_6^c and Γ_8^v–X_5^c indirect transition [29] and the phonon energy of transverse acoustic (TA) and transverse optical (TO) mode. The final form of the absorption coefficient α is the summation of Eq.(8.20) and (8.21)

$$\alpha = \sum_{\substack{i=1,2 \\ j=1,2}} C_i A_j(T) \left[\frac{(\hbar\omega - E_{gj}(T) + E_{pi})^2}{\exp(E_{pi}/kT) - 1} + \frac{(\hbar\omega - E_{gj}j(T) - E_{pi})^2}{1 - \exp(-E_{pi}/kT)} \right]$$

$$+ A_d[\hbar\omega - E_{gd}(T)]^{1/2} \tag{8.22}$$

where $E_{gd}(T)$ and $E_{gj}(T)$'s are evaluated by Eq.(8.11). The value of all the parameters in Eq.(8.22) are listed in the Table 8.2.

Free electrons and holes can make a transition from one level to another in the conduction band and valence band by absorbing a photon. This process is referred as the free carrier absorption, and can only become

Table 8.2 Coefficient constants in Eq.(8.22)

Quantity	Value
$E_{gd}(0)$	0.86 eV
$E_{g1}(0)$	0.74 eV
$E_{g2}(0)$	0.95 eV
C_1	5.5
C_2	4.0
A_1	80 $cm^{-1}eV^{-2}$
A_2	1200 $cm^{-1}eV^{-2}$
E_{p1}	7.755×10^{-3} eV
E_p	2.757×10^{-2} eV

significant in the long wavelength region in the heavily doped material [35]. Since free carrier absorption is very small in the wavelength region of 0.7 to 1.5 μm, this absorption process is negligible.

8.2.7. Minority Carrier Lifetime and Surface Recombination Velocity

Minority carrier lifetime and surface recombination velocity are important parameters in the semiconductor. Assuming the Schockley-Read-Hall (SRH) model with single recombination level in the energy bandgap, the carrier lifetime can be written as

$$\tau = \frac{1}{\sigma v_{th} N_{TT}} \tag{8.23}$$

where σ is the cross section of the traps, v_{th} is the thermal velocity of the carriers, and N_{TT} is the trap density. Similarly, with the same model, the surface recombination velocity S can be written as

$$S = \sigma_s v_{th} N_{ss} \tag{8.24}$$

where σ_s is the cross section of the surface states, and N_{ss} is density of states effective for recombination. Since these two parameters are sensitive to the fabrication processes and difficult to measure, the values of τ and S for electron and hole are obtained by matching the theoretical calculation and experiment results of the dark currents, $I_{sc}-V_{oc}$ measurements, and quantum efficiency measurements.

The minority carrier lifetime is a function of doping concentration [70]. The doping-dependent lifetime is expressed by the Kendal equation as

$$\tau = \frac{\tau_o}{1 + \frac{N}{N_{ref}}} \tag{8.25}$$

where τ_o is the carrier lifetime in a lightly doped semiconductor, N is the total impurity doping concentration, and N_{ref} is a reference concentration. Since τ and S are difficult to measure, their values are given as device parameters. The experimental value of τ_o in Ge ranges from 0.2 μs to 1000 μs [71,72]. In the computer simulation codes, we have set τ_o to 5 μs which is reasonable in view of our experiment results.

8.2.8. Normalizations and Boundary Conditions [62,63]

The computer programs solve simultaneously Poisson's equation, the current equations and the continuity equations, with given boundary conditions. For the convenience of numerical calculation, Eqs.(8.1-10) can be simplified using the normalization factors listed in Table 8.3. With some mathematical manipulation, we can rewrite Poisson's equation as

$$\nabla^2 V = n - p + N_A^- - N_D^+ \tag{8.26}$$

and the hole and electron continuity equations as

$$\nabla \cdot \mathbf{J}_p = G - R \tag{8.27}$$

and

$$\nabla \cdot \mathbf{J}_n = -(G - R) \tag{8.28}$$

the hole and electron current equations as

Table 8.3 Normalization factors [62]

Variable	Normalization Factor
Position	$L_{Di} = \left[\frac{\epsilon_s kT}{q^2 n_{io}}\right]^{1/2}$
Electrostatic Potential	$V_{nor} = \frac{kT}{q}$
Electric Field	$\frac{V_{nor}}{L_{Di}}$
Carrier Concentration	n_{io}
Current Densities	$\frac{qD_o n_{io}}{L_{Di}}$
Generation-Recombination Rate	$\frac{D_o n_{io}}{L_{Di}^2}$
Carrier Lifetimes	$\frac{L_{Di}^2}{D_o}$
Carrier Mobilities	$\frac{D_o}{V_{nor}}$
Carrier Diffusion Coefficients	$D_o = 1\ \text{cm}^2/\text{sec}$
Surface Recombination Velocity	$\frac{L_{Di}}{D_o}$
Fixed Surface-Charge Density	$L_{Di} n_{io}$
Surface Recombination Velocity	$\frac{D_o}{L_{Di}}$

$$J_p = -\mu_p \left[p \frac{d}{dx} [V - (\gamma - 1)V_G] - \frac{dp}{dx}\right] \tag{8.29}$$

and

$$J_n = -\mu_n \left[n \frac{d}{dx} (V - \gamma V_G) + \frac{dn}{dx}\right] \tag{8.30}$$

where $V_G = \dfrac{\Delta_G}{V_{nor}}$, and the recombination rate R as

$$R = (np - e^{V_G}) \left[A_n n + A_p p + \frac{1}{\tau_{no}(p + p_1) + \tau_{po}(n + n_1)} \right] \tag{8.31}$$

where

$$p_1 = e^{(E_i - E_T)/kT} \, e^{V_G} \tag{8.32}$$

and

$$n_1 = e^{(E_T - E_i)/kT} \, e^{V_G} \tag{8.33}$$

In order to solve three nonlinear second order partial differential equations, six boundary conditions are required. The boundary conditions can be the values of V, p, and n, or their derivatives at the boundary. The boundary conditions for V are obtained by first solving Poisson's equation under the equilibrium conditions with the assumption of charge neutrality at the boundary, that is to solve

$$\frac{d^2 V_{eq}}{dx^2} = e^{(V_{eq} + \gamma V_G)} \tag{8.34}$$

The potentials at boundary are

$$V(x{=}0) = V_{eq}(x{=}0) \tag{8.35}$$

and

$$V(x{=}H) = V_{eq}(x{=}H) + V_{bias} \tag{8.36}$$

where H is the thickness of the device and V_{bias} is the normalized bias voltage.

The electron and hole concentrations at the surfaces vary with surface conditions. If ohmic boundary conditions are specified, the carriers are assumed to be equal to their equilibrium values

$$p = p_{eq} = e^{-[V_{eq} + (\gamma-1)V_G]} \tag{8.37}$$

and

$$n = n_{eq} = e^{(V_{eq} + \gamma V_G)} \tag{8.38}$$

If non-ohmic boundary is specified, the surface recombination velocity, S, is used to characterize the boundary condition. The current densities at the surface are

$$\mathbf{J}_p \cdot \hat{\mathbf{n}} = R_s \tag{8.39}$$

and

$$\mathbf{J}_n \cdot \hat{\mathbf{n}} = -R_s \tag{8.40}$$

where

$$R_s = \frac{pn - e^{V_G}}{\frac{1}{S_n}(p+p_{1s}) + \frac{1}{S_p}(n+n_{1s})} \tag{8.41}$$

Under the low injection conditions, Eq.(8.39) and (8.40) can be reduced to

$$J_n = S_n\,(n - n_{eq}) \tag{8.42}$$

for p-type material and

$$J_p = S_p\,(p - p_{eq}) \tag{8.43}$$

for n-type material.

For the induced junction photodiode, the fixed charge density N_f has to be considered in the boundary conditions. By Gauss's law, the displacement field is discontinuous by a amount of the surface charge density, ρ_s, across the non-ohmic boundary as

$$(\mathbf{D}_{Ge} - \mathbf{D}_{ext})\cdot\hat{\mathbf{n}} = \rho_s \tag{8.44}$$

or

$$\nabla V_{Ge}\cdot\hat{\mathbf{n}} = -\frac{\mathbf{D}_{ext}\cdot\hat{\mathbf{n}} + \rho_s}{\epsilon_s} \tag{8.45}$$

where $\mathbf{D}_{Ge} = \epsilon_s\,\mathbf{E}_{Ge} = -\nabla V_{Ge}$. In normalized form, Eq.(8.45) becomes

$$\nabla V_{Ge}\cdot\hat{\mathbf{n}} = -N_f \tag{8.46}$$

where N_f is the normalized effective surface charge density.

8.2.9. Numerical Techniques

Finite difference techniques are used in SCAP1D and SCAP2D [62,63]. The codes simultaneously solve Poisson's equation, and the electron and hole continuity equations. There are three unknowns, V, p and n, at each mesh point in the device. The mesh points are generated automatically by the simulation programs or are specified by the user. For a device with N mesh points, we have to solve 3N coupled nonlinear differential equations simultaneously for the complete solutions.

Newton's method was chosen for this work because of its simplicity and effectiveness. If **F** represents the 3N independent equations in a N mesh point cell, **u** is the vector of V, p, and n, and **J** is the Jacobian matrix of **F**, then the problem is reduced to solving the following linear system

$$[\mathbf{J}(\mathbf{u}^k)]\ \Delta\mathbf{u}^{k+1} = -\ \mathbf{F}(\mathbf{u}^k) \tag{8.47}$$

where k is the kth iterative solution of Eq.(8.47), $\mathbf{J} = \left[\dfrac{\partial \mathbf{F}(\mathbf{u}^k)}{\partial \mathbf{u}^k}\right]$ and $\Delta\mathbf{u}^{k+1} = \mathbf{u}^{k+1} - \mathbf{u}^k$. The over relaxation damping technique was also applied in SCAP1D and SCAP2D calculations to improved the convergence characteristics of the codes. Newton's method requires an initial guess to start the iterative process. The equilibrium solution of Poisson's equation of Eq.(8.34) is used for the initial guess. The complete operation of the simulation programs is summarized by the flowchart shown in Fig. 8.1.

8.3. Simulations

In this section, modified SCAP1D and SCAP2D were used to analyze the Ge photodiode. A set of device parameters was found by fitting the theoretical values to the experimental data of the n^+pp^+ and induced junction diodes. With this set of parameters established, we can look further at the physical behavior inside the device which otherwise couldn't be observed.

Table 8.4 shows the parameters used to model the n^+pp^+ cell (DA10-4A #31) and induced junction cell (DA10-4B #51). A step p-n junction was assumed for simplicity (see Fig. 6.4 and 6.5 for the measured deep and shallow n^+ doping profiles). A relatively large surface recombination velocity

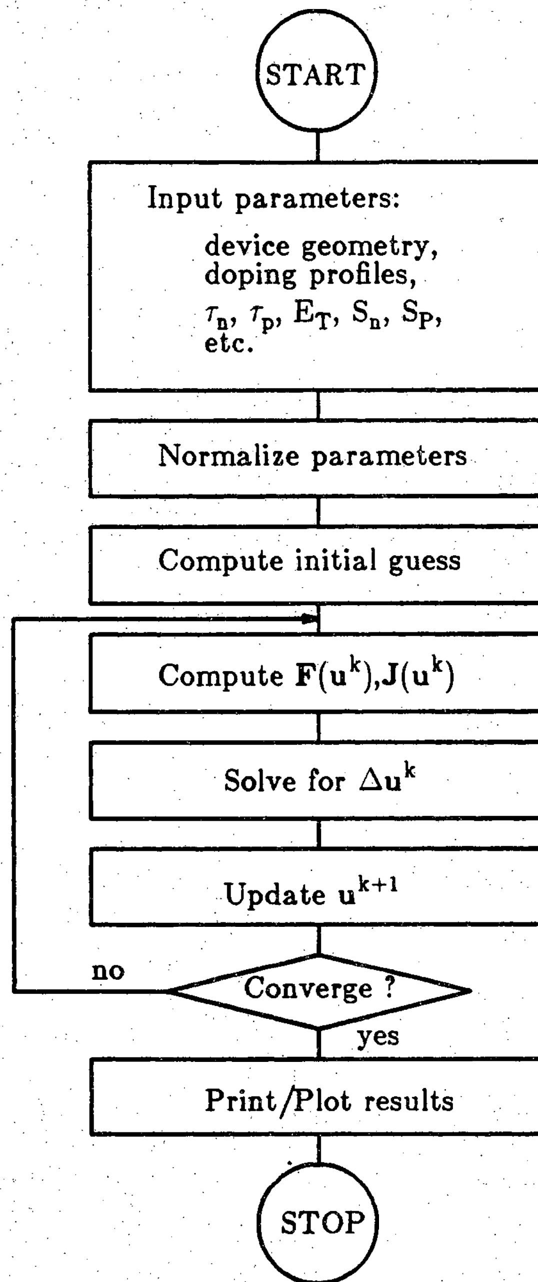

Figure 8.1 Flowchart of SCAP1D and SCAP2D operation.

Table 8.4 Device parameters for simulation

Variable	Value
Bias voltage	0 volt
Base	p-Ge, 2 Ω—cm
Thickness	300 μm
Doping concentration	$1.66 \times 10^{15}/cm^3$
Emitter	
Junction	Step
Junction depth (deep)	1.5 μm
Junction depth (shallow)	0.35 μm
Doping concentration	$2 \times 10^{19}/cm^3$
Carrier lifetime for electron, τ_{no}	5 μ sec
Carrier lifetime for hole, τ_{po}	5 μ sec
Surface recombination velocity	8×10^5 cm/sec
Fixed charges Q_f/q	5×10^{12} /cm^2
Illumination intensity	100 μA/cm^2
Kendal reference concentration	$5 \times 10^{16}/cm^3$

($S_p = 8\times10^5$ cm/sec) at the SiO_2-Ge surface and low minority carrier lifetimes ($\tau_o = 5\mu$ sec) in the bulk have to be assumed for good fitting. This simulation also assumes that the devices were operated at short circuit conditions. The structure of the devices were described in chapter V and their electrical and optical measurement in chapter VII.

Fig. 8.2-5 shows the comparison between computer calculations and experimental data for dark I-V and quantum efficiency. The figures show good agreement between theory and experiment. They also show good agreement between SCAP1D and SCAP2D codes. Therefore, SCAP1D will be used for device analysis under low injection conditions. For high intensity illumination, SCAP2D will be used for two-dimensional analysis.

Fig. 8.2 and 8.3 shows the simulation of forward currents of a n^+pp^+ diode and an induced junction diode, respectively. In the simulation, the calculated forward-biased currents were obtained by setting the series resistance to zero. The calculated values show good agreement with the I_{sc}–V_{oc} measurements where effects of the series resistance are eliminated.

The quantum efficiency calculation has also shown good agreement with experiment. In Fig. 8.4, the low quantum efficiency in the n^+pp^+ diode at short wavelengths is attributed to the high surface recombination velocity and low effective minority carrier lifetime in emitter ($\tau \cong 10^{-9}$ sec). In addition, the Auger recombination effect becomes significant in the emitter and, thus, further reduces the carrier lifetimes. In the induced junction cell, the quantum efficiency is less sensitive to carrier lifetime and surface recombination velocity (see Fig. 8.5).

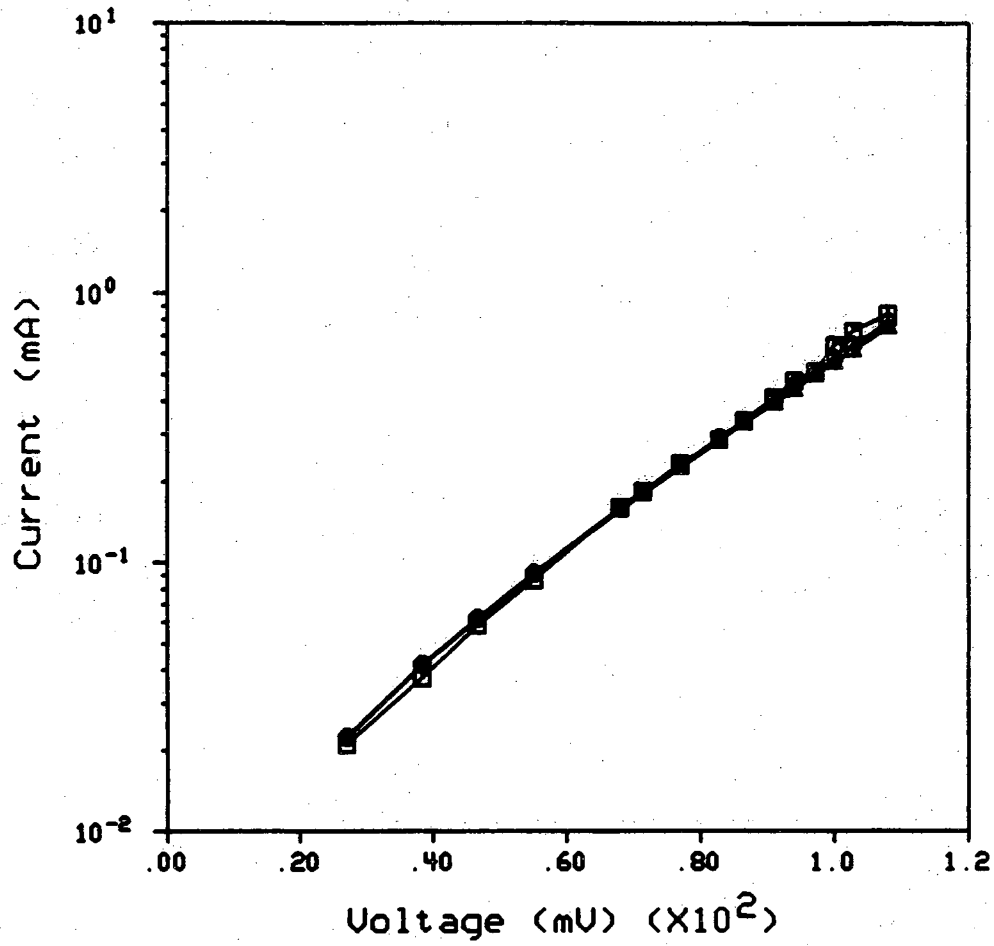

Figure 8.2 Measured (□), SCAP1D simulated (○), and SCAP2D simulated (△) $I_{sc} - V_{oc}$ of a $n^{+}pp^{+}$ photodiode.

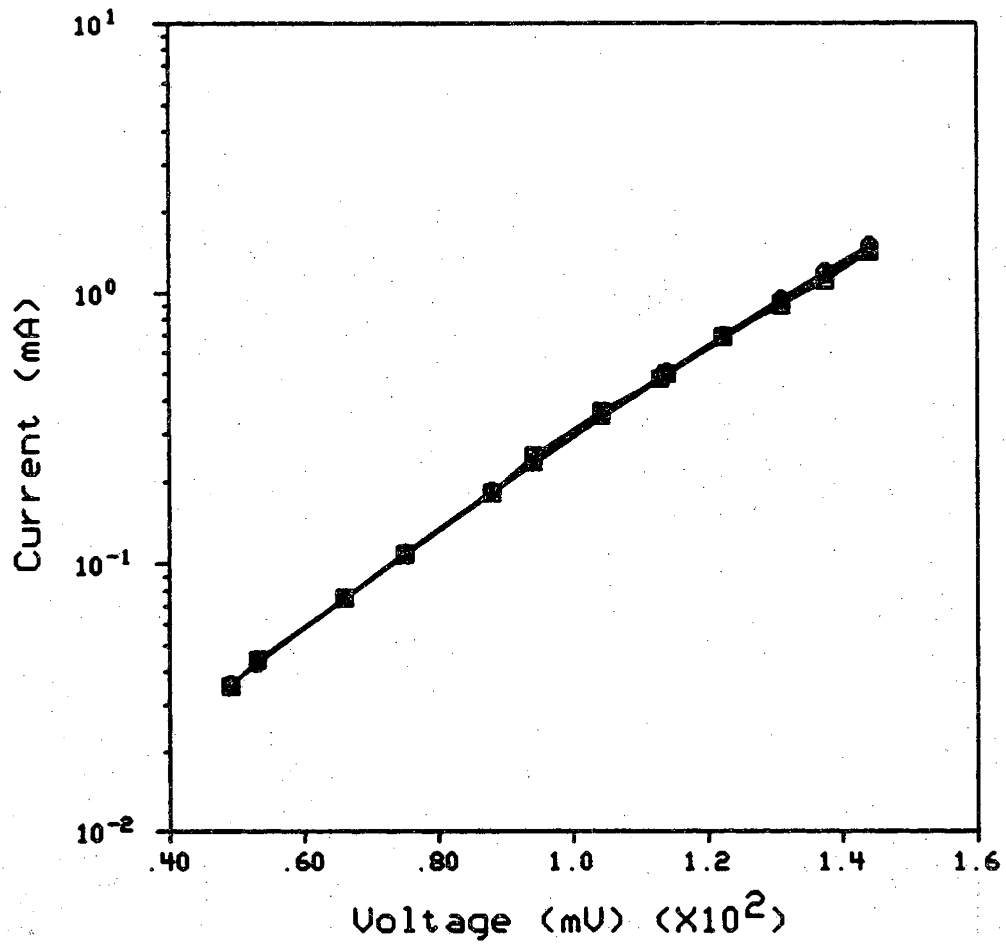

Figure 8.3 Measured (□), SCAP1D simulated (○), and SCAP2D simulated (△) $I_{sc} - V_{oc}$ of an induced junction photodiode.

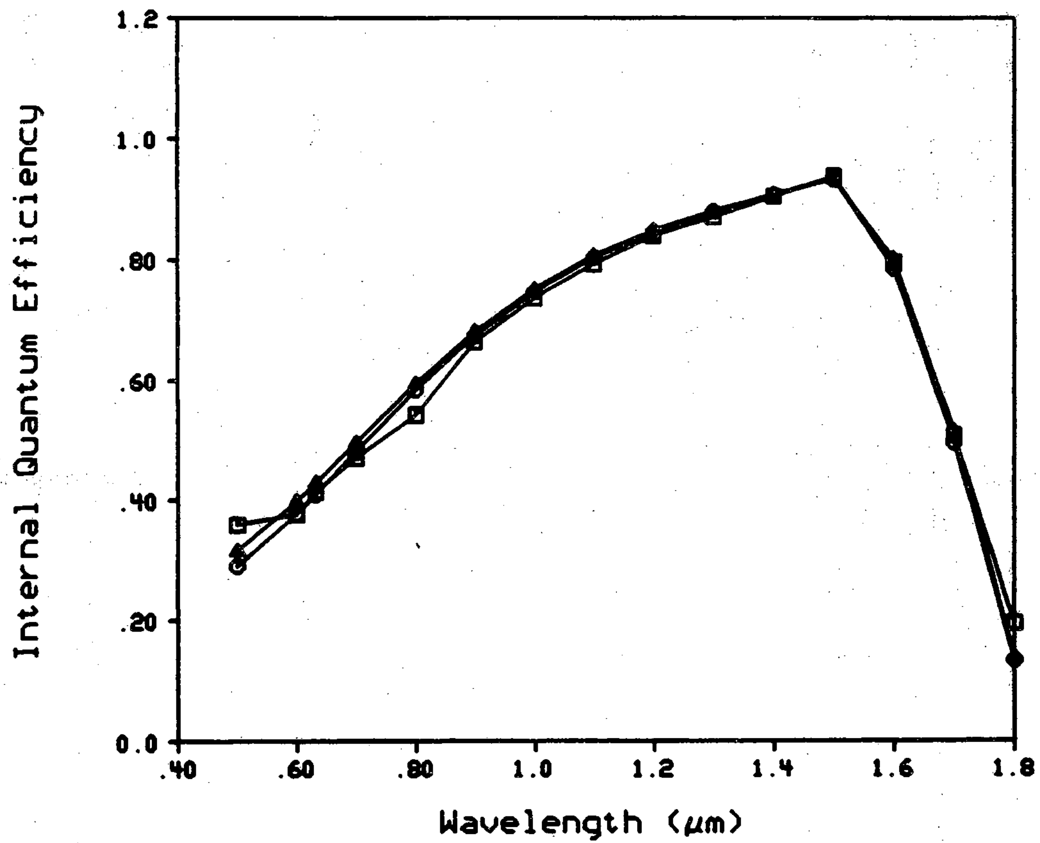

Figure 8.4 Measured (□), SCAP1D simulated (○), and SCAP2D simulated (△) internal quantum efficiency of a $n^{+}pp^{+}$ photodiode.

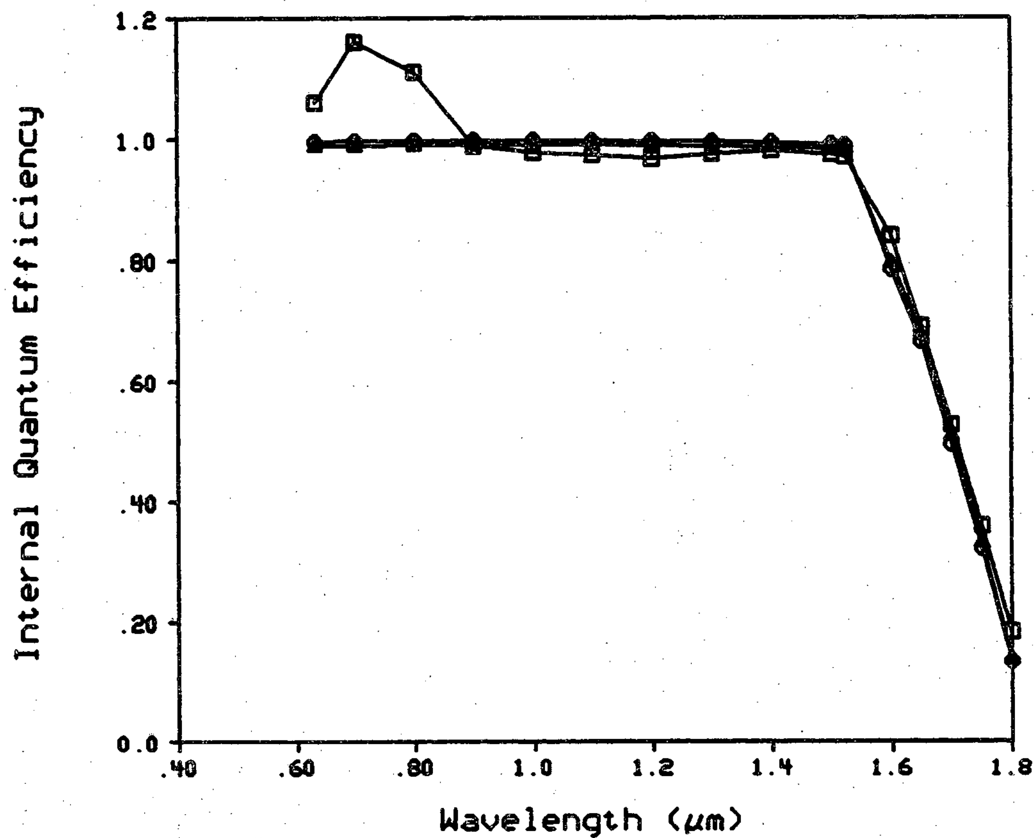

Figure 8.5 Measured (□), SCAP1D simulated (○), and SCAP2D simulated (△) internal quantum efficiency of an induced junction photodiode.

Fig. 8.6 shows the model of the doping profile of the n^+pp^+ diode. We have assumed constant doping for the emitter. Fig. 8.7 shows the doping-dependent carrier mobility in this device model. The solid line in the figure is the mobility for holes and the dashed line that for electrons.

Fig. 8.8-9 shows the carrier generation rate in germanium. The solid line is the generation rate for monochromatic light as a function of position. The dashed line is the integrated generation. We have assumed that one absorbed photon generates one electron-hole pair. As shown in the figure, the Ge absorbed 99.9% of the short wavelength radiation (0.9 μm) within 1 μm of depth. For longer wavelength radiation (1.5 μm), 99.9% of the photons are absorbed in 20 μm of penetration (Fig. 8.9).

Fig. 8.10-11 are the energy band diagrams, when the diode is illumination and biased at zero volts, of the n^+pp^+ and induced junction diode respectively. These plots show the conduction band edge, the valence band edge, the center of the gap, and the quasi-fermi levels for electrons and holes, all as a function of position. Fig. 8.11 shows the energy band bending near the surface of an induced junction cell due to the fixed positive charges in the SiO_2 ($Q_f/q = 5\times10^{12}$ /cm^2). The energy band bending converts the surface to a shallow n^+ layer thus forming a p-n junction near the surface.

Fig. 8.12-13 show the potential as the function of position in the vicinity of junction. Since the radiometer is operated under zero bias, this is the potential under short circuit current condition. The dashed lines in the figures are the potentials under the equilibrium condition. The deviation between the curves increases under high intensity illumination.

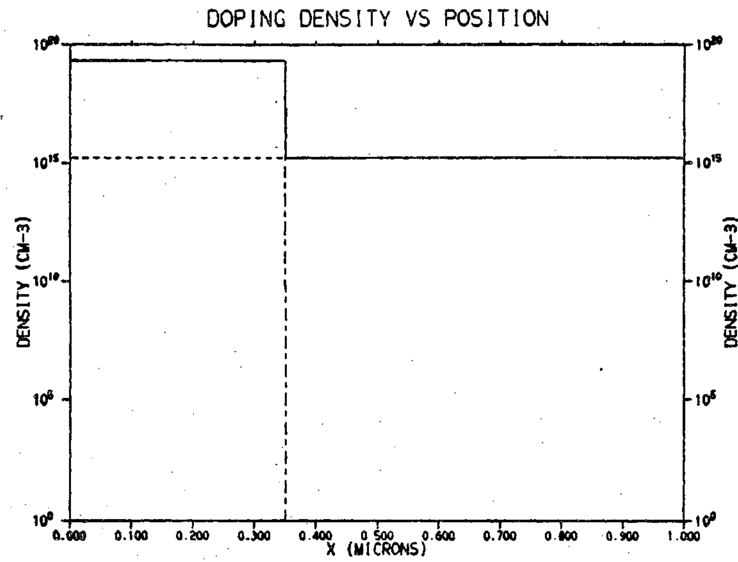

Figure 8.6 Doping profile of an n^+pp^+ photodiode near the emitter.

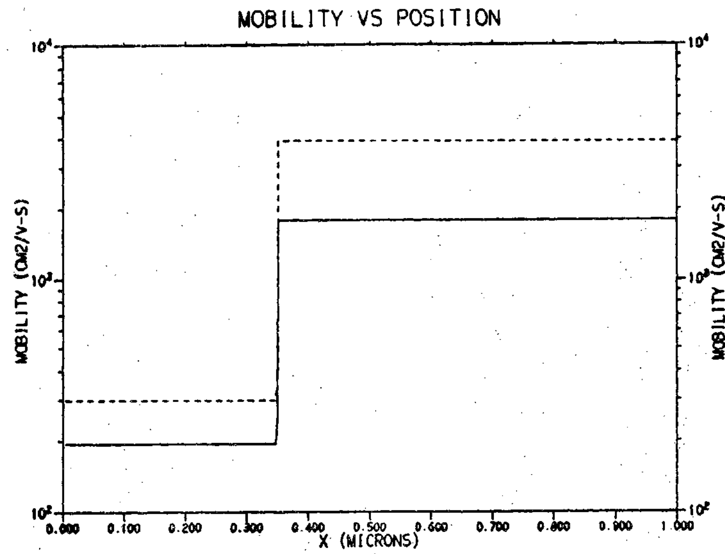

Figure 8.7 Doping-dependent mobility of an n^+pp^+ photodiode for holes and electrons.

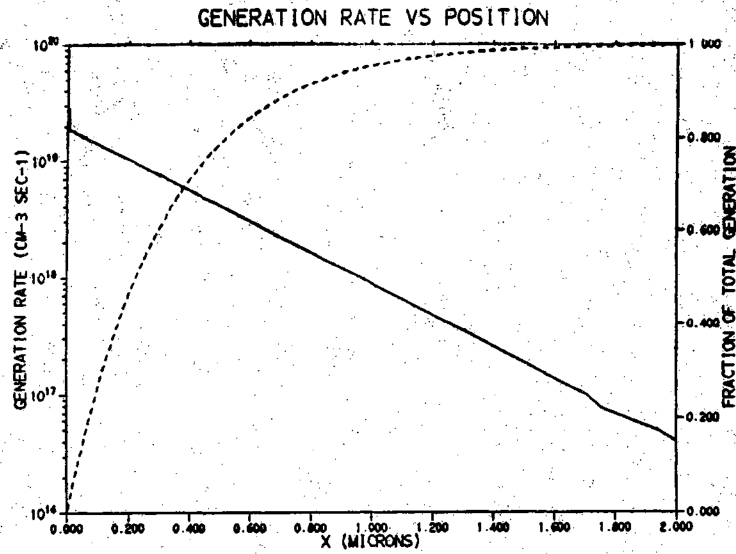

Figure 8.8 Generation rate and integrated generation rate in germanium as a function of position (λ=0.9 μm).

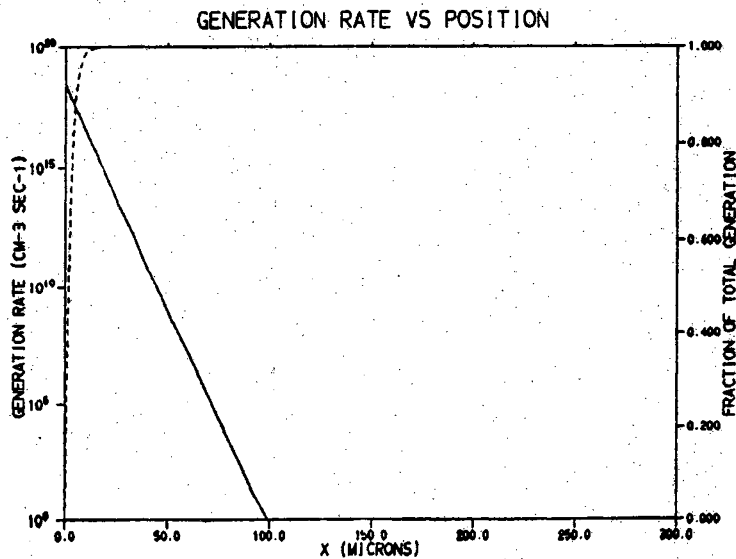

Figure 8.9 Generation rate and integrated generation rate in germanium as a function of position (λ=1.5 μm).

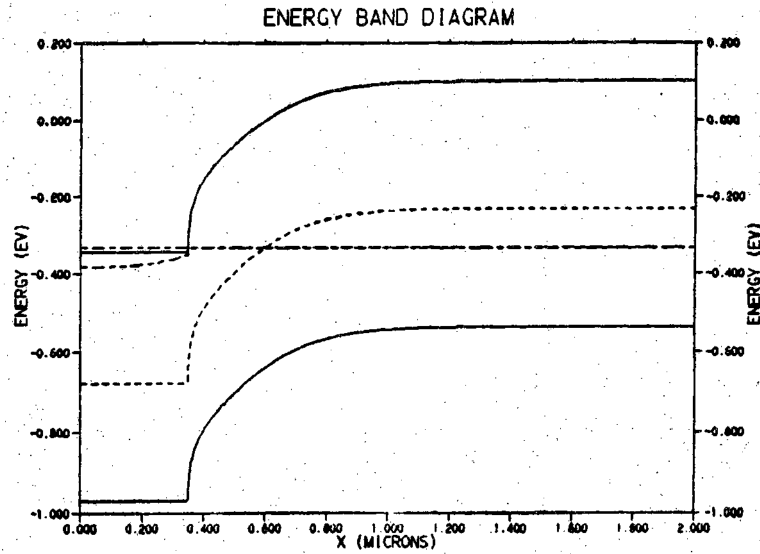

Figure 8.10 Energy band diagram as a function of position in an n^+pp^+ photodiode.

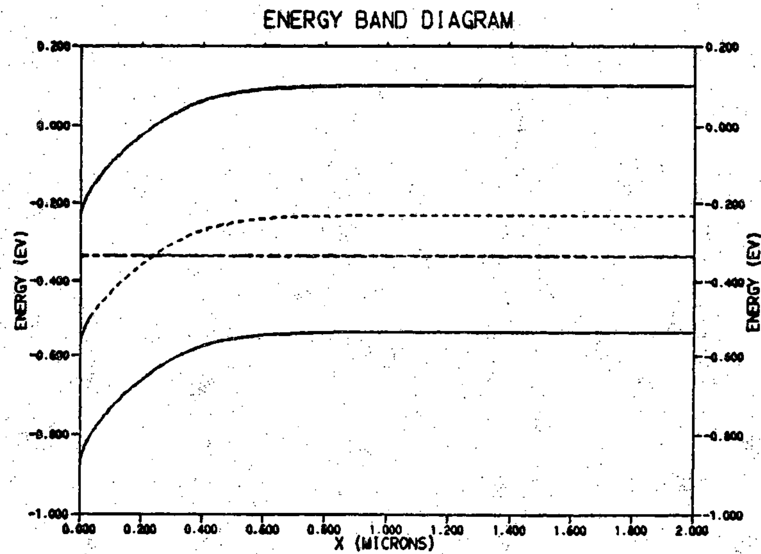

Figure 8.11 Energy band diagram as a function of position in an induced junction photodiode.

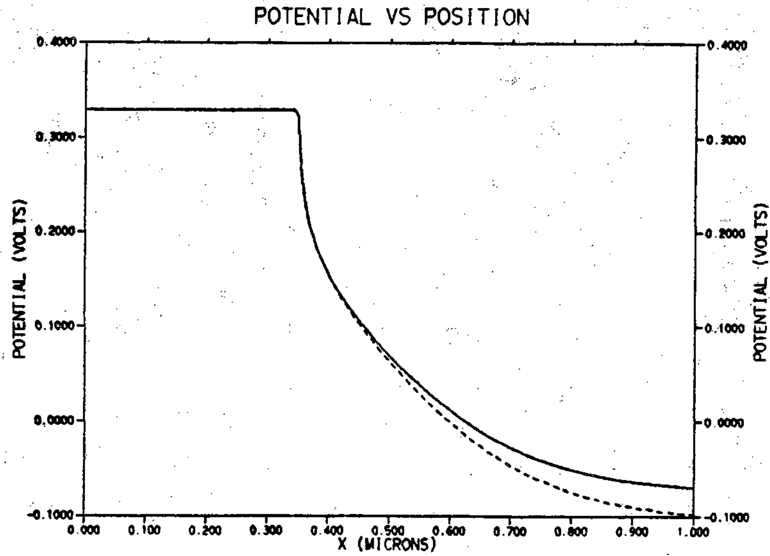

Figure 8.12 Potential and equilibrium potential as a function of position in an n^+pp^+ photodiode.

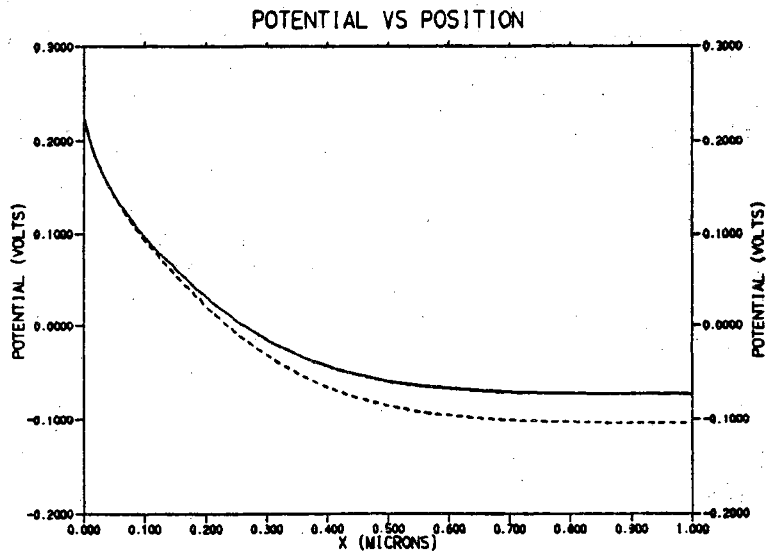

Figure 8.13 Potential and equilibrium potential as a function of position in an induced junction photodiode.

The electrical fields of the devices are plotted in the Fig. 8.14-15. In the n^+pp^+ diode, the high electric field exists in the vicinity of the depletion region. However, in the induced junction diode, the electric field is induced near the surface due to the energy band bending. This surface field helps to separate the photo-generated carriers and increase the collection efficiency.

Fig. 8.16-19 show the recombination rate and the integrated recombination as a function of position. The solid line represents the recombination rate and dashed line the integrated recombination. The dashed line underneath the solid line is the recombination rate due to the SRH recombination. The difference of these two lines is the recombination contributed by Auger recombination process.

Fig. 8.16 and 8.17 show the recombination rate of the radiation of $\lambda=0.9$ μm. The quantum efficiency of the n^+pp^+ diode at 0.9 μm is 66.3% (Fig. 8.4). More than 30% of the photo-generated carriers recombine in the device. Fig. 8.16 shows that about 90% of the total recombination takes place in the emitter region. This is because of the low carrier lifetime in the emitter. However, in the induced junction diode, less than 2% of the photo-generated carriers recombined in the device (Fig. 8.5). Most of the losses take place at the SiO_2-Ge interface (Fig. 8.17).

The recombination rates and integrated recombination of longer wavelength radiation ($\lambda=1.5$ μm) are shown in Fig. 8.18 and 8.19. At this wavelength, more carriers are generated in the base region than that of the short wavelength and thus, more carriers will be collected. The quantum efficiency of the n^+pp^+ diode at $\lambda=1.5$ μm is about 94% and less than 20% of the carrier recombination take place in the emitter region (Fig. 8.19).

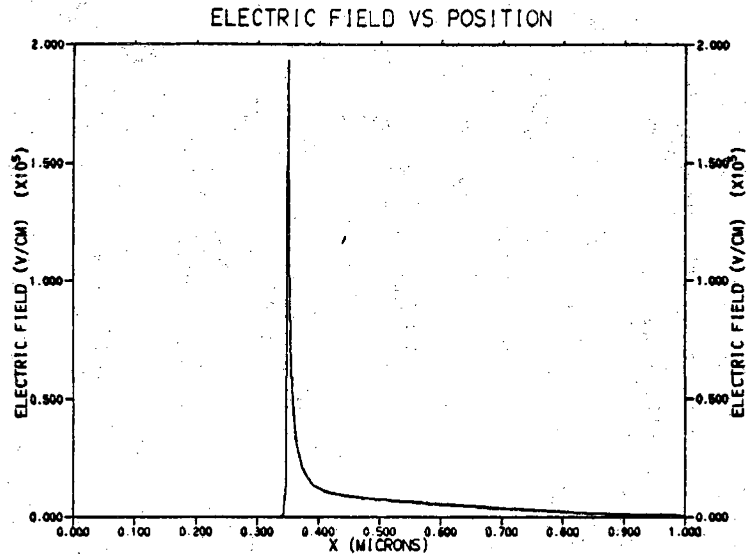

Figure 8.14 Electric field as a function of position in an n^+pp^+ photodiode.

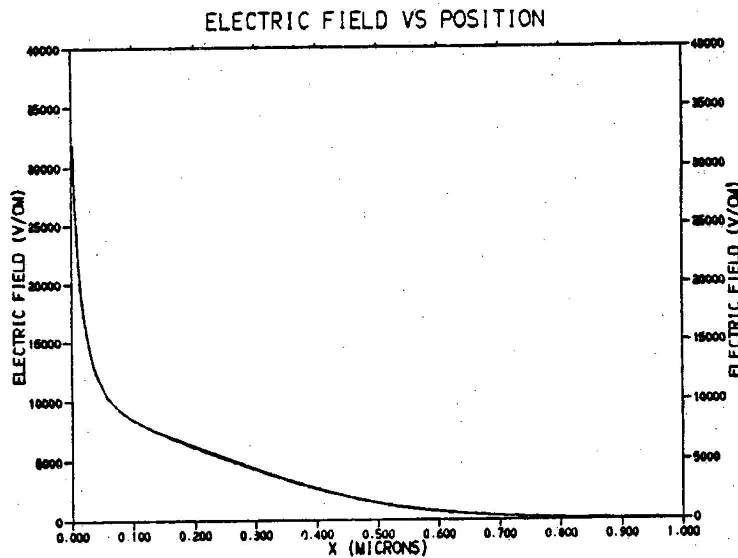

Figure 8.15 Electric field as a function of position in an induced junction photodiode.

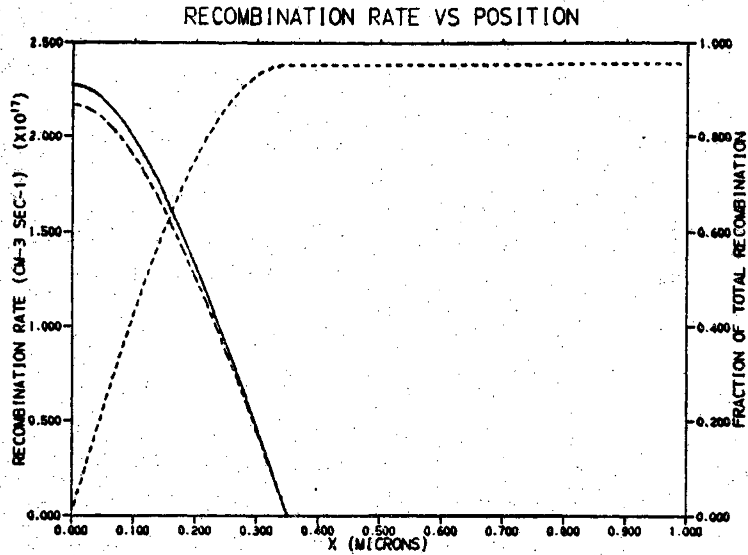

Figure 8.16 Recombination rate and integrated recombination rate as a function of position in an n^+pp^+ photodiode (λ=0.9 μm).

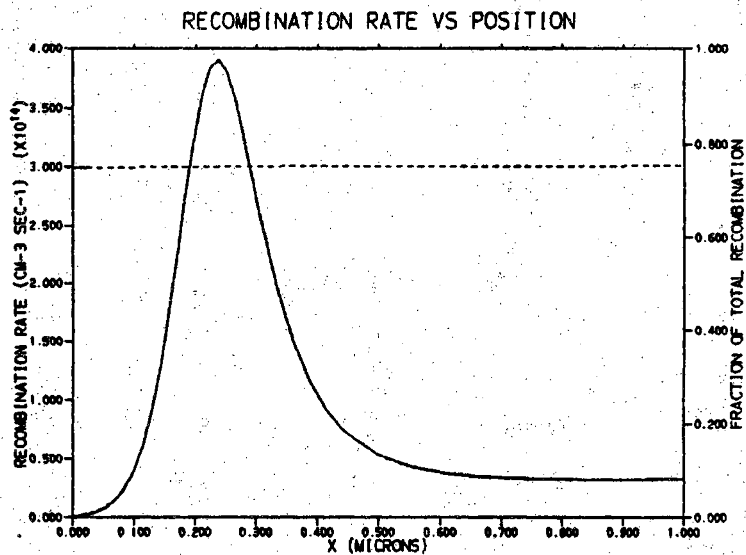

Figure 8.17 Recombination rate and integrated recombination rate as a function of position in an induced junction photodiode (λ=0.9 μm).

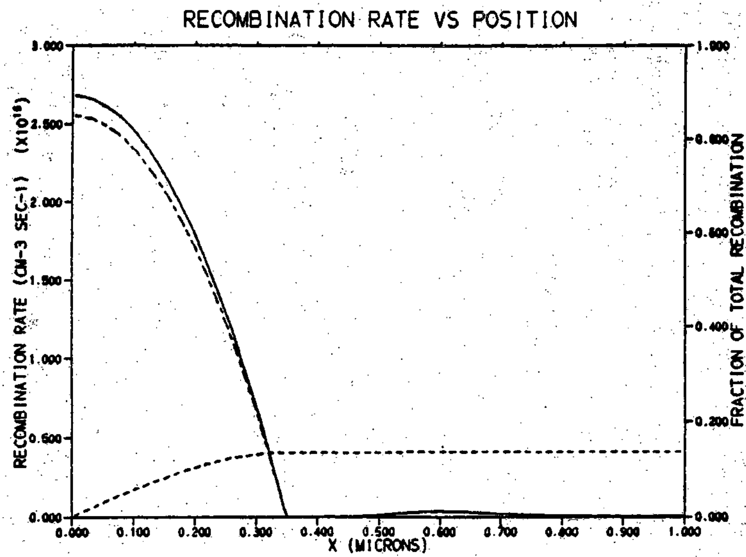

Figure 8.18 Recombination rate and integrated recombination rate as a function of position in an n^+pp^+ photodiode (λ=1.5 μm).

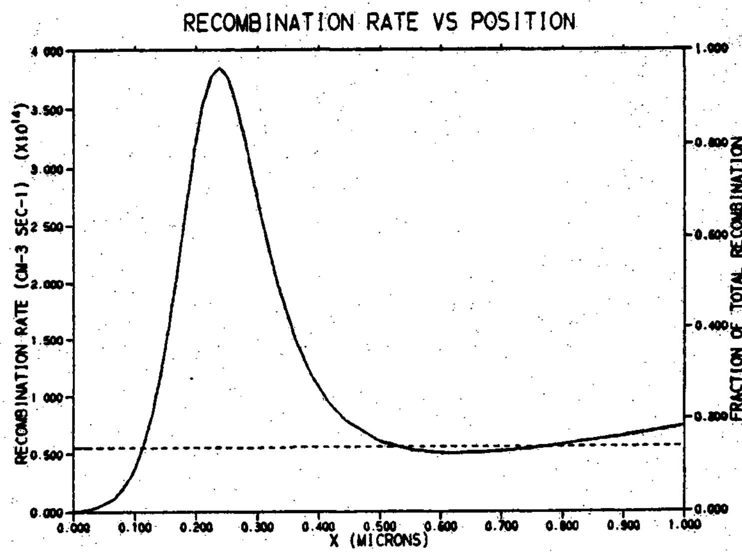

Figure 8.19 Recombination rate and integrated recombination rate as a function of position in an induced junction photodiode (λ=1.5 μm).

Additional physical quantities can be evaluated using the computer codes. Fig. 8.20-23 show the plots of the total carrier concentration and the excess carrier concentrations for electrons and holes in n^+pp^+ and induced junction diode. The high excess carrier in the vicinity of the depletion region is the result of the slightly forward-biased junction under illumination at V=0. The solid lines in the figures are for the holes and dashed lines for the electrons.

Computer simulations can be used to optimize the device performance. For instance, in the implanted diode, a shallow emitter is necessary for high quantum efficiency. Fig. 8.24 shows the effects of emitter junction depth on the quantum efficiency in implanted diodes. The improvement in quantum efficiency with shallow emitters is more noticeable at short wavelengths. In the shallow emitter diode, more carriers are generated in the base where less recombination occurs. As shown in the figure, junction depths of 0.1 μm or less are required in order to have quantum efficiencies comparable with the induced junction diode. Even then the fall off at 0.6 μm is larger.

High surface recombination velocity, S, is another factor limiting the n^+pp^+ diode performance. Fig. 8.25 shows the quantum efficiency of the n^+pp^+ diodes with different values of S. The value of S depends on the treatment during the fabrication and the final passivation of the surface. Since the SiO_2 is used for the passivation layer, a higher surface state density at the SiO_2-Ge interface than that at a SiO_2-Si interface is expected. Fig. 8.25 shows that an S of 10^3cm/sec or better is needed for high quantum efficiency. This requires a high quality SiO_2 interface and is not practical for germanium devices.

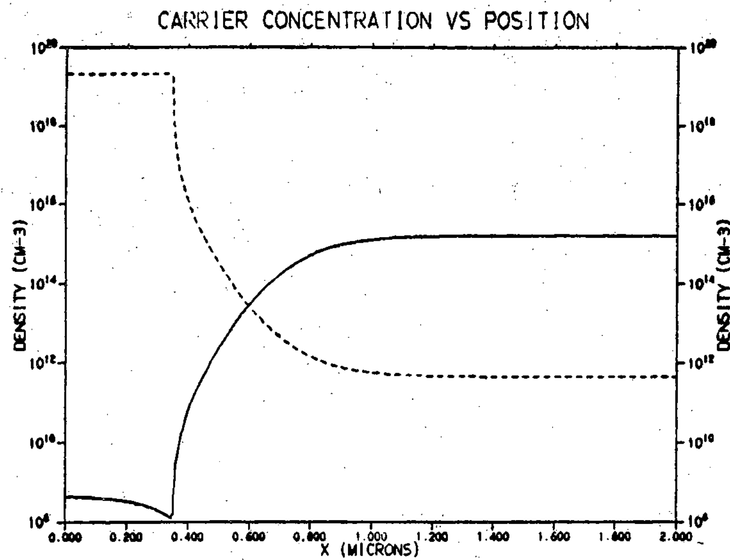

Figure 8.20 Carrier concentration as a function of position in an n^+pp^+ photodiode.

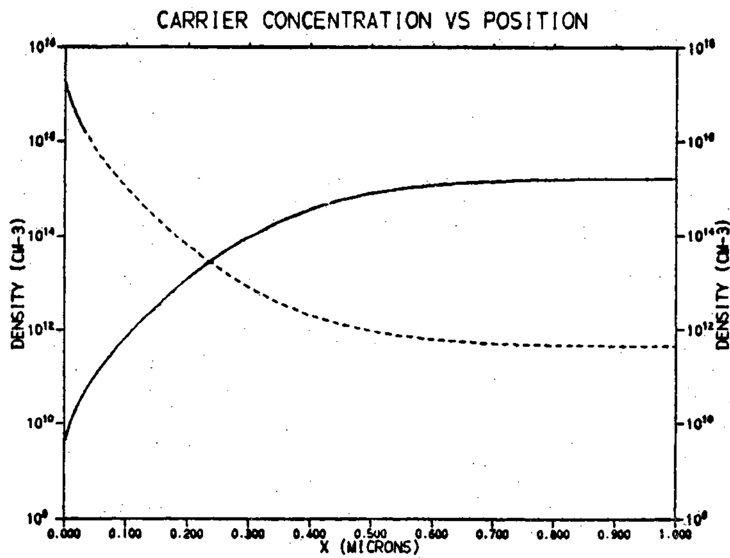

Figure 8.21 Carrier concentration as a function of position in an induced junction photodiode.

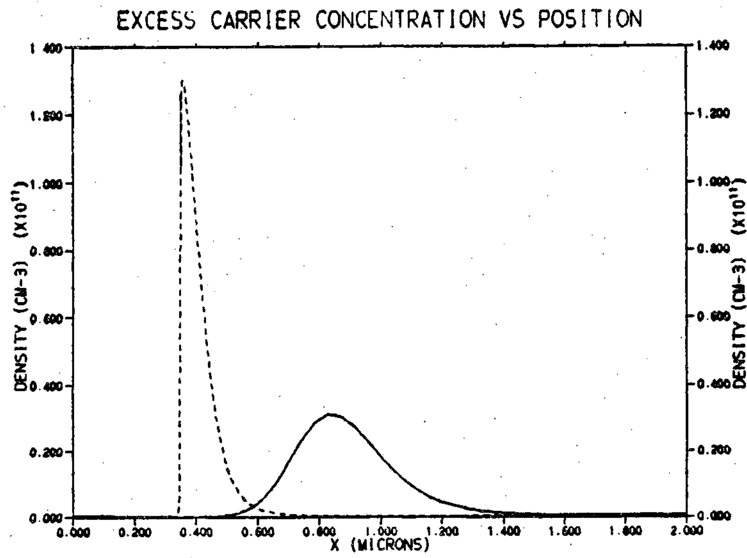

Figure 8.22 Excess carrier concentration as a function of position in an $n^{+}pp^{+}$ photodiode.

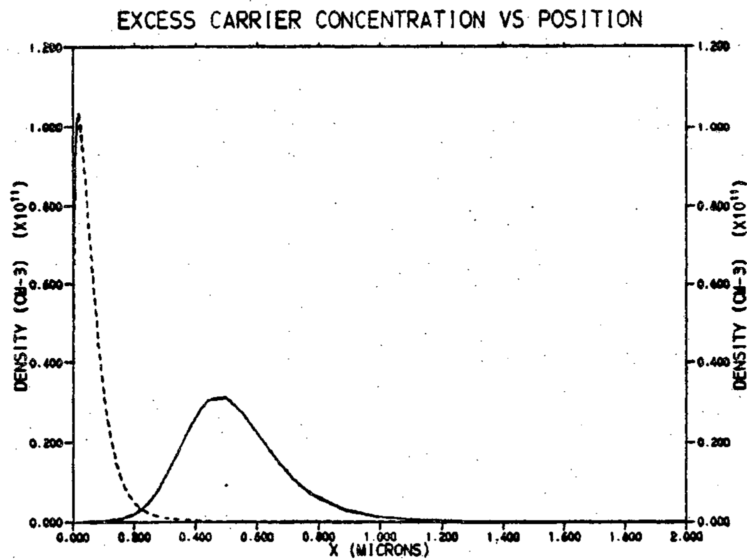

Figure 8.23 Excess carrier concentration as a function of position in an induced junction photodiode.

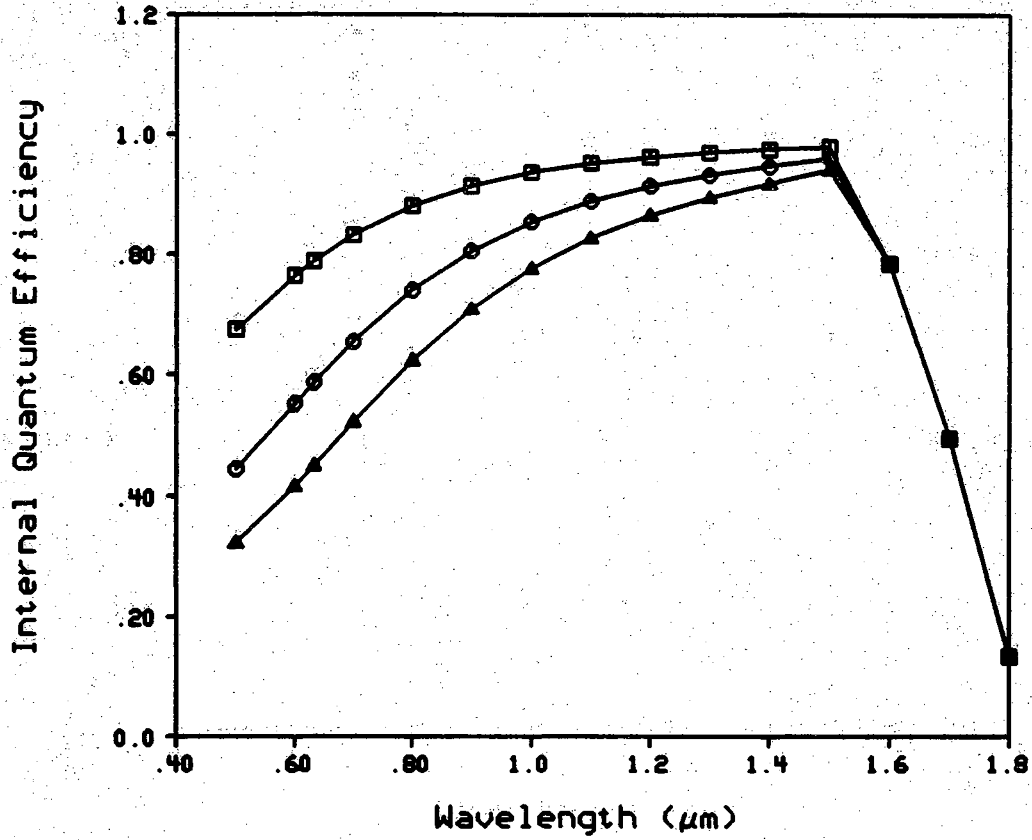

Figure 8.24 Internal quantum efficiency of a n^+pp^+ photodiode with the junction depth of 0.1 μm (□), 0.2 μm (○), and 0.3 μm (△).

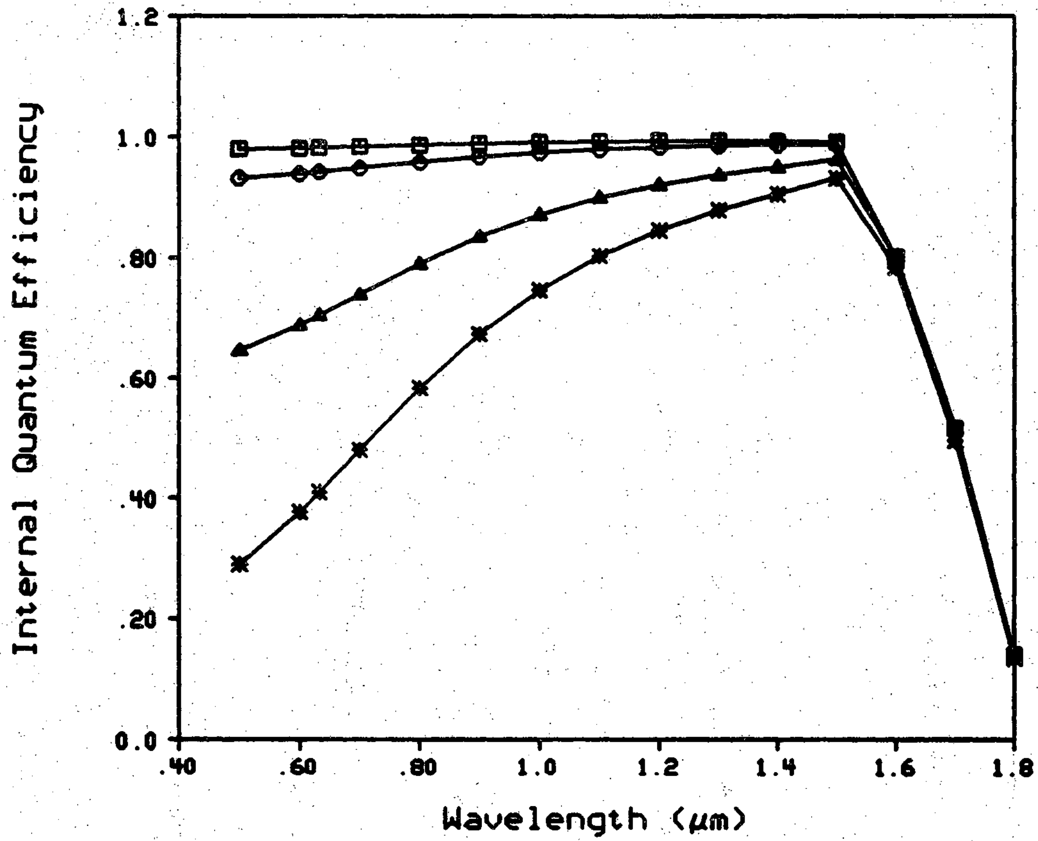

Figure 8.25 Internal quantum efficiency of a $n^{+}pp^{+}$ photodiode with the surface recombination velocity of 10^3 cm/sec (□), 10^4 cm/sec (○), 10^5 cm/sec (△), and 8×10^5 cm/sec (*).

As we have demonstrated with experimental data and theoretical calculation, the quantum efficiency of an induced junction photodiode is less sensitive to the surface recombination velocity and the carrier lifetime in the emitter. However, the induced junction diode requires enough fixed positive charge in the SiO_2 layer to induce a n-type inversion layer on the p-type substrate. Fig. 8.26 shows the changes of the quantum efficiency with different fixed positive charge density, Q_f, in the cells. As shown in the figure, the quantum efficiency starts to degrade if Q_f drops to lower than 2×10^{12} /cm^2.

The quantum efficiency of the induced junction photodiode is a function of the intensity of the incident radiation. Fig. 8.27 shows that the quantum efficiency decreases with increasing intensity of illumination. At high intensity, the large excess carrier concentration near the junction reduces the potential barrier, as indicated in Fig. 8.13. In addition, the lateral flow of the light-generated current along the surface causes a resistive voltage drop and, therefore, further reduces the inversion potential. A two dimension graphic can illustrate this phenomenon. Fig. 8.28 shows the potential of the induced junction diode under low illumination ($q\Phi_o = 10$ mA). At an intensity of 500 mA/cm^2, the potential in the illuminated area decreases and thus, the collection efficiency decreases (see Fig. 8.29).

8.4. Summary

In this chapter, we have described the models used in the computer simulation programs and the code modification made for its use in the simulation of Ge photodiodes. The computer programs solve for V, p, and n,

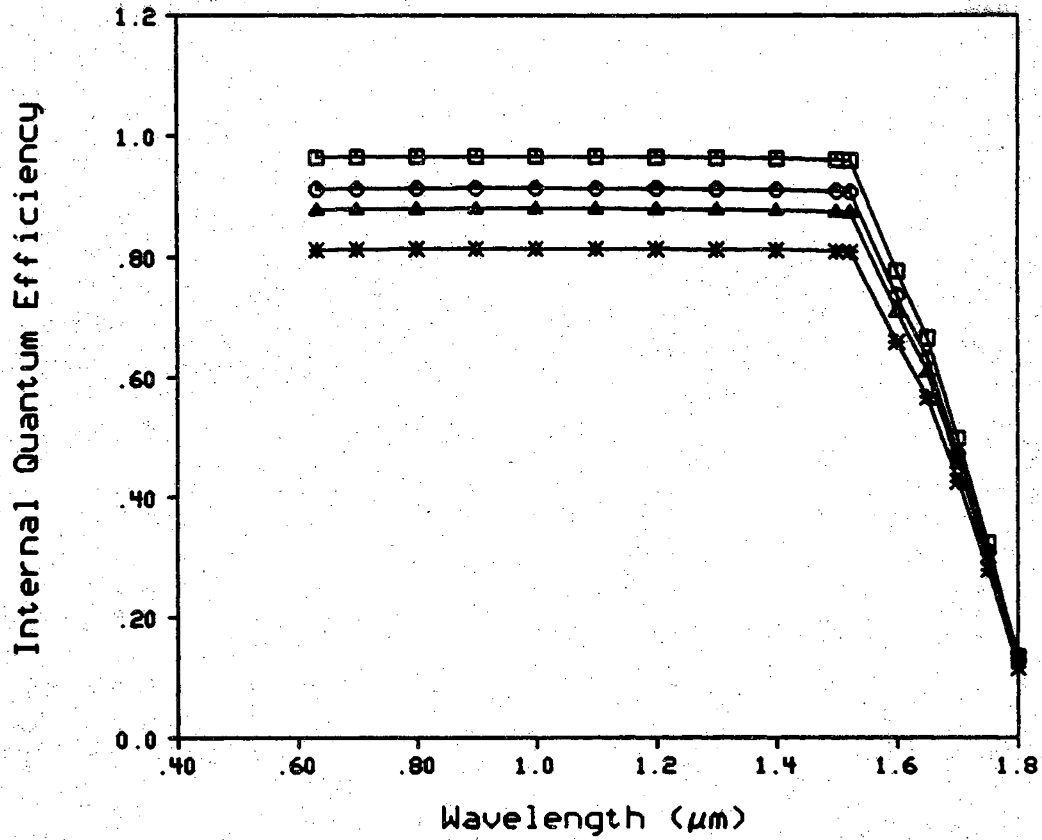

Figure 8.26 Internal quantum efficiency of induced junction photodiodes with fixed positive charge densities of $2\times10^{11}/cm^2$ (□), $10^{12}/cm^2$ (○), $8\times10^{11}/cm^2$ (△), and $6\times10^{11}/cm^2$ (*). The device parameters are shown in Table 8.4.

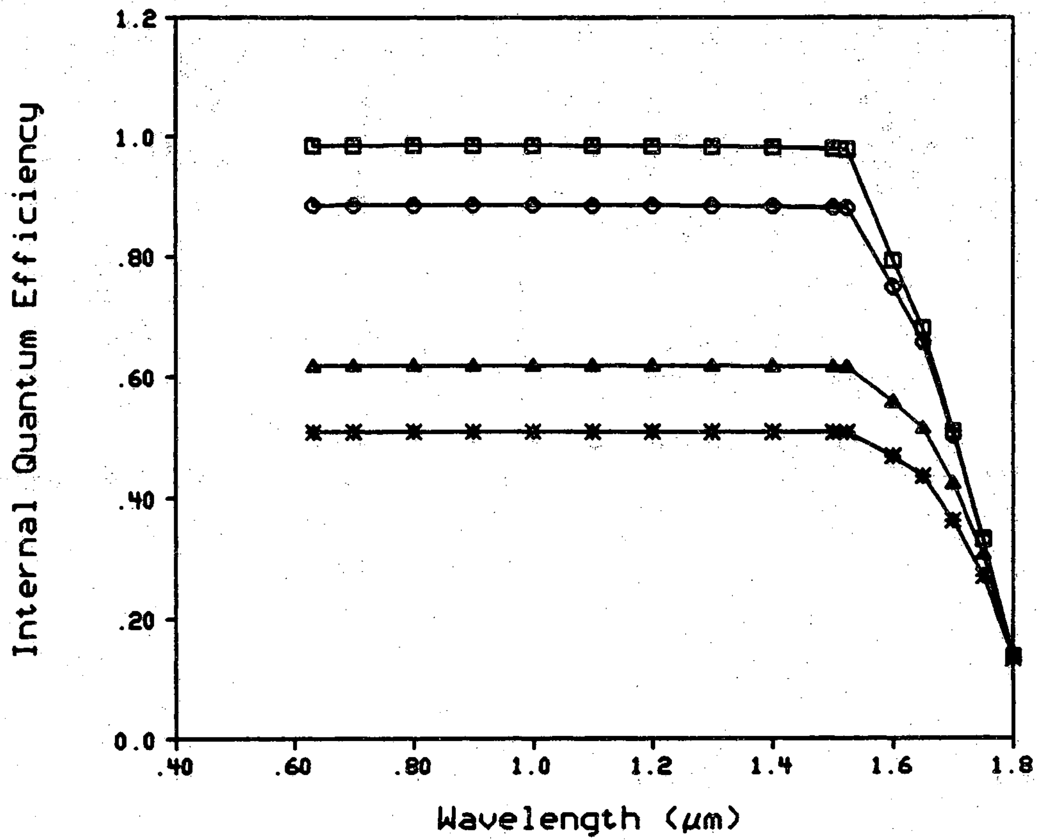

Figure 8.27 Internal quantum efficiency of induced junction photodiodes with the $q\Phi_o$ of 10 mA/cm^2 (□), 100 mA/cm^2 (○), 300 mA/cm^2 (△), and 500 mA/cm^2 (*).

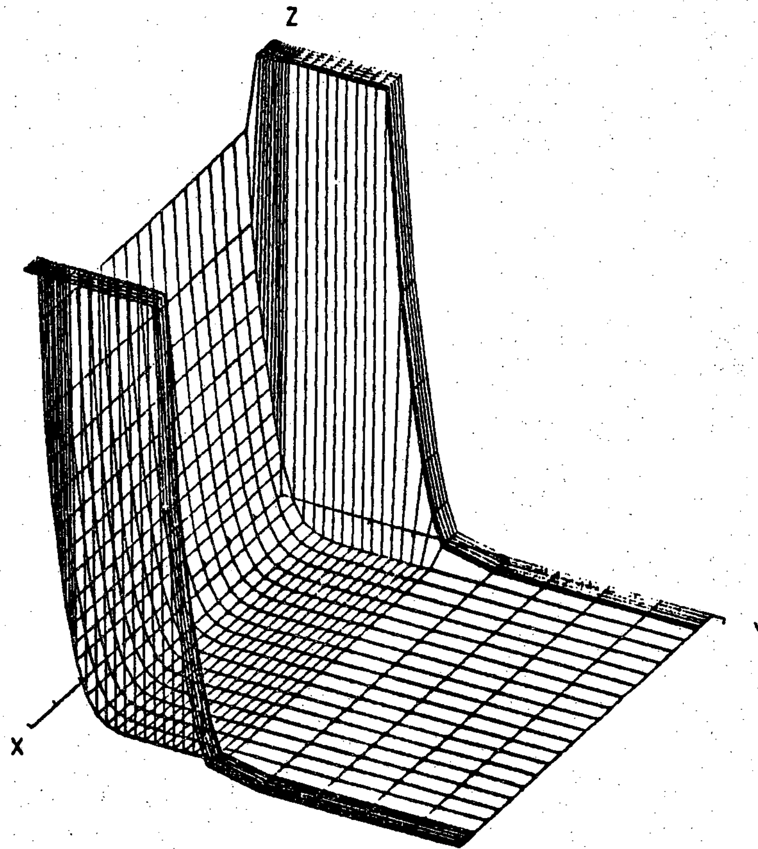

RUN = 1 POTENTIAL

V = 0.000
V = 0.000

X AXIS: 0.000E+00 TO 0.205E+04 MICRONS
Y AXIS: 0.000E+00 TO 0.500E+01 MICRONS
Z AXIS: -0.105E+00 TO 0.329E+00 VOLTS

Figure 8.28 Two-dimensional potential distribution under the low intensity illumination in an induced junction photodiode.

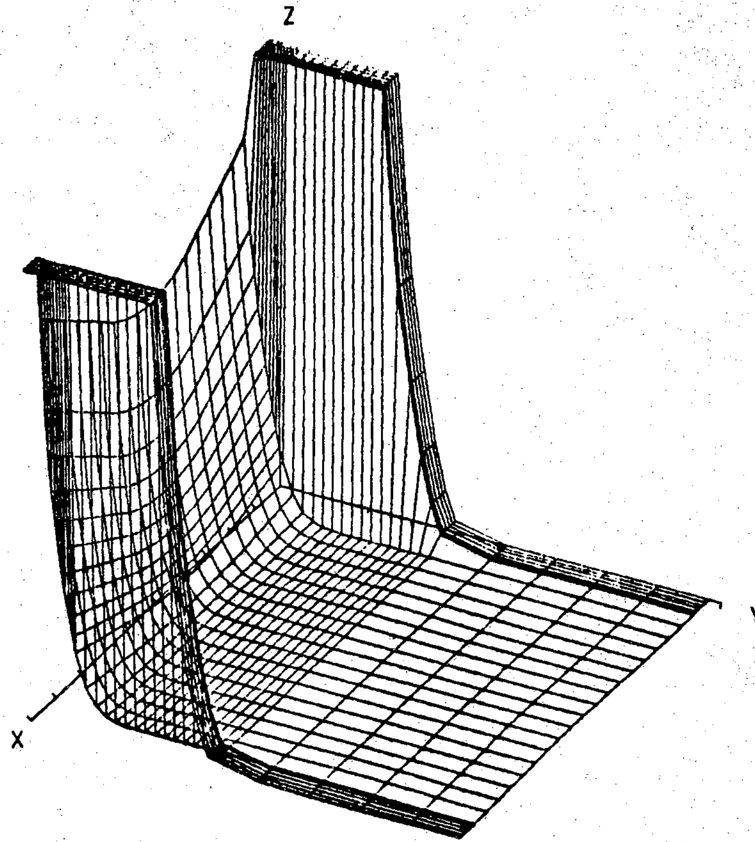

Figure 8.29 Two-dimensional potential distribution under the high intensity illumination in an induced junction photodiode.

and evaluate the physical quantities in the devices. We also demonstrated that the theoretical calculations have excellent agreement with the experiment data.

The simulations showed that high recombination occurs at the SiO_2-Ge interface and in the emitter for the n^+pp^+ photodiode. This is because of the high surface recombination velocity at the surface and low carrier lifetime in the emitter. A shallow emitter ($x_j < 0.1$ μm) and high quality surface ($S < 10^3$cm/sec) are required for a high quantum efficiency n^+pp^+ cell.

The induced junction photodiode is less sensitive to the surface recombination velocity and carrier lifetime. This is because the fixed positive charge in the SiO_2 induced a strong electric field near the surface. This electric field helps to collect the photo-generated electron-hole pairs and therefore, improves the quantum efficiency. The simulations demonstrated that the induced junction diodes are sensitive to the fixed charge density in the SiO_2 layer and the intensity of the illumination.

CHAPTER IX
SUMMARY AND CONCLUSIONS

9.1. Summary

This research is concerned with design and fabrication of an absolute radiometric detector operated over 0.7 to 1.5 μm wavelength range. This application requires a semiconductor photodiode with high internal quantum efficiency and long term stability. Of many possible materials, germanium is chosen because high quality material is available, the fabrication processes are relatively straight forward, and a high quantum efficiency is achievable.

First planar fabrication procedures for a germanium diode were developed. These fabrication processes require the adaptation of existing silicon planar monolithic techniques to germanium. Ion implantation techniques were used to form the p-n junctions, guard rings and back surface field, followed by a 650-700°C thermal anneal to electrically activate the impurities. This annealing process is crucial to the device performance. To reduce the surface recombination, CVD SiO_2 was deposited for surface passivation. A Ti/Pd/Ag metal layer was then sputtered to make the interconnections. Finally, the device was mounted on a TO-8 header for testing.

Two type of germanium photodiodes were fabricated and tested. Dark currents as low as 0.35 mA/cm^2 have been observed on the 2 Ω-cm substrate. The n^+pp^+ photodiode had a considerably lower quantum

efficiency (η) than an induced junction photodiode. This is especially true at the short wavelengths. The simulation analysis showed the low η is attributed to the low carrier lifetime in the emitter and the high surface recombination velocity at the SiO_2-Ge interface. On the other hand, the induced junction cells were less sensitive to the emitter carrier lifetime and the surface recombination velocity. The high quantum efficiency in the induced junction photodiode can be attributed to two causes: (1) the ion-implantation induced damage is not present in the cell, and (2) an electric field induced near the surface aids the collection of the photo-generated carriers.

The device simulation programs developed for solar cell analysis were modified for use in modeling germanium photodiodes. We have demonstrated the excellent agreement between the theoretical calculations and the experimental data for both the n^+pp^+ and induced junction photodiodes. As indicated in the simulation, the induced junction cell is sensitive to the number of the fixed charges in the SiO_2, and the intensity of the light source.

9.2. Conclusions

In this research, we have successfully developed the planar fabrication processes for a germanium photodiode. It is demonstrated that the induced junction photodiode performs significantly better than the n^+pp^+ photodiode, as far as the internal quantum efficiency is concerned. With the induced junction structure, we have observed a quantum efficiency of 98.8% at 0.7 μm and of 97.4% at 1.5 μm. This is by far the highest quantum efficiency ever reported for the germanium diodes. The induced junction cell

is, therefore, suitable for the absolute self-calibrating radiometric application over 0.7 to 1.5 μm wavelength range. The accuracy of this application is within 3% of unity. Future study should be concentrated on the optimization of the fixed oxide charge in the SiO_2 to increase the quantum efficiency.

In some applications, however, the possibility of exposure to the high energy radiation may present a problem since this can neutralize the oxide charge and cause degradation of the surface inversion [73,74]. Therefore, there is still a need to develop a ultra-shallow emitter junction diode that is as responsive in short wavelengths as the induced junction diode. Theoretical calculations have shown that high quantum efficiency n^+pp^+ cell requires that the emitter be less than 0.1 μm thick and the surface be well passivated. Special processes have to be developed to fabricate a ultra-shallow emitter diode. For instance, diffusing the impurities through a thin SiO_2 layer to form a junction 0.1 μm in depth has been reported [75]. The junction can also be formed by low energy ion implantation, followed by a rapid annealing which provides high temperature for the impurity activation, and for a short period of time to prevent the change of impurity profiles.

LIST OF REFERENCES

LIST OF REFERENCES

[1] J. Geist and W. R. Blevin, "Chopper Stabilized Null Radiometer Based Upon an Electrically Calibrated Pyroelectric Detector," *Appl. Opt.*, Vol. 12, pp. 2532, 1973.

[2] J. Geist, "On the Possibility of an Absolute Radiometric Standard Based On the Quantum Efficiency of a Silicon Photodiodes," *SPIE, Measurements of Optical Radiations,* Vol. 196, pp. 75-83, 1979.

[3] E. F. Zalewski and J. Geist, "Silicon Photodiode Absolute Spectral Response Self-calibration," *Appl. Opt.*, Vol. 19, pp. 1214-1216, April 1980.

[4] E. F. Zalewski and C. R. Duda, "Silicon Photodiode Device with 100% External Quantum Efficiency," *Applied Optics,* Vol. 22, No. 18, pp. 2867-2873, September 1983.

[5] H. Osanai, T. Shioda, T. Moriyama, S. Araki, M. Horiguchi, T. Izawa and H. Takata, "Effect of Dopants on Transmission Loss of Low-OH-content Optical Fibers," *Electronics Lett.*, Vol. 12, No. 21, pp. 549-550, 1976.

[6] D. N. Payne and W. A. Gambling, "Zero Material Dispersion in Optical Fibers," *Electronic Lett.*, Vol. 11, No. 8, pp. 176-178, 1975.

[7] F. T. Arecchi and Schulz-Dubois, editors, *Laser Handbook,* North-Holland Pub. Co., 1972.

[8] A. G. Milnes, *Deep Impurities in Semiconductors,* John Wiley & Sons, 1973.

[9] R. K. Willardson and A. C. Beer, editors, *Semiconductors and Semimetals, Vol. 12,* Chap. 2, Academic Press, New York, N. Y., 1977.

[10] R. P. Riesz, "High Speed Semiconductor Photodiodes," *Rev. Sci. Inst.*, Vol. 33, pp. 994-998, September 1962.

[11] S. R. Forrest, "Performance of $In_xGa_{1-x}As_yP_{1-y}$ Photodiodes with Dark Current Limited by Diffusion, Generation Recombination, and Tunneling," *IEEE J. Quant. Electron,* Vol. QE-17, No. 2, pp. 217-226, 1981.

[12] G. H. Olsen, "Low-Leakage, High-Efficiency, Reliable VPE InGaAs 1.0-1.7 μm Photodiodes," *IEEE Electron Dev. Lett.,* Vol. EDL-2, No. 9, pp. 217-219, 1981.

[13] C. E. Hurwitz and J. J. Hsieh, "GaInAsP/InP Avalanche Photodiodes," *Appl. Phys. Lett.,* Vol. 32, pp. 487-489, April 1978.

[14] H. Melchior and W. T. Lynch, "Signal and Noise Response of High Speed Germanium Avalanche Photodiodes," *IEEE Trans. on Electron Devices,* Vol. ED-13, No. 12, pp. 829-838, December 1966.

[15] T. Shibata, Y. Igarashi and K. Yano, "Passivation of Germanium Devices (III)," *Rev. of the Electrical Communication Laboratories,* Vol. 22, No. 11-12, pp. 1069-1077, November-December, 1974.

[16] H. Ando, H. Kanbe, T. Kimura, T. Yamaoka and T. Kaneda, "Characteristics of Germanium Avalanche Photodiodes in the Wavelength Region of 1-1.6 μm," *IEEE J. of Quantum Electronics,* Vol. QE-14, No. 11, pp. 804-809, November 1974.

[17] T. Mikawa, S. Kagawa and T. Kaneda, "Germanium Avalanche Photodiodes for Optical Communication Systems," *FUJITSU Scientific & Technical Journal,* pp. 95-119, June 1980.

[18] T. Kaneda, H. Fukuda, T. Mikawa, Y. Bonda and Y. Toyama, "Shallow Junction p^+-n Germanium Avalanche Photodiodes (APD's)," *Appl. Phys. Lett.,* Vol. 34, No. 12, pp. 866-868, 15 June 1979.

[19] H. Kanbe and G. Grosskopf, "Dark Current Noise Properties of a Germanium Avalanche Photodiodes," *Japn. J. of Appl. Phys.,* Vol. 19, No. 12, pp. L767-L770, December 1980.

[20] S. Kagawa, T. Kanede, T. Mikawa, Y. Banba and Y. Toyama, "Fully Ion-Implanted p^+-n Germanium Avalanche Photodiodes," *Appl. Phys. Lett.,* Vol. 38, No. 6, pp. 429-431, 15 March 1981.

[21] T. Mikawa, T. Kaneda, H. Nishimoto, M. Motegi and H. Okushima, "Small-Active-Area Germanium Avalanche Photodiode for Single-Mode Fibre at 1.3 μm Wavelength," *Electronics Lett.,* Vol. 19, No. 13, June 1983.

[22] M. Niwa, Y. Tashiro, K. Minemura and H. Iwasaki, "High Sensitivity Hi-Lo Germanium Avalanche for 1.5 μm Wavelength Region Single Mode Optical Fibre Communication Use," *NEC Res. & Develop.*, No. 77, pp. 13-21, April 1985.

[23] T. Kaneda, S. Kagawa, T. Mikawa and Y. Toyama, "An n^+-n-p Germanium Avalanche Photodiode," *Appl. Phys. Lett.*, Vol. 36, No. 7, pp. 572-574, 1 April 1980.

[24] O. Mikami, H. Ando, H. Kanbe, T. Mikawa, T. Kaneda and Y. Toyama, "Improved Germanium Avalanche Photodiodes," *IEEE J. of Quantum Electronics,* Vol. QE-16, No. 9, pp. 1002-1007. September 1980.

[25] T. Mikawa, S. Kagawa, T. Kaneda, T. Sakuri, H. Ando and O. Mikami, "A Low-Noise n^+np Germanium Avalanche Photodiode," *IEEE J. of Quantum Electronics,* Vol. QE-17, No. 2, pp. 210-216, February 1981.

[26] T. E. Hansen, "Silicon UV-Photodiodes Using Natural Inversion Layers," *Physica Scripta,* Vol. 18, pp. 471-475, 1978.

[27] M. E. Straumanis and E. Z. Aka, "Lattice Parameters, Coefficients of Thermal Expansion, and Atomic Weights of Purest Silicon and Germanium," *J. Appl. Phys.*, Vol. 23, No. 3, pp. 330-334, March 1952.

[28] W. C. Dunlap, *Introduction to Semiconductors,* Wiley, New York, N. Y., 1957.

[29] J. R. Chelikowsky and M. L. Cohen, "Nonlocal Pseudopotential Calculations for the Electronic Structure of Eleven Diamond and Zinc-Blende Semiconductors," *Phys. Rev.,* Vol. 14, No. 2, pp. 556-582, 15 July 1976.

[30] Kohn, *Solid State Physics,* Academic Press, New York, N. Y., 1957.

[31] M. B. Prince, "Drift Mobilities in Semiconductors. I. Germanium," *Phys. Rev.,* Vol. 92, No. 3, pp. 681-687, 1 November 1953.

[32] F. J. Morin, "Lattice Scattering Mobility in Germanium," *Phys. Rev.,* Vol. 93, pp. 62-63, 1 January 1954.

[33] R. A. Smith, *Semiconductors, 2nd ed.,* Cambridge University Press, London, 1979.

[34] W. C. Dash and R. Newman, "Intrinsic Optical Absorption in Single Crystal Germanium and Silicon at 77°K and 300°K," *Phys. Rev.,* Vol. 99, No. 4, pp. 1151-1155, 15 August 1955.

[35] W. Kaiser, R. J. Collins and H. Y. Fan, "Infrared Absorption in P-Type Germanium," *Phys. Rev.,* Vol. 91, pp. 1380-1381, 15 September 1953.

[36] P. Aigrain, "Theory of Impurity Bands with Randomly Distributed Centers," *Physica,* Vol. 20, No. 11, pp. 978-982, 1954.

[37] E. O. Kane, "Thomas-Fermi Approach to Impure Semiconductor Band Structure," *Phys. Rev.,* Vol. 131, No. 1, pp. 79-88. 1 July 1963.

[38] V. L. Bonch-Bruevich, "On the Theory of Degenerate Semiconductors," *Proc. Internat. Conf. on Phys. of Semiconductors,* Exeter, pp. 216-219, 1962.

[39] G. D. Mahan, "Energy Gap in Si and Ge: Impurity Dependence," *J. Appl. Phys.,* Vol. 51, No. 5, pp. 2634-2646, May 1980.

[40] J. I. Pankove, *Optical Processes in Semiconductors,* Prentice-Hill Inc., N. J., 1971.

[41] O. Christensen, "Quantum Efficiency of the Internal Photoelectric Effect in Silicon and Germanium," *J. Appl. Phys.,* Vol. 47, No. 2, pp. 689-695, February 1976.

[42] W. Schockley, "Problems Related To P-N Junctions in Silicon," *Czech. J. Phys.* B 11, pp. 81-121, 1961.

[43] J. Dziewior and W. Schmid, "Auger Coefficients for Highly Doped and Highly Excited Silicon," *Appl. Phys. Lett.,* Vol. 31, No. 5, pp. 346-348, 1 September 1977.

[44] J. Geist, "Quantum Efficiency of the p-n Junction in Silicon as an Absolute Radiometric Standard," *Appl. Opt.,* Vol. 18, No. 6, pp. 760-762, March 1979.

[45] H. J. Hovel, *Semiconductors and Semimetals, Vol. 11, Solar Cells,* Academic Press, 1975.

[46] T. E. Hansen, "Silicon UV-Photodiodes Using Natural Inversion Layers," *Physica Scripta,* Vol. 18, pp. 471-475, 1978.

[47] M. S. Lundstrom, R. J. Schwartz and J. L. Gray, "Transport Equations for the Analysis of Heavily Doped Semiconductor Devices," *Solid-State Electronics,* Vol. 24, pp. 195-202, 1981.

[48] A. Many, Y. Goldstein and N. B. Grover, *Semiconductor Surfaces,* John Wiley & Sons, Inc., New York, N. Y., 1965.

[49] J. G. Fossum, R. D. Nasby, and S. C. Pao, "Physics Underlying the Performance of Back-Surface-Field solar Cells," *IEEE Trnas. on Electron Devices,* Vol. ED-27, No. 4, pp. 785-791, April 1980.

[50] T. O. Sedgwick, J. A. Aboaf, and S. Krongelb, "Passivating, Masking, Mechanical and Electrical Properties of Dielectric Films for Ge-Planar Devices," *IBM Research Report, RC2573(#12295),* August 8, 1969.

[51] K. Watanabe, T. Tanigaki, and S. Wakayama, "The Properties of LPCVD SiO_2 Film Deposited by SiH_2Cl_2 and N_2O Mixtures," *J. Electrochem. Soc.,* Vol. 128, No. 12, pp. 2630-2635, 1981.

[52] H. Hupertz, and W. L. Engl, "Modeling of Low-Pressure Deposition of SiO_2 by Decomposition of TEOS," *IEEE Trans. on Electron Devices,* Vol. ED-26, No. 4, pp. 658-662, 1979.

[53] T. Yashiro, "Frequency and Temperature Dependence of C-V Characteristics at Ge—SiO_2 Interface and BT Treatments," *Japn. J. of Appl. Phys.,* Vol. 9, No. 7, pp. 740-747, July 1970.

[54] S. M. Sze, *Physics of Semiconductor Devices, 2nd Edition,* John Wiley & Sons, Inc., 1981.

[55] T. O. Sedgwick, "Dominant Surface Electronic Properties of SiO_2-Passivated Ge Surfaces as a Function of Various Annealing Treatments," *J. of Appl. Phys.,* Vol. 39, No. 11, pp. 5066-5077, October 1968.

[56] K. L. Wang, and P. V. Gray, "Relationships of the Chemical and Electrical Interfacial Properties of Germanium-SiO_2 Systems," *J. Electrochem. Soc.,* Vol. 123, No. 9, pp. 1392-1398, September 1976.

[57] R. F. Pierret, *Modular Series on Solid State Devices, Vol. IV, Field Effect Devices,* Addison-Wesley Publishing Co., 1983.

[58] J. F. Gibbons, W. S. Johnson, and S. W. Mylroie, *Projected Range Statistics, Semiconductor and Related Materials, 2nd Edition,* Halstead Press 1975.

[59] M. Y. Tsai, and B. G. Streetman, "Recrystallization of Implanted Amorphous Silicon Layers, I. Electrical Properties of Silicon Implanted with BF_2^+ or $Si^+ + B^+$," *J. Appl. Phys.,* Vol. 50, No. 1, pp. 183-187, 1979.

[60] G. A. Lee, "Multilayer Analysis of Spreading Resistance Measurements," *Spreading Resistance Symposium,* Proceeding of a Symposium Held at NBS, Gaithersburg, Md., pp. 75-94, June 13-14, 1974.

[61] F. M. Smits, "Measurement of Sheet Resistivities with the Four Point Probe," *Bell Syst. Tech. J.,* Vol. 37, pp. 711-718, 1958.

[62] M. S. Lundstrom, "Numerical Analysis of Silicon Solar Cells," *Tech. Report TR-EE 80-27,* Purdue University, December 1980.

[63] J. L. Gray, "Two-Dimensional Modeling of Silicon Solar Cells," *Tech. Report TR-EE 82-12,* Purdue University, August 1982.

[64] C. D. Thurmond, "The Standard Thermodynamic Functon of the Formation of Electrons and Holes in Ge, Si, GaAs and GaP," *J. Electrochem. Soc.,* Vol. 122, No. 8, pp. 1133-1141, 1975.

[65] G. D. Mahan, "Energy Gap in Si and Ge: Impurity Dependence," *J. Appl. Phys.,* Vol. 51, No. 5, pp. 2634-2646, May 1980.

[66] J. I. Pankove, *Optical Processes in Semiconductors,* Prentice-Hill Inc., N. J., 1971.

[67] D. M. Caughey and R. F. Thomas, "Carrier Mobilities in Silicon Empirically Related to Doping and Field," *Proceedings of IEEE (Letters),* pp. 2192-2193, 1967.

[68] M. S. Adler, "Accurate Calculations of the Forward Drop and Power Dissipation in Thyristors," *IEEE Trans. on Electron Devices,* No. ED-25, pp. 16-22, January 1978.

[69] K. Raikanan, R. Singh and J. Shewchun, "Absorption Coefficient of Silicon for Solar Cell Calculations," *Solid State Electronics,* Vol. 22, pp. 793-795, 1979.

[70] I. V. Karpova and S. G. Kalashnikov, "Electron and Hole Lifetimes in Highly Doped Germanium," *Soviet Phys. - Solid State,* Vol. 5, No. 1, pp. 219-223, July 1963.

[71] J. F. Battey and R. M. Baum, "Carrier Capture Probabilities in Nickel Doped Germanium," *Phys. Rev.,* Vol. 100, No. 6, pp. 1634-1637, Dec. 15, 1955.

[72] J. Okada, "Recombination Centers in Germanium," *J. of Japan Phys. Soc.,* Vol. 13, No. 8, pp. 793-800, Aug. 1958.

[73] H. Ouchi, T. Mukai, T. Kamei, and M. Okamura, "Silicon p-n Junction Photodiodes Sensitive to Ultraviolet Radiation," *IEEE Tran. on Electron Devices,* Vol. ED-26, No. 12, pp. 1965-1969, December 1979.

[74] R. Korde and J. Geist, "Stable, High Quantum Efficiency, UV-Enhanced Silicon Photodiodes by Arsenic Diffusion," *Solid State Electronics,* Vol. 30, No. 1, pp. 89-92, 1987.

[75] W. V. Munch, "Double-junction Photosensitive Devices with High UV Responsivity," *Japn. J. Appl. Phys.,* Vol. 16, Suppl. 16-1, pp. 271-274, Jan. 1977.

[76] W. Budde, *Optical Radiation Measurements, Vol. 4, Physical Detectors of Optical Radiation,* pp. 215-231, Academic Press Inc., 1983.

APPENDIX

APPENDIX

FABRICATION PROCEDURES

1. Initial wafer clean
    - rinse in warm Acetone.
    - ultrasonic clean in Trichloroethylene (TCE) for three minutes.
    - ultrasonic clean in Acetone for one minute.
    - ultrasonic clean in Methanol for one minute.
    - rinse in DI water for five minutes.
    - ultrasonic clean in H_2O : HF (10:1) solution for one minute.
    - rinse in DI water for five minutes.
    - blow dry in N_2.
2. CVD oxidation
    - temperature: 400°C
    - thickness: 4000 Å
3. Open window for p^+ channel stop (mask #1)
4. Channel stop and back surface implantation
    - impurity: boron
    - dosage/energy: $10^{15}cm^{-2}$/25Kev
5. Wafer clean
6. CVD oxidation
    - temperature: 400°C
    - thickness: 7000 Å
7. Open window for deep n^+ implantation (mask #2).

8. Deep n^+ implantation
    - impurity: arsenic
    - dosage/energy: $4\times10^4 cm^{-2}$/70Kev
9. CVD oxidation
    - temperature: 400°C
    - thickness: 5000 Å
10. Open window for the shallow n^+ implantation (mask #3).
11. Shallow n^+ implantation
    - impurity: arsenic
    - dosage/energy: $10^{14} cm^{-2}$/35Kev
12. Strip SiO_2
13. CVD oxidation
    - temperature: 400°C
    - thickness: 3000 Å
14. Post-implantation annealing
    - ambient: Argon
    - temperature/time: 700°C/20 min
15. Open window for contact (mask #4).
16. Metalization
    - define metal patterns (mask #5)
    - deposit Ti/Pd/Ag metals
    - lift-off process
17. Post-metalization anneal
    - temperature/time: 400°C/5 min
18. Package and Test

VITA

VITA

Daniel Li-Chung Huang was born in Keelung, Taiwan, Republic of China on June 27, 1950. He received a Bachelor of Science degree in Physics from Fu Jen University, Taipei, Taiwan in June 1972, and a Master of Science degree in Physics in 1976 and MSEE degree in 1978 from University of Cincinnati.

From 1972 to 1974, he served as a Second Lieutenant in Chinese Army. From 1978 to 1979, he was with the University of Arizona. In 1979 he joined Delco Electronics where he worked on bipolar integrated circuits. He returned to graduate school at Purdue University in 1982 and has been a research assistant since then. He was married to Ellen Shue-Lan Ko in June 18, 1977. They have three sons, Joseph, and twins, Brian and Kevin.